NASA Contractor Report 174779

NASA-CR-174779
19850002915

The Effect of Tantalum and Carbon on the Structure/Properties of a Single Crystal Nickel-Base Superalloy

Hung C. Nguyen

Michigan Technological University
Houghton, Michigan

October 1984

Prepared for

NATIONAL AERONAUTICS AND SPACE ADMINISTRATION
Lewis Research Center
Under Grant NAG 3-216

ENTER: D

2 1 1 RN/NASA-CR-174779

DISPLAY 02/6/1

85N11223*# ISSUE 2 PAGE 182 CATEGORY 26 RPT#: NASA-CR-174779 NAS 1.26:174779 CNT#: NAG3-216 84/10/00 100 PAGES UNCLASSIFIED DOCUMENT

UTTL: The effect of tantalum and carbon on the structure/properties of a single crystal nickel-base superalloy TLSP: M.S. Thesis. Final Report

AUTH: A/NGUYEN, H. C.

CORP: Michigan Technological Univ., Houghton. AVAIL.NTIS SAP: HC A05/MF A01

MAJS: /*CARBON/*HEAT RESISTANT ALLOYS/*NICKEL ALLOYS/*SINGLE CRYSTALS

MINS: / CHEMICAL COMPOSITION/ HEAT TREATMENT/ MICROSTRUCTURE/ TENSILE PROPERTIES

ABA: R.J.F.

SUMMARY

THE EFFECT OF TANTALUM AND CARBON ON THE STRUCTURE/PROPERTIES OF A SINGLE CRYSTAL NICKEL-BASE SUPERALLOY

The microstructure, phase chemistry, and creep and hot tensile properties were studied as a function of tantalum and carbon levels in Mar-M247 type single crystal alloys. Microstructural studies showed that several types of carbides (MC, $M_{23}C_6$ and M_6C) are present in the normal carbon (0.10 wt.% C) alloys after heat treatment. In general, the composition of the MC carbides changes from titanium-rich to tantalum-rich as the tantalum level in the alloy increases. Small (~0.2 μm) $M_{23}C_6$ carbides are present in all alloys. Tungsten-rich M_6C carbides are also observed in the alloy containing no tantalum. No carbides are present in the low carbon (0.01 wt.% C) alloy series.

The morphology of γ' is observed to be sensitive to heat treatment and tantalum level in the alloy. Cuboidal γ' is present in all the as-cast structures. After heat treatment, the γ' precipitates tend to have a more spheroidal-like morphology, and this tendency increases as the tantalum level decreases. On prolonged aging, the γ' reverts back to a cuboidal morphology or under stress at high temperatures, forms a rafted structure. The weight fraction and lattice parameter of the spheroidal γ' increases with increasing tantalum content. Changes in the phase chemistry of the γ matrix and γ' have also been analyzed using phase extraction techniques. The partitioning ratio (percent element in γ'/percent element in γ) decreases for tungsten and aluminum and increases for tantalum as the tantalum content increases for both alloy

series; no significant changes occur in the partitioning ratios of the other alloying elements.

A reduction in secondary creep rate and an increase in rupture time result from increasing the tantalum content and decreasing the carbon level. The latter result can be interpreted in terms of a "cascade effect"; that is, the primary benefit of removing carbon is to release those metallic elements, most notably tantalum, which otherwise partition to carbides, into the γ and γ' phases. The results strongly suggest the MC carbides do not directly influence the secondary creep rate or rupture life but do cause a reduction in rupture ductility. The data also suggest the principal sources of strengthening from tantalum arise from an increase in the amount of γ' with tantalum and an increase in solid solution strengthening of γ and γ' as a result of the phase chemistry changes. However, changes in the antiphase boundary energy of γ' with tantalum and a greater propensity for the γ' raft structure to form in creep tests at higher temperatures with increasing tantalum may also be factors.

TABLE OF CONTENTS

INTRODUCTION

The development of nickel-base superalloys began in the 1940's because of the need for materials that exhibited good resistance to creep and oxidation at high temperatures, and could, therefore, be used in aircraft gas turbine engines. Although the largest use of nickel-base superalloys remains within the aircraft and industrial gas turbine industries, nickel-base superalloys have also found application in such areas as steam power plants and chemical processing equipment.

The term "superalloy", associated with commercial nickel-base alloys, is attributed to their superior mechanical properties which are independent of temperature up to or exceeding 700 - 800°C. Nickel-base superalloys are usually divided into two classes depending on whether the alloy is cast or wrought. In general, those alloys which are cast have higher temperature capabilities than wrought alloys since the former contain additional alloying elements which lead to enhanced solid solution strengthening and precipitation hardening.

Nickel-base superalloy development has continued over the years in response to the need for further improvements in high temperature strength and resistance to hot corrosion and oxidation so that the operating temperatures in advanced gas turbine engines could be increased. However, a new factor in alloy design has surfaced recently concerning the availability of certain alloying elements used in nickel-base superalloys but obtained primarily from sources outside the United States. Specifically, the United States imports over 90% of its tantalum, cobalt, chromium, and niobium, and as a result, these elements have gained "strategic element" status within the aerospace industry [1,2]. Because the availability of these critical alloying elements may not be

assured in the future, it has been recognized that systematic studies must be undertaken to understand the effect these various alloying elements have on the microstructure, mechanical properties and environmental resistance of nickel-base superalloys [2]. The goal of these programs is to utilize the structure/property information to devise a strategy whereby the strategic elements could be reduced or replaced by other alloying elements while still maintaining the superior properties of the alloy. Therefore, the objective of this study is to define the role that one of the strategic elements, tantalum, plays in the high temperature mechanical properties of a commercially important cast nickel-base superalloy, Mar-M247.

Microstructures of Nickel-Base Superalloys

Since the mechanical properties of an alloy are related to its microstructure, a logical starting point is to examine the microstructure of nickel-base superalloys. The microstructure of most nickel-base superalloys consists of a fcc nickel/chromium solid solution (γ phase) matrix in which precipitates of the γ' phase are dispersed. γ' is an ordered and coherent phase (with γ) which will precipitate if sufficient amounts of aluminum and/or titanium are present in the composition. The γ' structure is an ordered variant of the fcc structure ($L1_2$ structure) with composition $Ni_3(Al,Ti)$; the aluminum and titanium atoms are positioned at the corners of the unit cell and the nickel atoms are in the face-centered positions.

Commercial superalloys contain a number of additional alloying elements. These alloying additions are used to solid solution strengthen γ and γ' and/or change other properties of the γ' phase. Typical additions are refractory elements such as tungsten and molybdenum which

partition to the γ matrix. Cobalt and iron are also common alloying additions which partition to the γ matrix. Titanium and aluminum are also known to be present in the γ phase from phase analyses of a number of commercial nickel-base superalloys [3]. Vanadium, tantalum and niobium partition to γ' although cobalt, chromium, molybdenum and tungsten are also present in γ' at concentrations less than in the γ phase of the same alloy [3]. Within γ', it is believed that cobalt substitutes solely for nickel atoms while niobium, titanium, vanadium and possibly tantalum substitute for aluminum. The remaining elements substitute for nickel and aluminum [4]. The substitution of particular elements for aluminum or nickel in γ' (which may cause the rejection of other elements to γ) is important because the degree of mismatch between the lattice parameters of γ and γ' can be changed. In addition to possibly influencing the mechanical properties of the alloys, it is thought the degree of mismatch controls the γ' morphology. If the mismatch is small (less than 0.5%), spheroidal particles of γ' form. As the mismatch increases through alloying additions, cuboidal γ' particles and eventually plate-like γ' occur [5].

In addition to the γ' phase, carbides are generally found in interdendritic regions or at grain boundaries in nickel-base superalloys. The preferred location of the carbides, for alloy design purposes, is at the grain boundaries in polycrystalline alloys where their primary function is to inhibit grain boundary sliding. Grain boundary sliding becomes an important deformation mechanism at high temperatures which can lead to premature failure. At high temperatures, the presence of discrete carbides on the grain boundaries restricts deformation in the grain boundary region leading to increased creep resistance and

rupture lifetime. Four distinct types of carbides have been observed in superalloys: MC, $M_{23}C_6$, Cr_7C_3 and M_6C. "M" in the formulas represents carbide forming elements such as tantalum, titanium, tungsten, niobium and chromium or some combination of these elements.

MC carbides are believed to be the first carbides formed during solidification at temperatures just below the melting point of the alloy. MC carbides have a coarse cubic ("blocky") and "script" type morphology and are considered to be reasonably stable carbides in nickel-base superalloys. However, MC carbides will decompose to other carbide forms in certain temperature ranges, although the addition of tantalum or niobium tends to stabilize MC carbides from this decomposition [4].

$M_{23}C_6$ and M_6C carbides usually form as a product of solid state transformations at temperatures lower than 1000°C. $M_{23}C_6$ carbides often precipitate at grain boundaries in the temperature range from 760°C to 980°C as a result of the reaction:

$$MC + \gamma \longrightarrow M_{23}C_6 + \gamma'$$

$M_{23}C_6$ is predominantly a chromium rich carbide and plays an important role in influencing the creep properties of an alloy by inhibiting grain boundary sliding. M_6C precipitates at higher temperatures than does $M_{23}C_6$ (815°C - 980°C) in superalloys through a reaction similar to the formation of $M_{23}C_6$. This carbide generally occurs when the molybdenum and tungsten content of the alloy is high. The morphology of M_6C carbides is very similar to $M_{23}C_6$ and the carbides often exist as discrete particles located on grain boundaries. M_6C carbides may also occur as platelets with an acicular morphology.

An undesirable component in the microstructure of nickel-base superalloys is the presence of topologically close packed (TCP) phases such as σ, μ, and Laves. These phases are sometimes observed after extended aging at high temperature. For example, sigma phase was observed in Udimet 700 after aging for more than 500 hrs at temperatures of 760°C and 845°C [6]. TCP phases typically form as thin plates parallel to $\{111\}_\gamma$ and can act as sources for crack initiation and propagation with a resultant loss in rupture strength and ductility. TCP phase formation also affects solid solution strengthening by removing refractory elements such as molybdenum and tungsten from γ and γ', and can alter the γ' morphology by reducing the γ/γ' mismatch. The formation of TCP phases results when the composition of the alloy is not properly controlled. However, with an alloy design technique known as PHACOMP (PHAse COMPutation), the formation of TCP phases can be avoided in superalloys [7].

Boron in concentrations from 0.005 to 0.02 wt pct and zirconium from 0.005 to 0.1 wt pct are often present in the composition of nickel-base superalloys. Although M_3B_2 type borides may be present at the grain boundaries, the beneficial effect of these alloying additions are thought to occur from their presence as atoms which migrate to and fill "open space" at grain boundaries. This strengthens the grain boundary region by slowing down grain boundary diffusion processes which contribute to creep deformation [4].

Overview of Strengthening Mechanisms in Nickel-Base Superalloys

A discussion of the structure/properties relationships in nickel-base superalloys can be divided into two sections; first, a description of the possible mechanisms contributing to the yield or flow stress of

γ' containing nickel-base superalloys before examining the more specific nature of high temperature creep strength in these alloys.

The mechanisms that predominantly contribute to the strengthening of a nickel-base superalloy are solid solution strengthening of γ and γ' and precipitation hardening from the presence of the γ' precipitates in the γ matrix. The parameters important in the precipitation hardening by γ' include the volume fraction and particle size of γ', the energy of the antiphase boundary (APB) faults produced when a dislocation from the matrix cuts through an ordered γ' particle, and the magnitude of the coherency strain produced by the mismatch in the lattice parameters between γ and γ'. It should be appreciated that more than one of these mechanisms will make a contribution to the flow stress in a commercial alloy and that the various contributions will not be simply additive.

The ability of a solute to solid solution strengthen a matrix is believed to be primarily dependent upon the difference in lattice parameter and elastic moduli of the solute and solvent atoms. Fleischer [8] and Labusch [9,10] have proposed theories that can be used to explain the functional dependence of yield stress on solute concentration for binary systems. The situation in nickel-base superalloys is more complex because a number of elements partition to γ and γ'. However, based upon the change in the lattice parameter [11] and flow stress [12] of nickel when various solutes are added and the relative difference in moduli of nickel and various solutes, refractory elements such as molybdenum and tungsten as well as aluminum and chromium are believed to be the most potent solid solution strengtheners of γ. An additional contribution which has been considered is the effect of the solutes on the stacking fault energy of γ [13]. Lowering the stacking

fault energy makes cross slip more difficult and would also result in a hardening increment.

The strengthening of a nickel-base superalloy due to the presence of γ' in its microstructure is related to several factors listed at the beginning of this section. While solid solution hardening of γ' may make a contribution, substantial strengthening is attributed to the creation of APB's as the γ' particles are sheared by (a/2)<110> type dislocations gliding on {111} planes at low temperatures and possibly on {001} planes at high temperatures; the dislocations travel in pairs with the first dislocation creating, and the second dislocation eliminating, the APB. A number of theories have been advanced to explain the increase in flow stress when the particles are sheared in order hardening (see reference 14 for a review). Recently, these theories have been criticized as not pertaining to nickel-base superalloys when large volume fractions of γ' are present [15] and more recent theories, taking into account the presence of obstacles in large concentrations, have been derived [15,16]. However, in all of these models, the flow stress still depends on the APB energy so that a goal in alloy design is to alter the γ' composition with a concomitant increase in the APB energy. Titanium is known to increase, and chromium is known to decrease, the APB energy [17], and elements such as tantalum, niobium and molybdenum are believed to increase the APB energy. In general, the flow stress also increases as the particle size and volume fraction increase. With increasing particle size, however, it eventually becomes easier for single matrix dislocations to move past the γ' particles by the Orowan bypass mechanism [18].

Coherency strain hardening is dependent on the difference in lattice parameters between γ and γ' [19,20]. The interaction between dislocation and particle arises physically from the stress field of the dislocation interacting elastically with the coherency strains introduced into the matrix by the precipitate misfit. There has been debate over the relative contribution of coherency strain hardening to the overall strengthening in nickel-base alloys. In a detailed study on a high (approximately 60%) volume fraction γ' alloy (Mar-M200), it was concluded that about 80% of the flow stress at room temperature was derived from order hardening with the remainder due to solid solution hardening and coherency strain hardening [21].

The role of carbides in inhibiting grain boundary sliding has been discussed. However, carbides form intragranularly and are also present in some single crystal alloys. The potential strengthening effects of these carbides, therefore, need to be addressed. Carbides sometimes precipitate on stacking faults or dislocations during creep if some carbon still remains in solution. The precipitation of fine carbides on dislocations during creep can reduce the mobility of the dislocations leading to an increase in creep strength [22]. The influence of the carbides formed during solidification on strength and creep properties should be negligible since their spacing is too large to interfere with dislocation motion. These carbides, on the other hand, may play an important role in fracture. Finally, regardless of the preferred site of the carbides in the microstructure, they indirectly affect strengthening by removing those alloying elements such as titanium, tungsten and tantalum which would otherwise partition to γ and γ'.

Creep Mechanisms in Superalloys

At temperatures greater than $0.5T_m$ (T_m = melting temperature), time dependent changes in strain at constant stress, known as creep, become an important aspect of deformation. The ability of a material to resist creep is important because components in a gas turbine engine, for example, are subjected to a constant stress for prolonged periods of time at elevated temperature. The creep curve of any metal can be separated into three successive stages: a) primary creep, in which the creep rate gradually decreases with time, b) secondary creep, sometimes called steady state creep, where the creep rate remains nearly constant with time, and c) tertiary creep, a period where the creep rate increases continually with time until rupture occurs. All three stages of the creep curve may not be observed during the creep testing of a metal or alloy. For instance, at high stresses and high temperatures, the primary stage is rarely observed. Thus, the creep curve and creep rates are strongly dependent on factors such as temperature and stress level, but will also be influenced strongly by the microstructure of the material.

The secondary creep rate is usually a critical alloy design parameter since a component spends most of its lifetime in this regime. Secondary creep may result from the simultaneous operation of several deformation mechanisms active at high temperatures such as thermally assisted dislocation motion (dislocation creep), grain boundary sliding and diffusional creep. Since single crystals are being investigated in the present study, only thermally assisted dislocation motion need be considered.

In pure metals or solid solution alloys which deform by dislocation creep, it has been shown that the secondary creep rate ($\dot{\varepsilon}_s$) can be related to the applied stress using a power law expression of the type [23]:

$$\dot{\varepsilon}_s = A[\sigma/E(T)]^n \exp(-Q_c/RT) \quad (1)$$

where σ is the applied stress, the stress exponent n is in the range 3 to 5, Q_c is the apparent creep activation energy (often found to be equal to the activation energy for self diffusion), E(T) is Young's modulus corrected for temperature and A is a structure/materials dependent constant. In precipitation strengthened alloys, however, n is found to be in the range of 6 to 75 and Q_c is reported to be 2 to 3 times greater than the activation energy for self diffusion (see references 24 to 28, for example). It has been suggested for alloys strengthened by second phase particles, the creep equation can be rewritten as [27,29 to 31]:

$$\dot{\varepsilon}_s = A^*[(\sigma-\sigma_r)/E(T)]^{n_o} \exp(-Q_o/RT) \quad (2)$$

where A* is again a material/structure constant, σ_r is a "resisting" stress, and the quantity $(\sigma - \sigma_r)$ represents the effective stress acting on mobile dislocations during creep. When creep data for precipitation hardened alloys are analyzed using equation (2), n_o is usually equal to 3 or 4 and Q_o is equal to the self diffusion activation energy. The origin and magnitude of the resisting stress depends upon applied stress, temperature and the microstructure. The latter dictates the type of dislocation-obstacle interaction; for example, the dislocation can move past second phase particles by the Orowan looping mechanism, shearing through the particles, or by diffusion controlled climb [32,33]. Each different dislocation-obstacle interaction should require

a different resisting stress and this has been demonstrated in several systems [26,27]. It has been also suggested that the resisting stress should be equal to the macroscopic yield stress obtained in a hot tensile test at the same temperature and strain rate as the steady state creep rate obtained in a creep test [27,34 to 36]. However, there are not sufficient data to support this conjecture.

The two major contributions to the creep resistance of nickel-base superalloys are the γ' precipitates acting as obstacles to mobile dislocations and the solid solution strengthening elements present in the γ matrix. Our previous discussion of solid solution hardening in terms of impeding dislocation motion would be applicable at temperatures up to at least 0.6 T_m. At temperatures greater than 0.6 T_m, diffusion becomes rapid and the primary function of the solute atoms is to slow down diffusion in γ. Refractory elements such as molybdenum, tungsten and tantalum are effective in this regard because of their high melting points and thus, low diffusion coefficients in the temperature range important in the application of nickel-base superalloys. In addition, the secondary creep rate is the result of a balance between strain hardening and recovery; the latter involves coarsening of the dislocation network which forms due to diffusion controlled climb and/or thermally-activated cross slip. Therefore, if the solute additions lower the stacking fault energy of γ and the propensity for cross slip, a reduction in the creep rate should result [37].

Creep resistance, with regards to precipitation hardening by γ', is enhanced in general by refining the particle size and spacing to either increase the Orowan stress or to force the dislocations to shear through the γ' particles. If the latter mechanism occurs, increasing the

resistance of the γ' particle to shearing by the dislocations is the alloy design goal; for instance, it would be desirable to increase the APB energy or the strength of γ' by alloying element additions. An additional factor is that particle coarsening takes place during creep at high temperatures. Stevens and Flewitt [38] have shown that creep curves in IN 738 fail to show primary or secondary creep stages but exhibit instead a continuously increasing creep rate at 850°C. This behavior was attributed to coarsening of the bimodal spheroidal and cuboidal γ' precipitate distribution during creep testing. Although there appeared to be no effect of stress on the coarsening rate in the study of Stevens and Flewitt, stress induced coarsening of γ' can be an important factor in creep deformation [39]. A recent study [40] indicated that the onset of tertiary creep in a superalloy was a result of the stress induced coarsening of γ'. One possible influence on the coarsening rate of γ' is the mismatch in lattice parameter between the γ-γ' phases [41]. It has been suggested that to stabilize the γ' morphology in superalloys under stress and/or long term exposure at high temperatures, one must minimize the degree of mismatch between the γ matrix and the γ' precipitates. This leads to a low coarsening rate of γ' and helps to enhance the creep resistance of the alloy.

However, Pearson et al. [42] have shown that in Ni-Al-Ta-Mo single crystals, the directional coarsening of γ' into platelets perpendicular to the stress axis significantly increased the creep resistance of the alloy. Pearson et al. also indicated the directional coarsening of γ' is not a gradual coarsening process but occurs very rapidly in the creep test. This was confirmed in more recent studies [43,44] in which the formation of γ' platelets or rafts was found to begin in the primary

creep stage. A stable raft γ' structure was developed at the end of primary creep or early in secondary creep and stayed very much unchanged until the onset of the tertiary creep stage. Since the γ' raft structure is fine and continuous, it prevents the dislocations from bypassing the γ' by the Orowan mechanism and also impedes dislocation climb around the γ' [42], thereby reducing the secondary creep rate.

Finally, when single crystal alloys are utilized, there is a significant influence of orientation on the creep behavior. Studies on single crystals of Mar-M200 demonstrated that substantial stress rupture times were obtained for crystals oriented near [001] and [111] at 760°C and 871°C while short stress rupture times were obtained for crystals oriented near [011] [45]. Further studies demonstrated that at 760°C, primary creep occurred from slip on {111}<112> rather than {111}<110> [46 - 48], while secondary creep took place on the latter slip system. It was concluded that the secondary creep occurred only after sufficient strain hardening took place on intersecting {111}<112> slip systems. More recent work on Mar-M247 has shown that the rupture time at 774°C is strongly determined by the lattice rotation required to produced intersecting slip [49,50]; as the rotation to obtain slip on more than one {111}<112> slip system increased, a large primary creep strain resulted and the specimen failed during primary creep or a large true stress is obtained at the beginning of secondary creep which produced high secondary creep rates and low stress rupture lives.

Overview of the Present Study

An advantage of utilizing tantalum as an alloying element in nickel-base superalloys arises from its effect on structure/properties. Tantalum is a strong carbide former and can alter the type of carbide or

carbides present when added to an alloy. Tantalum is believed to partition to γ' (i.e., it is a γ' forming element) although tantalum has been found to partition evenly between γ and γ' when hafnium is present [51]. In fact, Ford and Herchenroeder [52] have suggested that tantalum improves the high temperature stability of γ' because it does partitions evenly between γ and γ'. If tantalum is a γ' forming element, its addition would increase the volume fraction of γ', the γ' strength through solid solution hardening [53] and, it is believed, the magnitude of the APB energy of γ'. The tantalum present in γ can act as a potent solution hardener and/or help in reducing the diffusion which takes place in γ during creep. Additions of tantalum can be used also as a partial substitute for tungsten to reduce the possibility of phase instability (i.e., TCP phase formation).

While the general attributes of tantalum with regard to beneficial effects on structure/properties (and in other areas such as improved oxidation and corrosion resistance [54] and castability [55]) are known, no systematic studies exist which examine the change in structure and properties as tantalum is varied in a specific alloy system. Systematic studies are necessary to understand the "Ta effect" so that partial or full substitution of tantalum is possible in an alloy system. Currently the tantalum levels in commercial alloys range from 1.5 to 4.5 wt% in polycrystalline cast alloys such as Mar-M246 and B1900, respectively, up to 12 wt% in the new single crystal cast alloy 454. Therefore, an additional (and broader) aim of the present work is to provide a basis upon which to rationalize why these tantalum levels yield the desired mechanical properties in current alloys, and more importantly, to begin to provide a fundamental knowledge base from which the next generation

of superalloys can benefit from the properties imparted by tantalum in the current alloys.

The present study examines the tantalum effect by systematically varying the tantalum content in a commercially important cast nickel base superalloy, Mar-M247. Single crystals were used to avoid the additional complication of grain boundary effects on mechanical properties. Two levels of carbon have been utilized in the program in addition to the tantalum variations; one carbon content is a typical Mar-M247 level of 0.1 wt.% while the second is a low carbon (LC) version with 0.01 wt.%. Since the alloys with the typical carbon content contain carbides in addition to γ and γ' while no carbides form in the LC series of alloys, an additional feature of the study is to assess whether the carbides directly influence the mechanical properties of single crystal Mar-M247.

EXPERIMENTAL PROCEDURE

A. Materials

A master metal alloy based on the Mar-M247 composition (Table 1) but stripped of tantalum, zirconium, hafnium, boron and carbon was vacuum induction melted and cast into 8cm round ingots by Cannon-Muskegon Corporation. A series of single crystal test bars, 15cm long and 1.5cm in diameter, were vacuum cast using the withdrawal process at Howmet Turbine Components Corporation with the growth axis approximately parallel to [001]. Two groups of single crystals were cast. Both groups had varying tantalum contents up to or exceeding the normal 3 wt. pct. level found in Mar-M247. However, one group contained the typical carbon level in Mar-M247 of 0.1 wt. pct. while the other group contained as little carbon as possible from the melting practice (see Table 2). The latter group was designated as the low carbon (LC) alloys.

B. Heat Treatment

The typical heat treatment cycle for Mar-M247 consists of a solution heat treatment above the γ' solvus temperature followed by an argon quench to room temperature. Subsequently, a single aging heat treatment at 871°C±5°C for 20 hrs was employed followed by air cooling to room temperature.

Before heat treatments were conducted on the six alloys in the present study, the γ' solvus and the solidus temperatures had to be established for the various alloys. Differences in the γ' solvus and the solidus temperatures were expected because of the alloying element variations. The γ' solvus and solidus temperatures were established from differential thermal analyses (DTA) performed by General Electric Research Laboratory at Schenectady, NY, and were found to be a function of

Table 1. Nominal Composition of Mar-M247 (wt. pct.)

Elements	Mar-M247
Al	5.50
C	0.15
Co	10.00
Cr	8.30
Mo	0.70
Ta	3.00
Ti	1.00
W	10.00
B	0.015
Zr	0.05
Hf	1.50
Ni	Bal

Table 2. Composition of Alloys Used in This Study (wt. pct.)

Element	Alloy E	Alloy F	Alloy G	Alloy H	Alloy I	Alloy J
Al	4.88	5.40	5.59	4.94	5.24	5.45
C	0.11	0.10	0.11	0.01	0.01	0.01
Co	9.08	9.60	9.70	9.22	9.43	9.60
Cr	7.87	8.00	8.02	7.87	7.98	8.05
Mo	0.48	0.55	0.58	0.48	0.53	0.55
Ta	--	2.79	4.34	--	1.62	3.07
Ti	0.46	0.52	0.60	0.50	0.55	0.57
W	9.52	9.78	9.76	9.58	9.58	9.74
Ni	Bal	Bal	Bal	Bal	Bal	Bal

the tantalum content in the alloy, with the exception of the solidus temperature for the normal carbon alloys (Figure 1). These data were confirmed by experiments at Michigan Technological University in which as-cast materials were heated to various temperatures for several hours in the vicinity of the γ' solvus temperature before being quenched to room temperature. Transmission electron microscopy (TEM) foils from these specimens were examined to detect whether the as-cast cuboidal γ' dissolved during the solutionizing heat treatment. Using these data, a solution heat treated temperature 15°C above the γ' solvus was selected for each alloy. The complete heat treat cycles are given in Table 3.

C. Metallography

Several specimens were prepared from each alloy for metallographic observation. Specimens were prepared by mechanical polishing through 600 grit silicon carbide papers, followed by polishing on cloth with 1 μm diamond paste. The final polishing was done on cloth with a 0.05 μm aluminum oxide abrasive slurry. Optical metallographic observation of the specimen in the as-polished condition was useful in that the carbide distribution was easily observed. The specimens were then etched by immersion in Marbles reagent for 1 min. (Marbles reagent contains HCl, H_2O and $CuSO_4$ in a 5:5:1 ratio). This preparation delineated the carbides as white particles while the interdendritic regions in as-cast specimens appeared darker due to an increased amount of γ' in that area.

For scanning electron microscopy (SEM) observation, the specimens were prepared using the identical method employed for optical microscopy except that the etching solution consisted of 33% HNO_3, 33% acetic acid, 33% distilled water and 1% hydrofluoric acid, and specimens were coated with a conductive carbon layer. In the SEM, the carbides appeared as

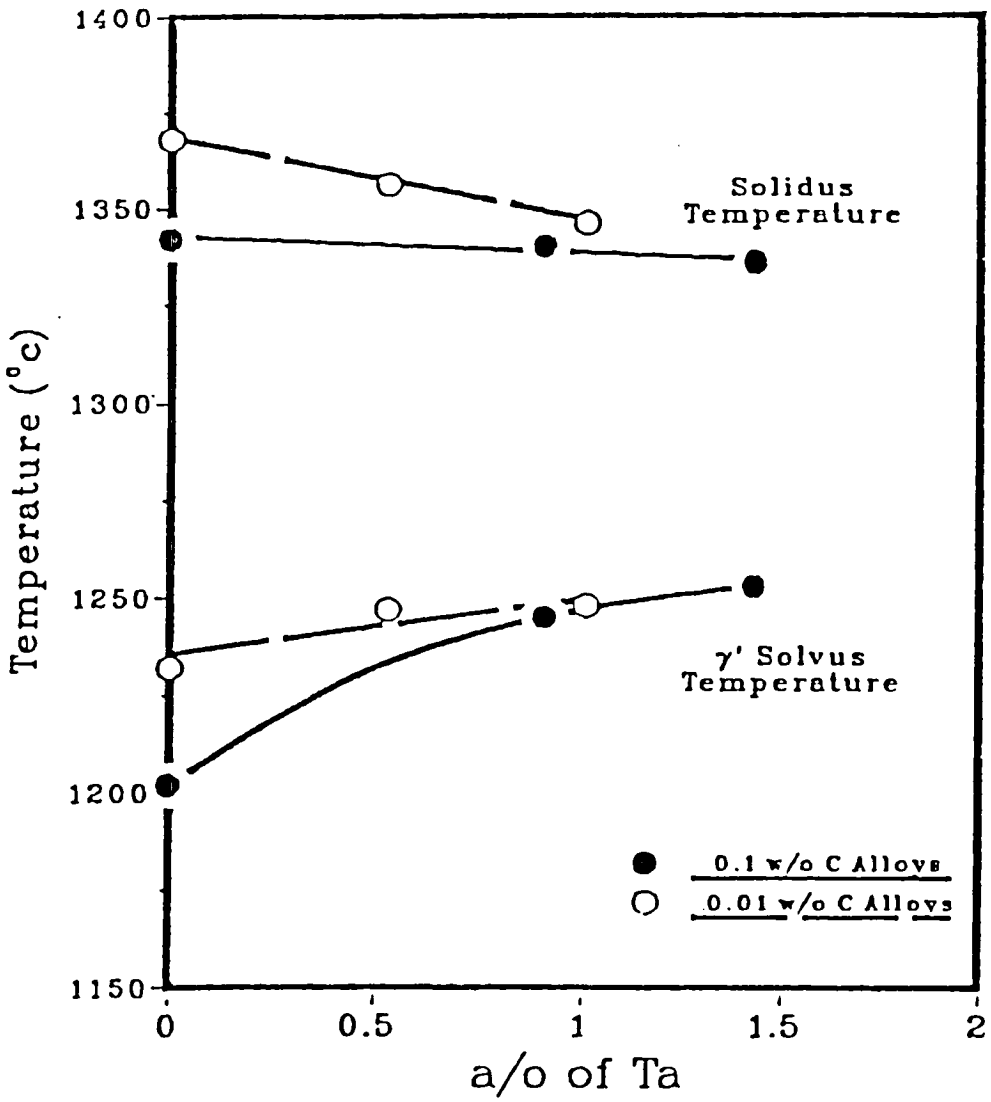

Figure 1. Solidus and γ' solvus temperatures determined from differential thermal analysis as a function of Ta level in the alloy .

Table 3. Heat Treatment Schedule for the Alloys

Alloy	γ' Solvus Temperature (°C)		Solution Treatment
	DTA	TEM Metallography	
E	1200	1175 - 1200	1215°C/4 hrs, Argon Quench
F	1245	1225 - 1250	1260°C/4 hrs, Argon Quench
G	1250	1225 - 1250	1260°C/4 hrs, Argon Quench
H	1235	1225 - 1250	1250°C/4 hrs, Argon Quench
I	1245	1225 - 1250	1260°C/4 hrs, Argon Quench
J	1250	1225 - 1250	1260°C/4 hrs, Argon Quench

All alloys are aged at 871°C for 20 hrs followed by air cooling.

white particles in relief, while γ' appeared as dark, etched out particles. The specimens were examined using a JEOL 35C Scanning Electron Microscope. Non-dispersive x-ray elemental analyses were also performed on the specimens using an EDAX unit attached to the SEM. In addition, some quantitative chemical analyses were run using a computer interfaced with the EDAX analyzer. The program, FRAME, was used to make the appropriate ZAF corrections so that quantitative analyses could be obtained.

In order to achieve higher resolution, transmission electron microscopy (TEM) was also employed to examine the specimens. Specimens were prepared by first mechanically thinning to approximately 0.13mm. Thin foils were obtained by using a two-jet Fischione unit with an electrolyte consisting of 10% perchloric acid in ethanol at a temperature of approximately -15°C and operating conditions of 50V and 70mA. The foils were examined using a Philips 301 transmission electron microscope operating at 100 kV.

D. Phase Extraction and Identification

Phase extraction analysis was used to identify the phases present in the alloys. Specimens for this analysis were about 0.15cm in thickness and a minimum of four extraction runs were obtained for each alloy. Surfaces were grounded and polished through 600 grit silicon carbide paper to remove surface contamination. Specimens were subsequently electropolished in a 20% H_2SO_4 in methanol (CH_3OH) solution using stainless steel as the cathode; this removed any strain induced during mechanical polishing. The electrolyte was discarded, and the specimen surface was cleaned, rinsed with methanol, dried, and weighed.

The γ' and carbide phases were extracted from the alloy matrix using a standard electrolytic extraction technique. An electrolyte consisting of 1% ammonium sulfate, $(NH_4)_2SO_4$, and 1% citric acid in distilled water was used. The specimen (0.15 mm in thickness) was suspended from a wire and submerged in the electrolyte. The contact point between the specimen and the wire (which was coated by microshield) was never in the electrolyte. The dissolution process was automatically stopped when the part of the specimen in the electrolyte totally dissolved*. A typical extraction process was completed in 3 to 4 hours using a current density of $75mA/cm^2$ at room temperature. The residue was collected, dried and weighed. Chemical analysis of the residue was performed by NASA-Lewis Research Center at Cleveland, Ohio using the inductive coupled plasma atomic emission spectroscopy technique. In some cases, the γ' in the residues was subsequently dissolved in a solution of 50% HCl in methanol to obtain a residue containing only carbides. The weight fraction of γ' or the carbides was obtained by dividing the weight of the γ' or carbides residue by the total weight loss.

---

* To verify the accuracy of this technique, specimens were exchanged with Dr. Michael Nathal at NASA-Lewis. Nathal uses a more conventional extraction technique on Mar-M247 in which the specimen is not allowed to totally dissolve. However, the γ' which adheres to the remaining sample must be removed by scraping or lightly sand blasting the specimen. Nathal obtained a γ' extraction of 68 wt.% on alloy J and 67 wt.% on a Mar-M247 specimen he sent us. Our results for the same specimens were 65.5 wt.% and 64 wt.%, respectively, in good agreement with Nathal.

The identification of the phases was performed using x-ray diffraction techniques. A diffractometer was employed using CuKα radiation and a nickel filter at a scanning speed of ½° per min. The diffraction patterns were compared to known patterns in the literature [56] to tentatively identify the carbide phases present in the residue. The lattice parameters of γ' and the carbides were calculated using the Cohen method [57]. From the lattice parameters and the allowed reflections, identification of the carbides was possible.

E. Mechanical Testing

A series of specimens were machined from fully heat treated bars into the tensile and creep specimens shown schematically in Figure 2. Hot tensile tests were carried out at 540°C (1000°F), 760°C (1400°F) and 982°C (1800°F) according to ASTM E21-79. Temperatures were controlled to ±3°C. The 0.2% offset yield strength was obtained along with the tensile strength, reduction in area and % elongation at fracture.

The creep data were obtained under constant stress at 760°C (1400°F) 871°C (1600°F) and 982°C (1800°F) according to ASTM E139-79 . Each specimen was loaded to a given stress level and temperature, and the test allowed to continue until fracture was obtained or the test was terminated after a fixed number of hours. Creep extension was measured automatically using an extensometer and was recorded until the specimen failed. The initial orientation of each test specimen, as well as the final orientations of selected specimens after creep testing, were determined by the Laue back reflection x-ray technique. All hot tensile and creep tests were performed by Joliet Metallurgy Laboratory, Joliet, Illinois.

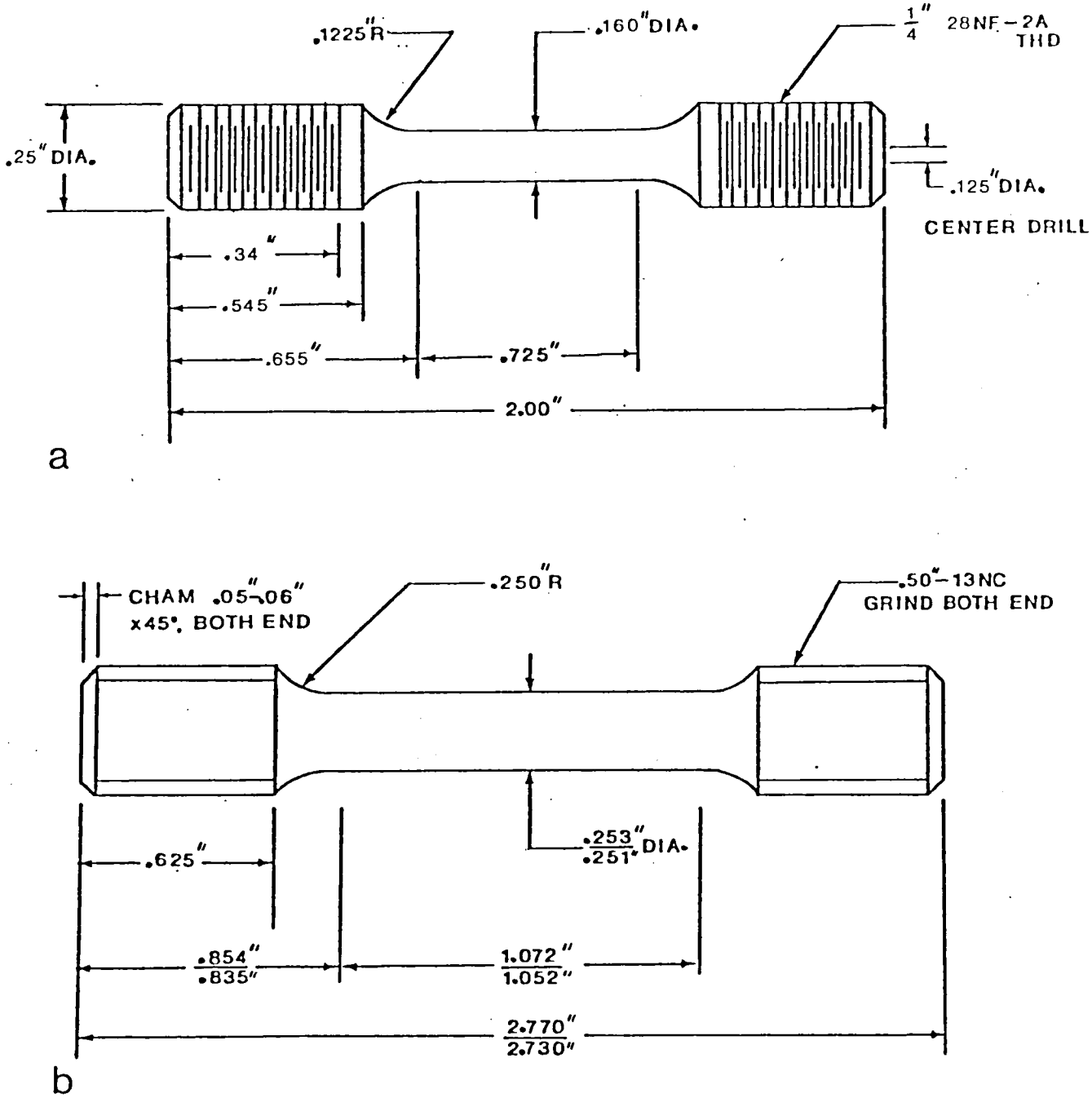

Figure 2. Schematic drawings of the (a) creep specimen and (b) tensile specimen utilized in the study.

EXPERIMENTAL RESULTS

A. Microstructure

As-Cast Structure

Representative as-cast microstructures for the normal carbon alloys are shown in Figures 3a and b. For comparative purposes, optical micrographs were taken at the center of each ingot on transverse sections. All normal carbon alloys displayed a heavily cored dendritic structure in which carbides and coarse γ' (see Figure 4) were present in the interdendritic regions. As the amount of tantalum increased, the volume fraction of carbides also increased (compare Figures 3a and b). X-ray diffraction patterns from the carbide residue revealed that a single primary MC type carbide was present in each alloy. As the tantalum content increased, the lattice parameter increased from 0.432nm to 0.444nm (Table 4). The presence of MC carbides in these alloys was also confirmed from electron diffraction patterns. Optical micrographs of the LC alloys also showed a heavily cored, dendritic structure (Figures 3c and 3d).

The morphology of the γ' precipitate could only be resolved using TEM. The TEM study showed that cuboidal γ' is present in the as-cast structure. More detailed examination of the structure using dark field imaging reveals the presence of a bimodal distribution of γ' (Figure 5); fine γ' particles approximately 0.5 μm in size are present along with an ultrafine γ' whose size was less than 0.1 μm. The bimodal distribution of cuboidal γ' was present in all six as-cast alloys.

Heat-Treated Microstructure

After the heat treatments listed in Table 3, the segregation present in the as-cast structure was partially reduced. No dendritic

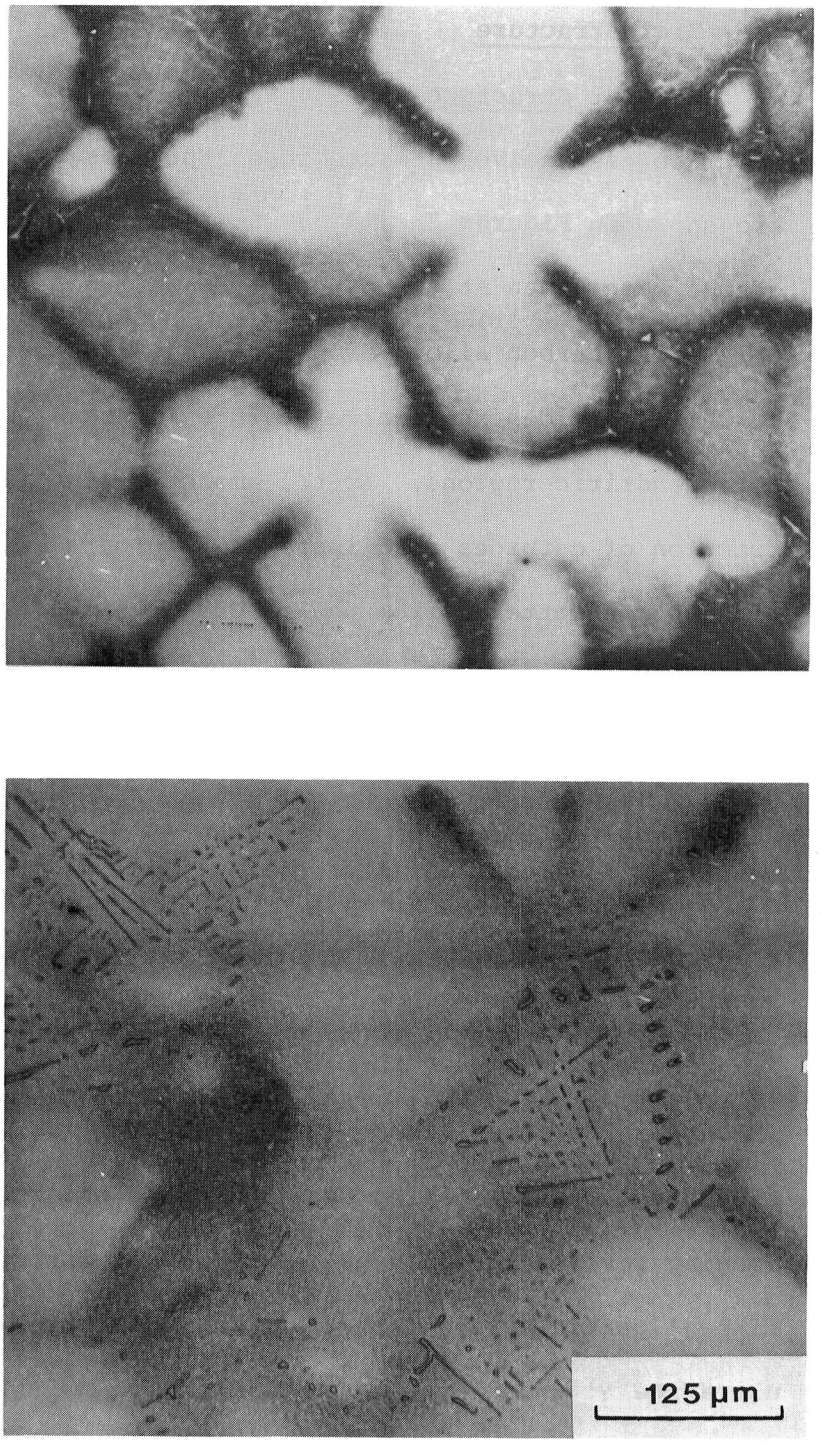

Figure 3. Optical micrographs of the as-cast microstructure in normal carbon Mar-M247 type alloys. In addition to the dendrite structure, note the coarse γ' (dark areas) and fine γ' (gray areas) in both (a) alloy E (0 wt.% Ta) and (b) alloy F (3 wt.% Ta).

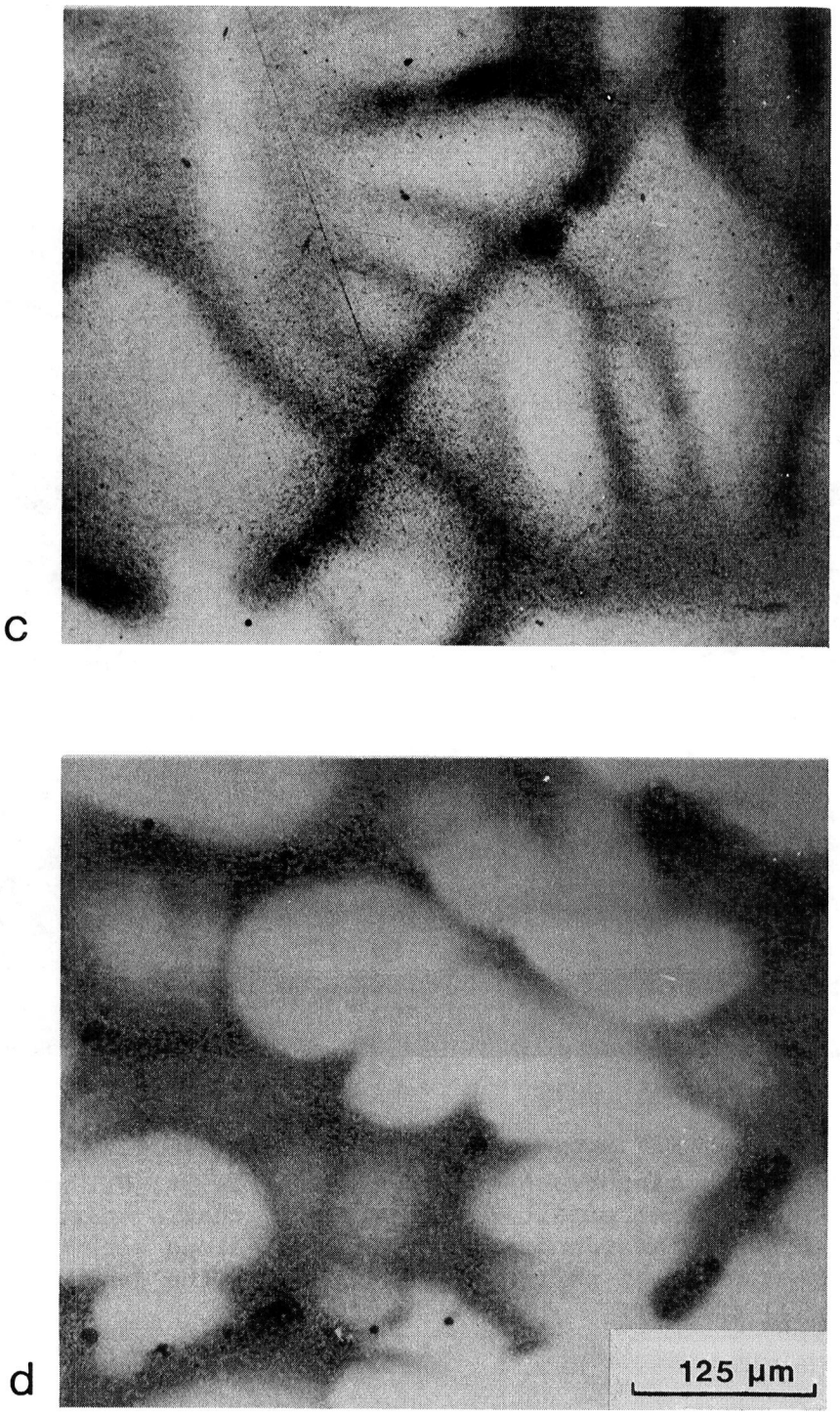

Figure 3. Optical micrographs of the as-cast microstructure in LC Mar-M247 type alloys showing the dendrite structure in (c) alloy H (0 wt.% Ta) and (d) alloy J (3 wt.% Ta).

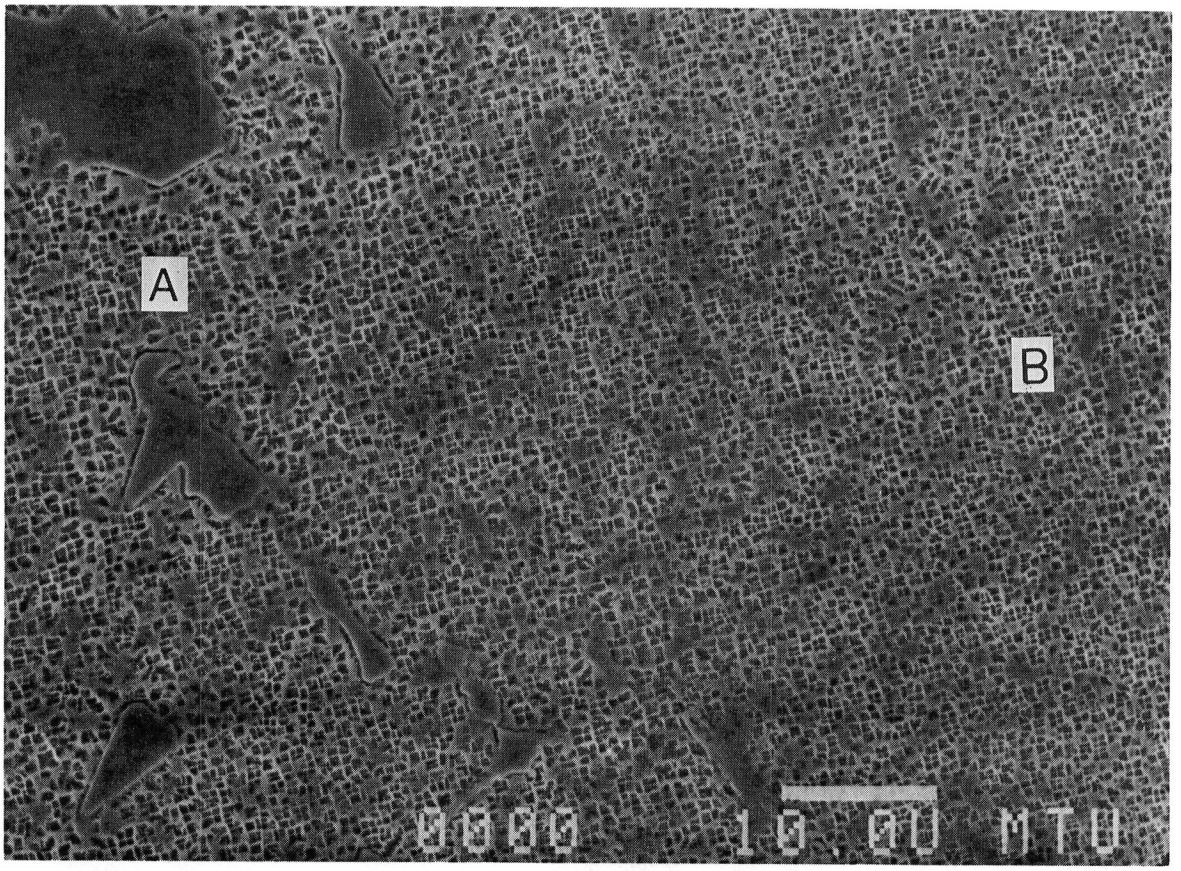

Figure 4. SEM micrograph of alloy F (3 wt.% Ta, 0.1 wt.% C) in the as-cast condition illustrating that a coarse γ' is present in the interdendritic regions (A) along with MC carbides while a finer γ' particle size occurs in the dendrite cores (see region at (B)).

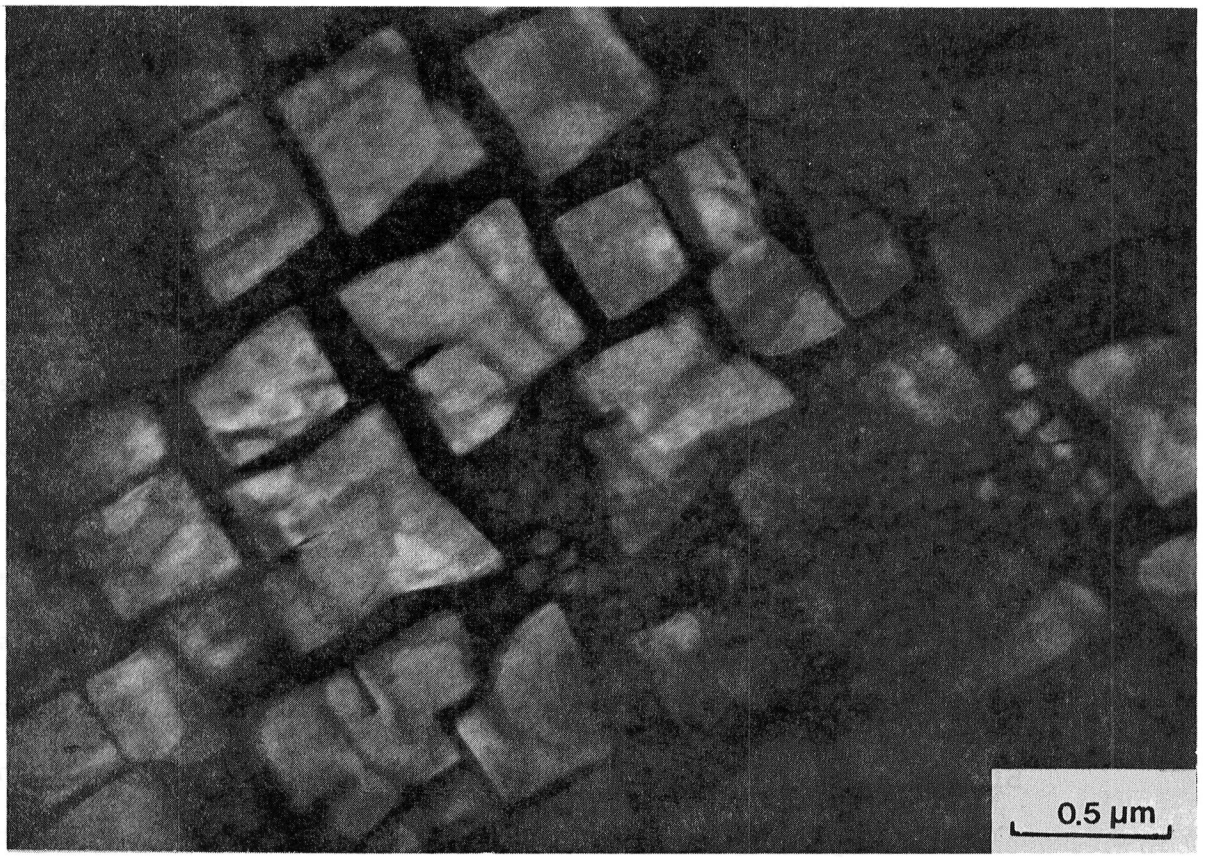

Figure 5. TEM dark field image of alloy F in the as-cast condition illustrating the fine γ' (0.5 μm) and ultrafine γ' (0.1 μm) precipitates.

structure was observed in alloys that were tantalum free or that contained only a low tantalum level such as alloy I. In alloys containing higher tantalum levels such as alloys F and G, a slight trace of the dendritic structure left behind after heat treatment was evident. In-situ EDX (Energy Dispersive X-ray) analyses in the SEM indicated that tungsten was still segregated at the dendrite cores in all six alloys.

Examination of the normal carbon alloys by SEM revealed that another carbide morphology was present in the dendrite cores of alloy E (0 wt.% Ta). Figure 6a shows these new carbides possess an acicular morphology while the MC carbides in the interdendritic regions have an elongated script morphology. X-ray diffraction analyses on the extracted carbide residue from alloy E showed that three distinct carbide phases were present in the alloy; two MC type carbides with lattice parameters of 0.430nm and 0.439nm and a M_6C type carbide with a lattice parameter of 1.110nm (Table 4). However, in-situ EDX analyses indicated there were only two distinct carbide compositions. The acicular carbides present at the dendrite cores were tungsten rich while the other carbide morphology observed in the interdendritic regions was titanium-tungsten rich.

It was concluded that the acicular carbides present in the dendrite cores were tungsten-rich M_6C carbides based on the morphology, composition and lattice parameter of the carbides. Since M_6C carbides form as a result of solid state transformations, this would explain their absence in the as-cast structure. A quantitative estimate of the tungsten and titanium in the other chemically distinct carbide was made using in-situ EDX analysis with a standard ZAF correction program (FRAME). Carbides of sufficient size (~2 μm) were selected to minimize

Table 4. Lattice Parameters and Analysis of Carbides Present in the Normal Carbon Alloys

Alloy	As-Cast Condition	Heat-Treated Condition
E	a_o = 0.432nm, MC	a_o = 0.430nm, MC a_o = 0.439nm, MC a_o = 1.110nm, M_6C a_o = 1.068nm, $M_{23}C_6$
F	a_o = 0.440nm, MC	a_o = 0.437nm, MC a_o = 0.439nm, MC a_o = 1.075nm, $M_{23}C_6$
G	a_o = 0.444nm, MC	a_o = 0.439nm, MC a_o = 1.080nm, $M_{23}C_6$

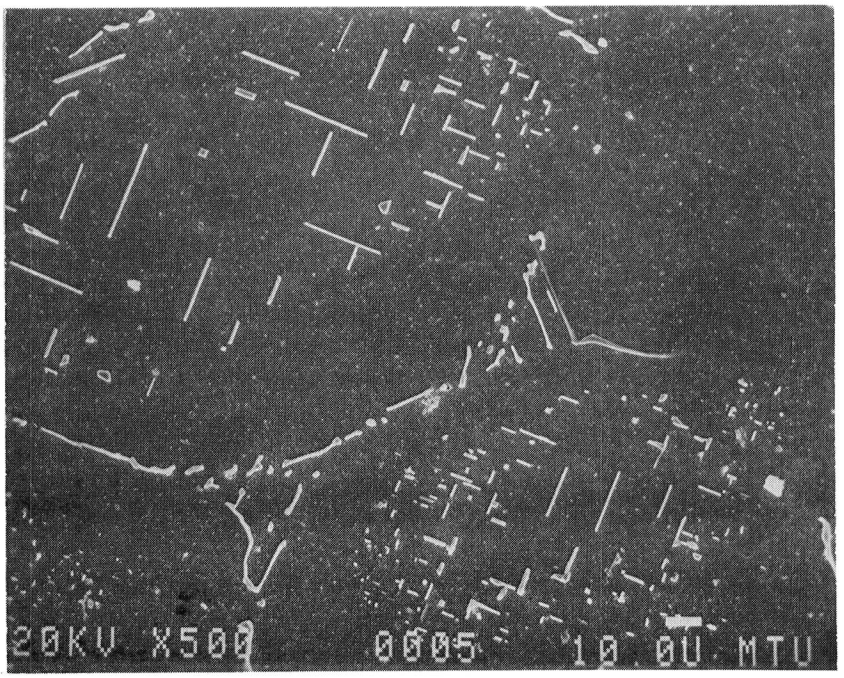

Figure 6a. SEM micrograph of alloy E (0 wt.% Ta, 0.1 wt.% C) after heat treatment. MC carbides have an elongated script morphology in the interdendritic regions while M_6C carbides have an acicular morphology at the dendrite cores.

the matrix effect and an average of twenty analyses yielded a composition of 74 at. % Ti and 26 at. % W. An estimate of the carbide lattice parameter was made assuming Vegard's law and knowing the lattice parameter of pure tungsten carbide (0.4248nm) and pure titanium carbide (0.4328nm); a value of 0.4307nm was obtained. From this, it was concluded the elongated script morphology carbides present in the interdendritic regions were titanium-tungsten rich carbides with a lattice parameter of 0.430nm. The composition (and identity) of the 0.439nm lattice parameter MC carbide is unknown and further work to identify this carbide is planned.

In the alloys containing tantalum, no evidence of the M_6C carbide was found from examination of the microstructures and from the X-ray diffraction analyses. It was observed that some of the elongated script carbides in the interdendritic regions had broken down into small individual almost spheroidal-like particles (1 - 2 μm in size), as shown in Figure 6b. Based on X-ray diffraction analyses of the extracted carbide residue of alloy F, two distinct MC carbides with lattice parameters of 0.437nm and 0.439nm were identified (Table 4). In-situ EDX analysis revealed only one average composition that was tantalum and titanium rich with a small amount of tungsten (47 at.% Ta - 46 at.% Ti - 7 at.% W). A lattice parameter of 0.438nm for this carbide was obtained from the work on Ta-Ti-W-C alloys by Brownlee and Whitehead [11]. This value falls in between the lattice parameters obtained from the X-ray diffraction analyses. It is very possible that the EDX analysis has obtained an average carbide composition and that the two carbides established from X-ray analyses contain slightly less tantalum and slightly more tantalum than the average composition obtained from the EDX analysis.

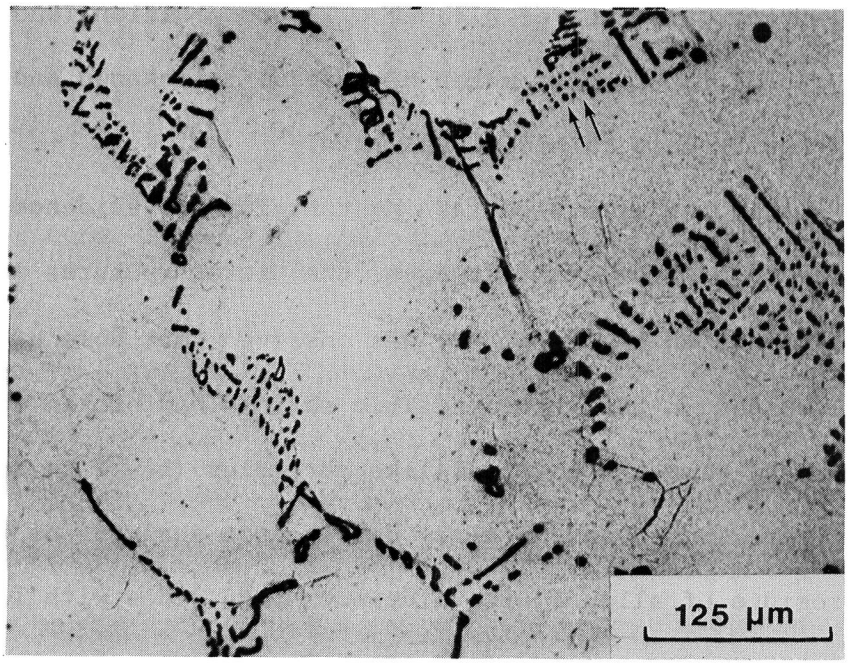

Figure 6b. Optical micrograph of alloy F (3 wt.% Ta, 0.1 wt.% C) after heat treatment in which some of the MC carbides have broken down into small particles (see arrows).

Pure TaC has a larger lattice parameter (0.4455nm) than TiC and WC, and small changes in tantalum content in the carbide could change the lattice parameter by 0.001 or 0.002nm.

Only one distinct set of diffraction lines were found in the X-ray diffraction patterns from the extracted carbide residue of alloy G. The in-situ EDX analysis yielded a slightly more tantalum-rich composition (55 at. % Ta - 37 at. % Ti - 7 at.% W). The lattice parameter estimated using this chemical analysis was 0.4393nm and was in good agreement with the value of 0.439nm determined from the X-ray diffraction analysis.

The lattice parameters of the carbides based on X-ray diffraction analyses were confirmed by TEM thin foil studies. However, unexpectedly, a $M_{23}C_6$ type carbide was found with a lattice parameter of 1.068nm in alloy E, 1.075nm in alloy F and 1.080nm in alloy G. Due to the size of these $M_{23}C_6$ carbides being less than 0.2 μm (Figure 7), they would be difficult to observe by SEM, and because their volume fraction was low, it is not surprising their presence was not revealed by the X-ray diffraction technique.

It was possible to ascertain that the total amount of carbides increased with increasing tantalum content by comparing the microstructures (see Figure 3). This was confirmed from the phase extraction results. The total amount of carbides increased from 1.0 to 1.8 wt.% as the tantalum level increased from 0 to 4.5 wt.% (Figure 8a).

The other surprising result was that the γ' precipitates became more spheroidal in shape after heat treatment as the tantalum level in the alloy was reduced (Figures 9a to 9d). In addition, a bimodal γ' distribution was not found. The average size of the γ' precipitates increased slightly from about 0.15 μm to 0.17 μm as the tantalum level

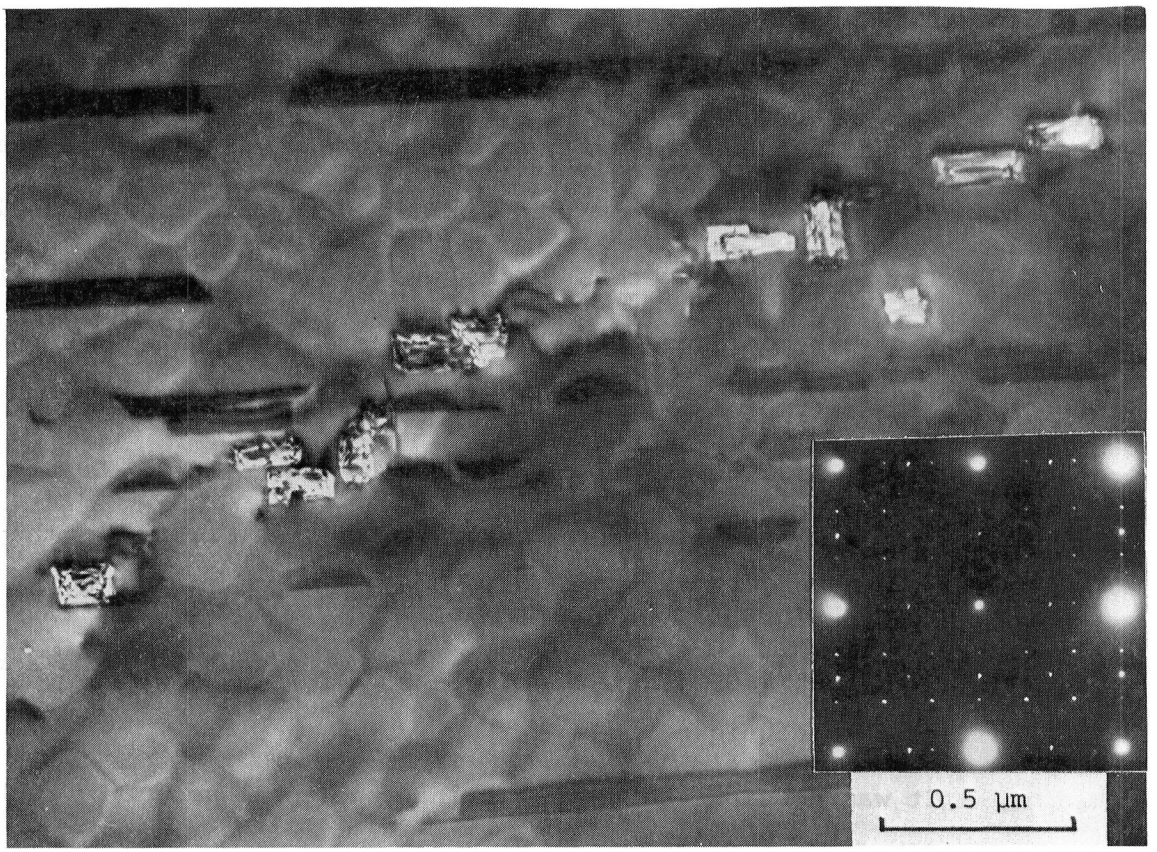

Figure 7. TEM dark field image micrograph of normal carbon Mar-M247 type alloys after heat treatment showing small cuboidal shaped $M_{23}C_6$ carbides. The inset in the lower right corner is a [001] zone axis diffraction pattern from this area. The diffraction spots closest to the transmitted beam (middle bright spot at the bottom of the diffraction pattern) which form a cubic pattern arise from diffraction from carbides. The other intense spots in the pattern are reflections common to the γ and γ' phases while the spots halfway between the transmitted beam and the nearest intense spots are superlattice reflections from the γ' phase.

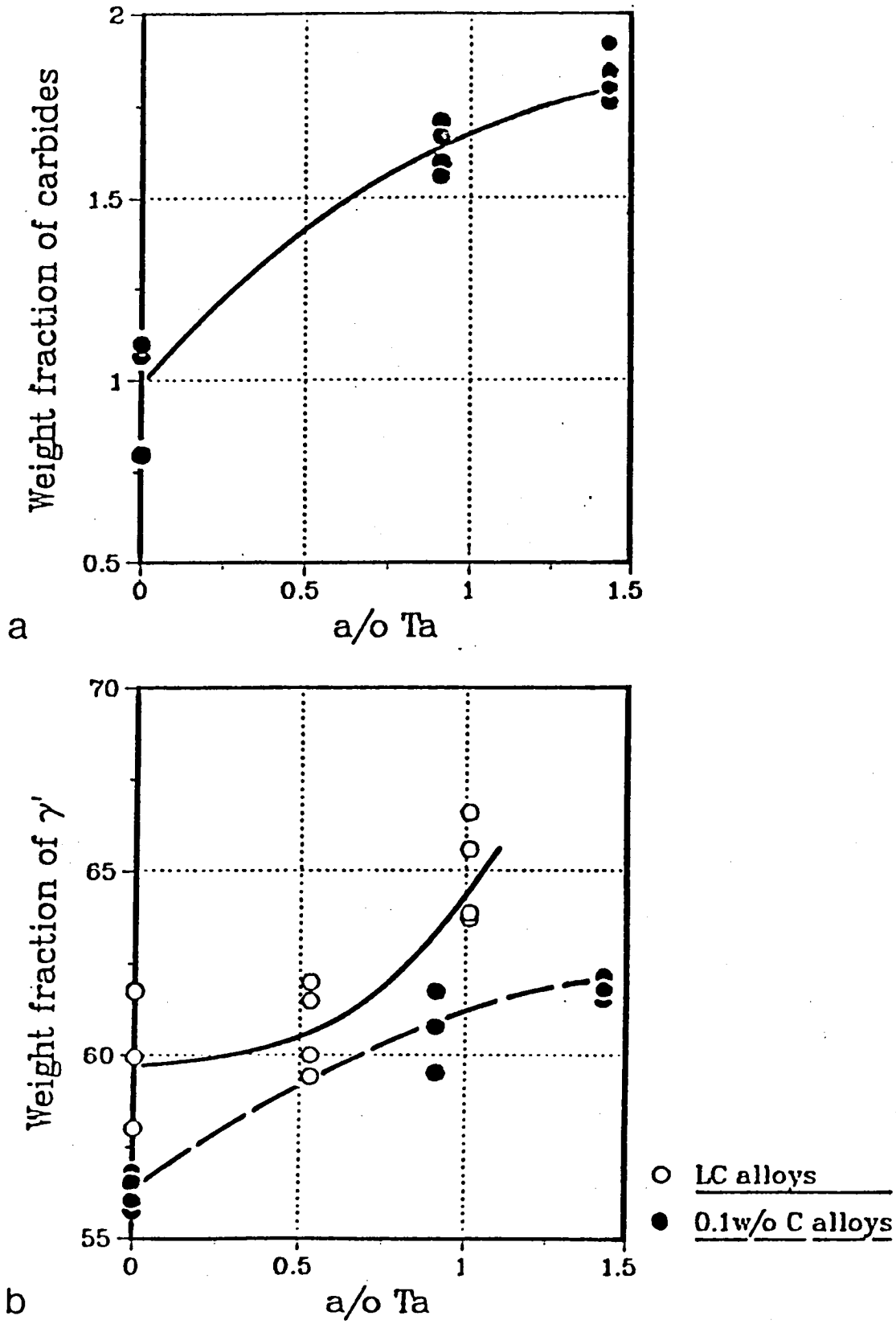

Figure 8. Phase extraction results showing the influence of Ta level in the alloy on (a) carbide weight fraction and (b) γ' weight fraction.

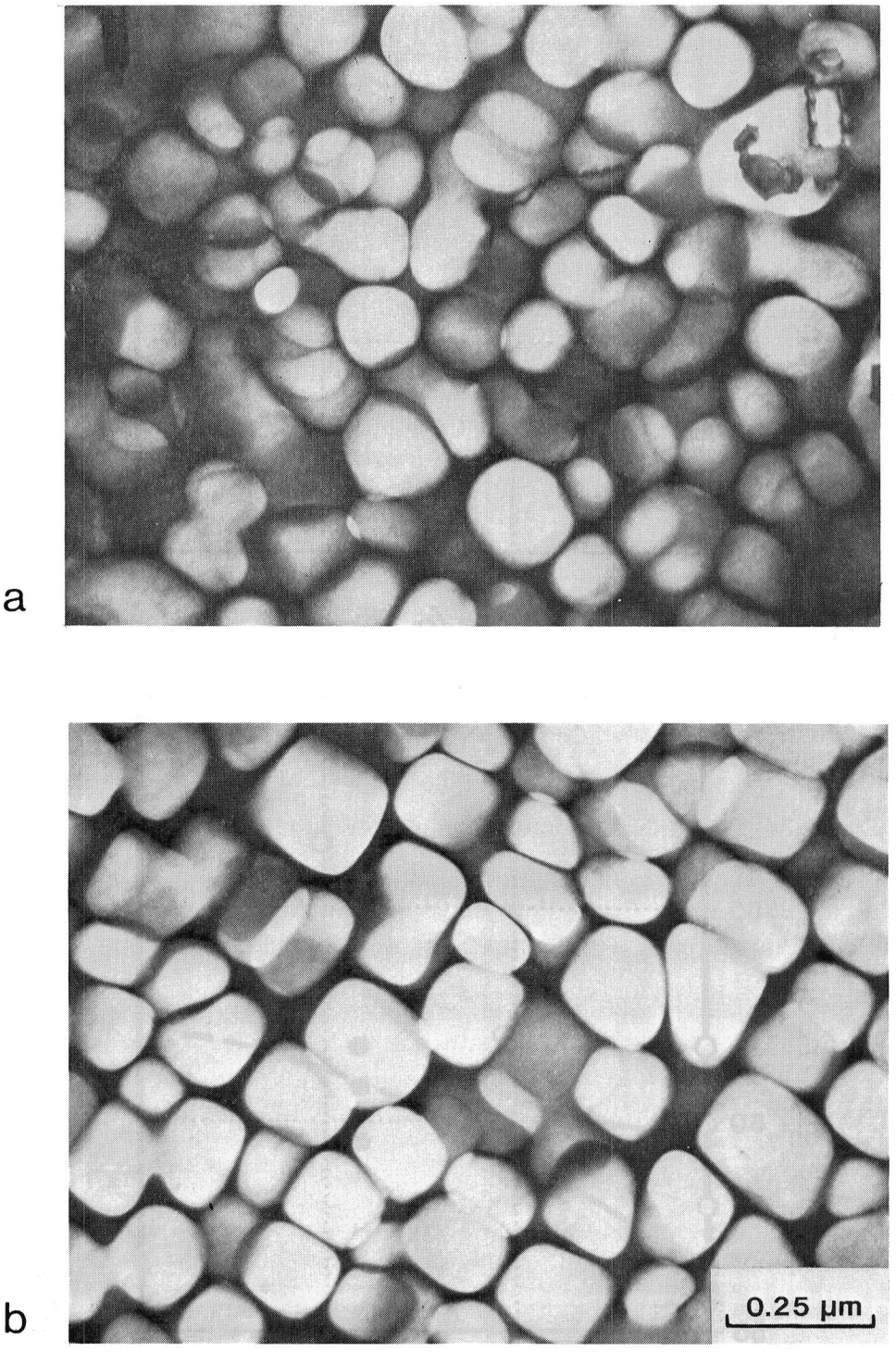

Figure 9. TEM dark field image micrographs of the normal carbon heat treated Mar-M247 type alloys showing the γ' morphology in (a) alloy E and (b) alloy G.

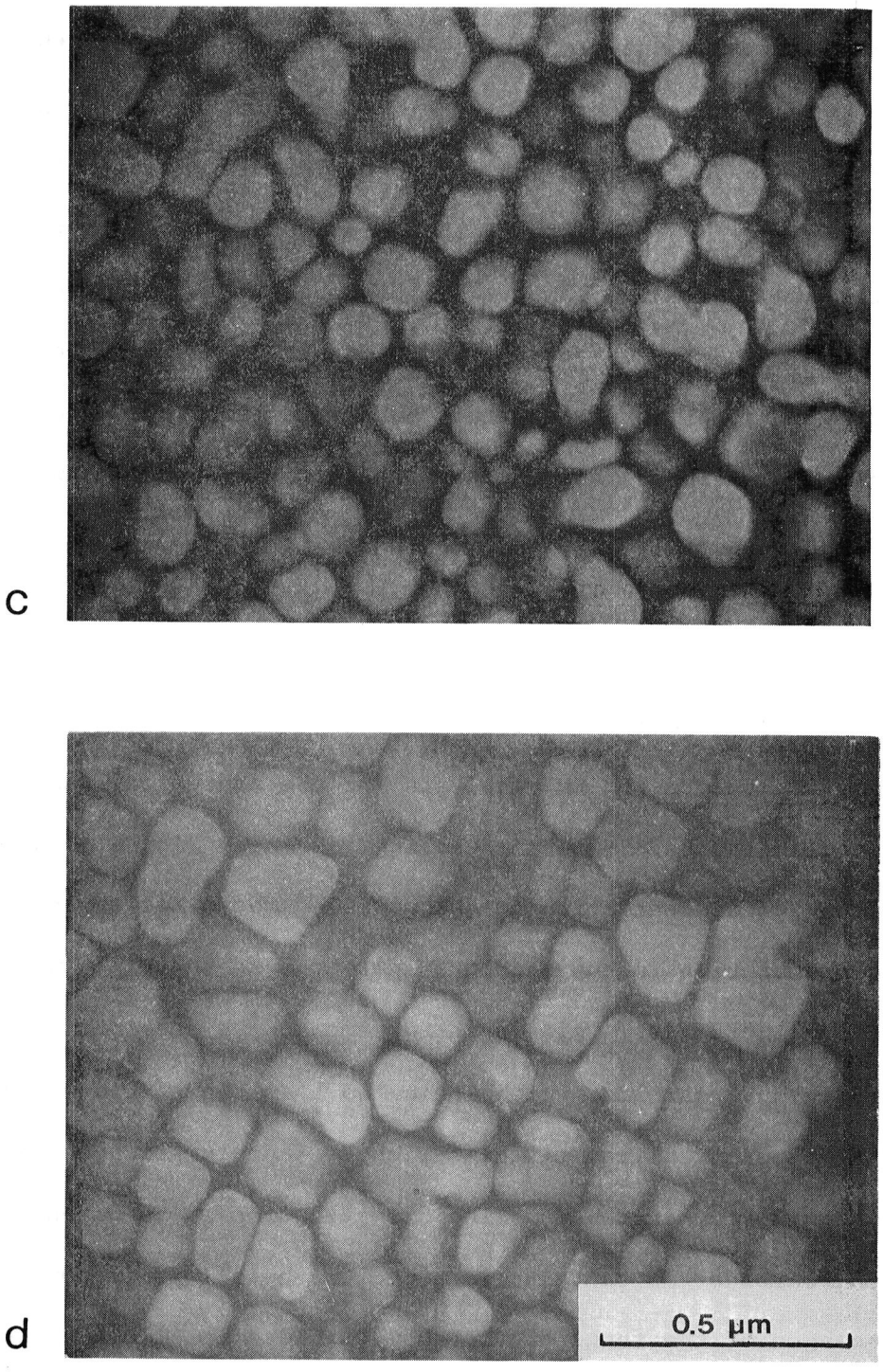

Figure 9. TEM dark field image micrographs of the LC heat treated Mar-M247 type alloys showing the γ' morphology in (c) alloy H and (d) alloy J.

increased (Figure 10a); these measurements were made directly on TEM micrographs. Based on the phase extraction results, the weight fraction of γ' was found to increase as the level of tantalum increased as shown in Figure 8b for both sets of alloys. X-ray diffraction studies performed on the residues revealed a slight increase in the lattice parameter of γ' from 0.3575nm to 0.3585 nm as tantalum increased (Figure 10b). However, γ-γ' peak separation could not be resolved on bulk single crystal specimens orientated for diffraction from specific planes at high 2θ angles. This indicates that the mismatch between γ and γ' is negligible at room temperature.

B. Phase Chemistry and Elemental Partitioning

The composite composition of carbides in the normal carbon alloys was analyzed using EDX analysis and the analytical ZAF correction program in the SEM on the carbide residue. Figure 11 shows that the titanium concentration in the carbides decreases and the tantalum concentration in the carbides increases as the tantalum content in the alloy increases. This is in agreement with the in-situ EDX analysis on individual carbides which indicated that the carbides underwent a change in composition from titanium-rich to tantalum-rich as the tantalum level of the alloy increased. The dramatic drop in tungsten concentration in the carbides as tantalum is added to the alloys is consistent with the absence of the tungsten-rich M_6C carbides in alloys F and G. The presence of chromium in the carbide residue is attributed to the $M_{23}C_6$ carbides being predominantly $Cr_{23}C_6$ carbides.

The composition of the γ' phase was determined by using the Inductive Coupled Plasma, Atomic Emission Spectroscopy (ICP) method at

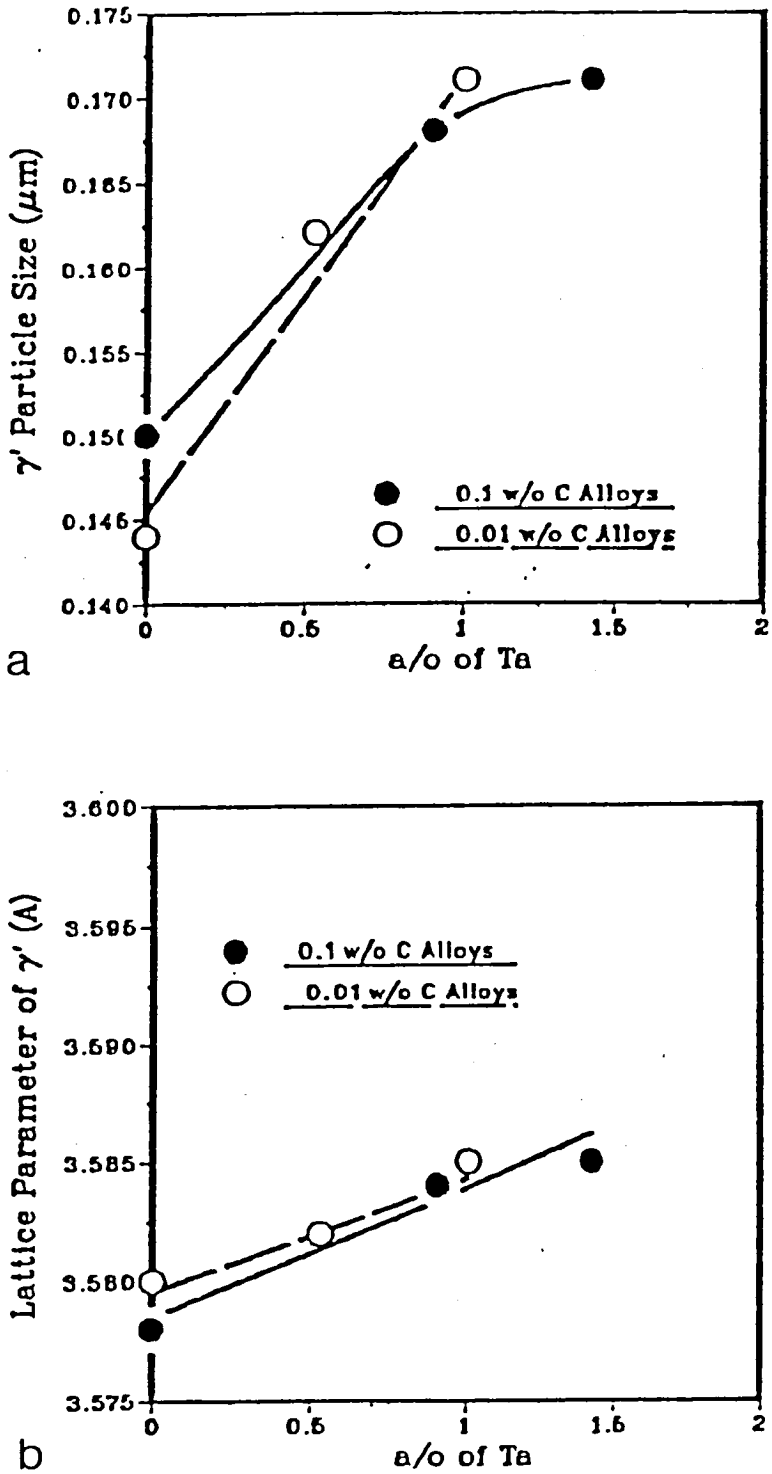

Figure 10. γ' particle size (a) and γ' lattice parameter (b) as a function of the Ta level in the alloys.

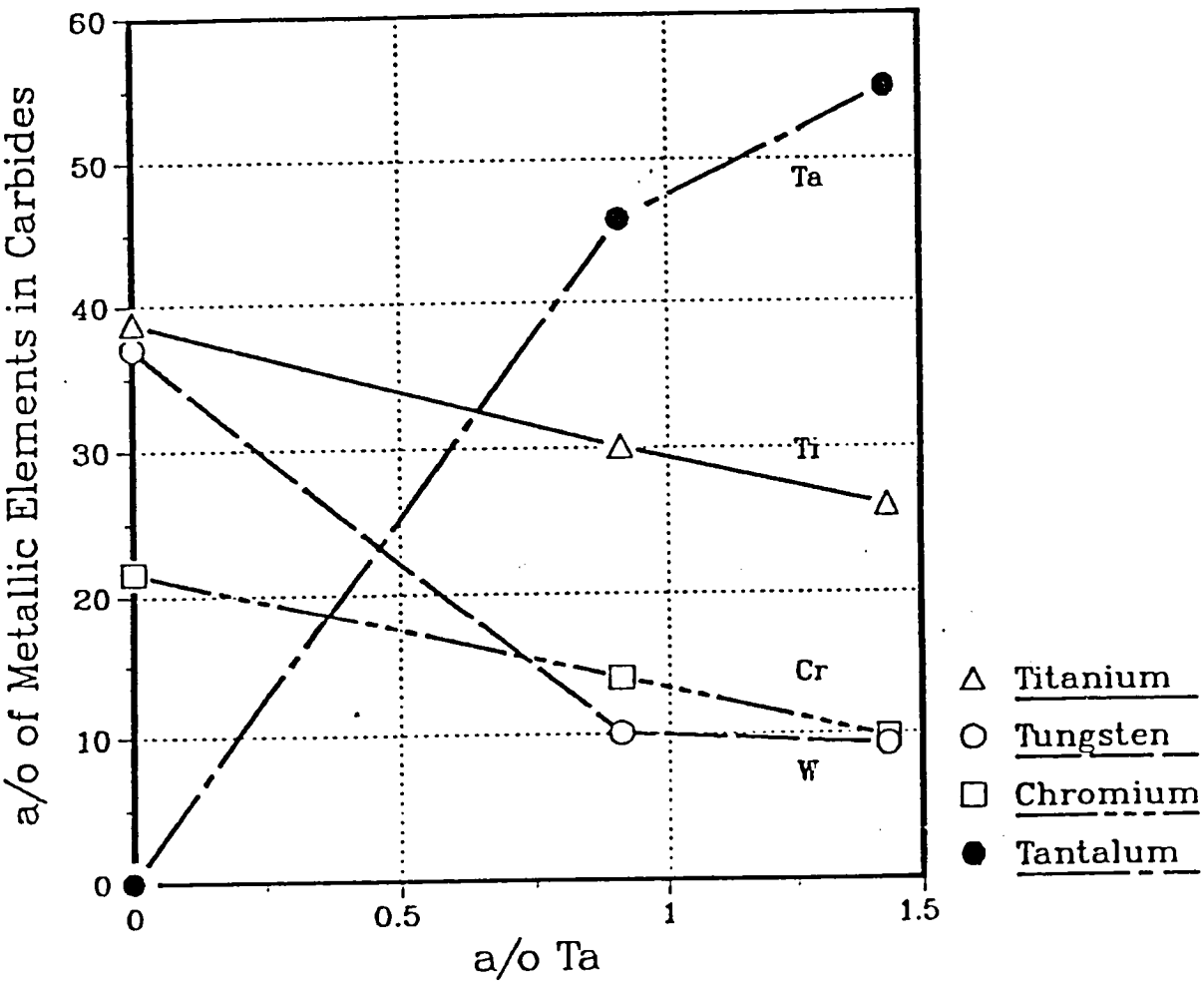

Figure 11. Composite composition of carbides as a function of Ta level in the Mar-M247 type alloys.

NASA-Lewis Research Center in Cleveland, Ohio on the extracted residue from fully heat treated specimens of all six alloys. In the normal carbon alloys, as the bulk tantalum content in the alloy increases, there is a slight decrease in the concentration of chromium, tungsten and aluminum in the γ' phase and no change in the molybdenum and titanium concentrations (Figure 12a); the cobalt level in γ' increases slightly as the bulk tantalum level increases. There is, however, a sharp increase in the tantalum concentration in γ' as the bulk level of tantalum in the alloy increases. Using the results of the γ' phase analysis, the carbide analysis and the bulk alloy chemistry, the composition of the γ phase was calculated using a mass balance technique. The results are shown in Figure 12b. The concentration of every alloying element in the γ phase increases as the bulk tantalum content in the alloy increases.

The γ' phase chemistry of the LC alloys is consistent with the γ' phase chemistry of the normal carbon alloys in that minor or no change in concentration of the various elements with the exception of tantalum occur as the bulk tantalum content in the alloy is varied (Figure 13a). Specifically, no change in the concentration of tungsten or molybdenum and possibly aluminum takes place as tantalum was varied, and only small decreases in the concentration of cobalt and chromium and a small increase in the titanium concentration is observed as the bulk tantalum content increases. Again, there is a sharp increase in tantalum concentration in γ' as the tantalum content of the alloy increases. Also consistent with the γ phase chemistry of the normal carbon alloys, Figure 13b shows that with the possible exception of tantalum, the

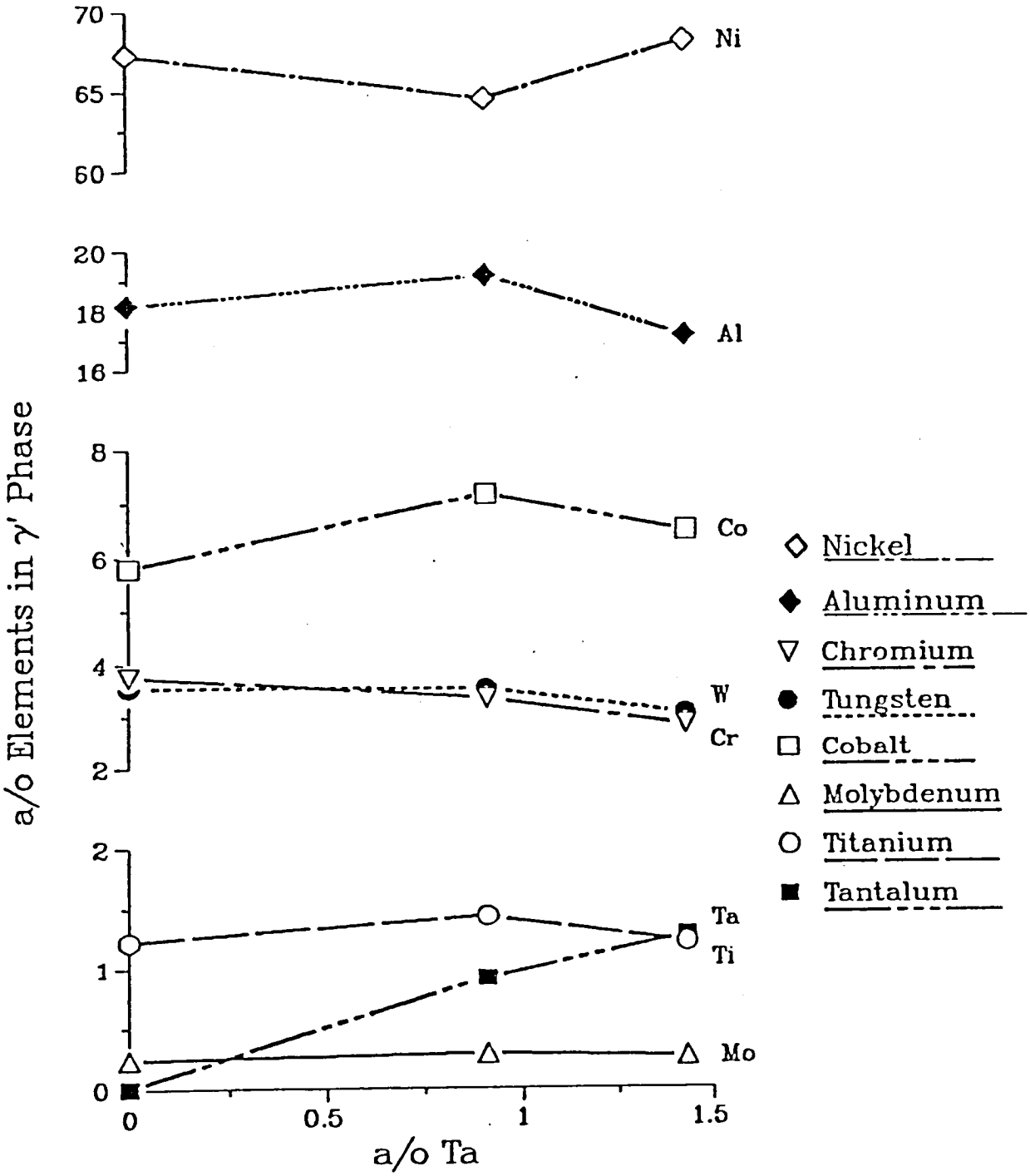

Figure 12a. Composition of the γ' phase in the normal carbon Mar-M247 type alloys as a function of the Ta level in the alloys.

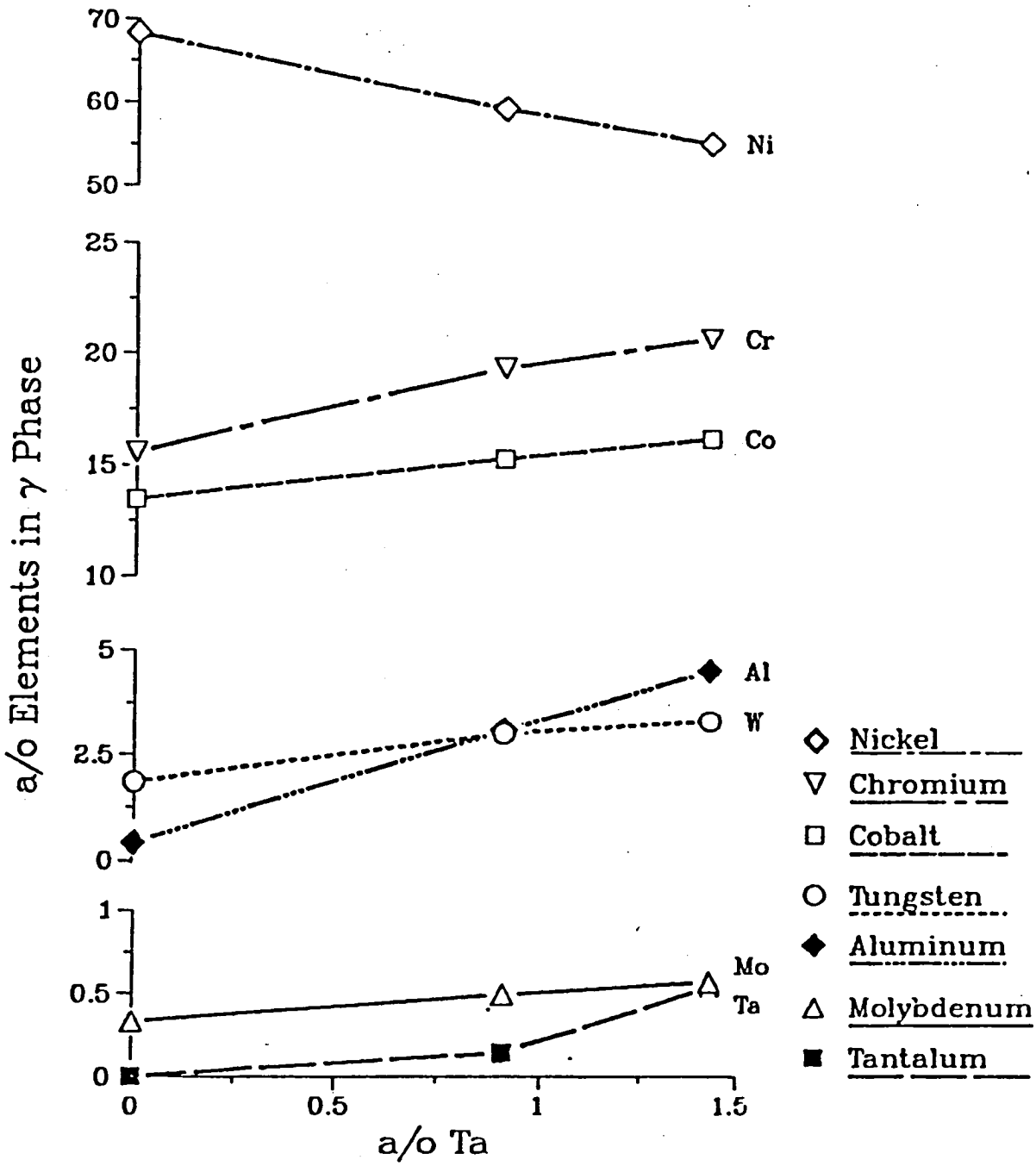

Figure 12b. Composition of the γ phase in the normal carbon Mar-M247 type alloys as a function of Ta level in the alloys.

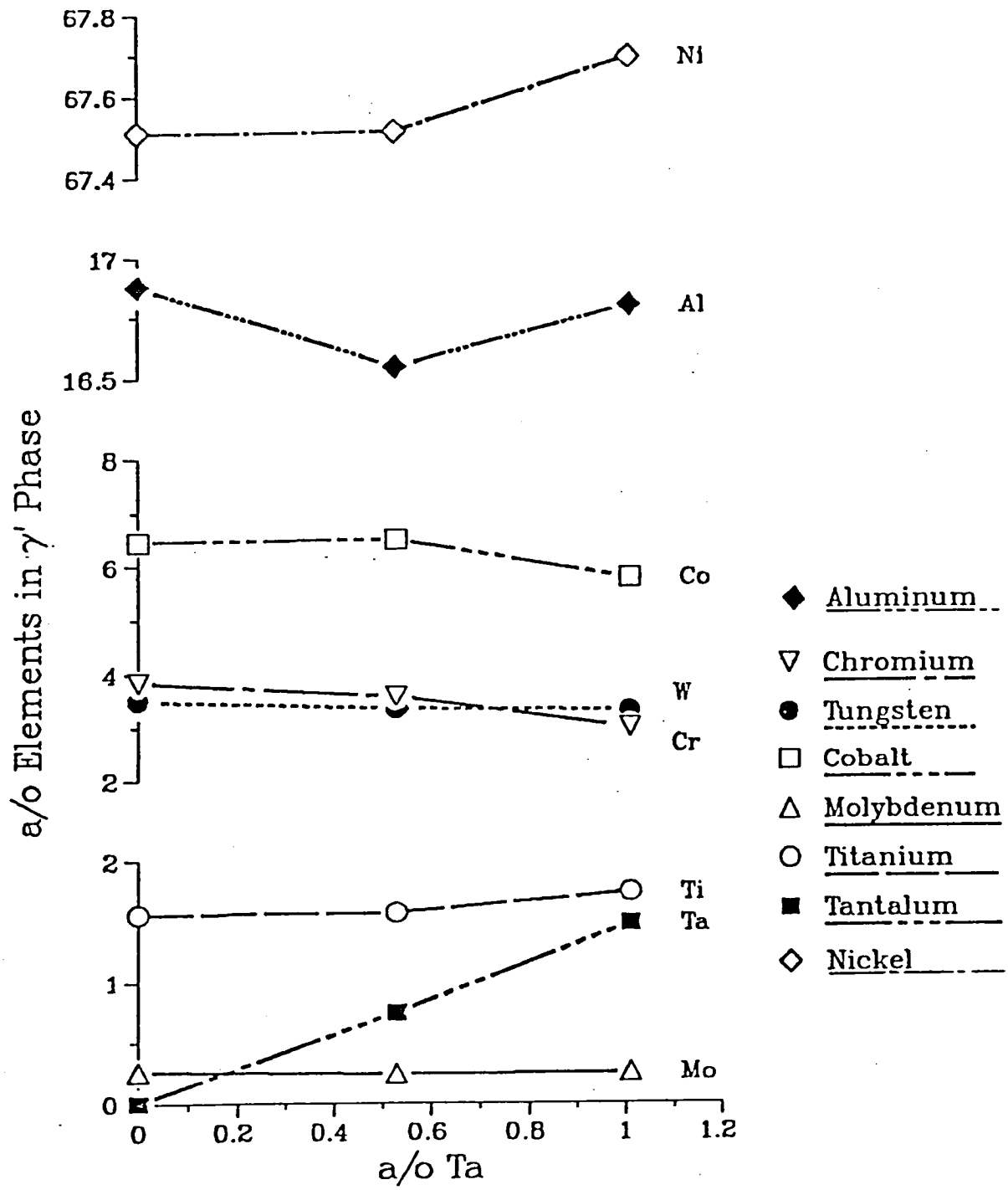

Figure 13a. Composition of the γ' phase in the LC Mar-M247 type alloys as a function of Ta level in the alloys.

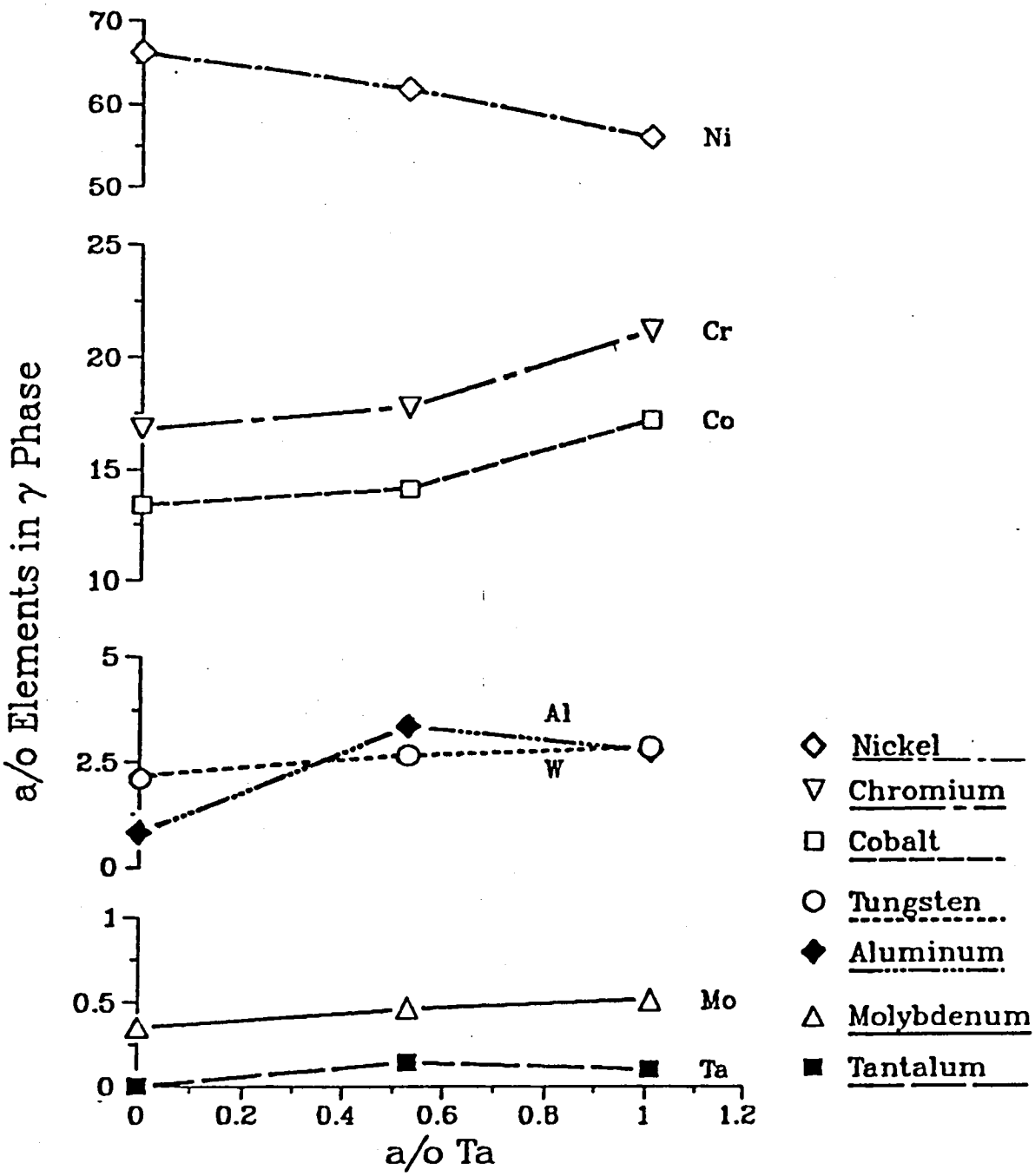

Figure 13b. Composition of the γ phase in the LC Mar-M247 type alloys as a function of Ta level in the alloys.

concentration of each element in the γ phase increases as the bulk tantalum content increases.

The dependence of the concentration of the various alloying elements in the γ and γ' phases on the bulk tantalum content should be viewed with caution. The levels of these various alloying elements were not kept constant in the bulk alloy chemistries (see Table 2). However, the partitioning of the elements between the γ and γ' phases should not be strongly affected by slight variations in the overall bulk alloy chemistries. Thus the partitioning behavior, defined as the ratio of concentration of an element in γ' to the concentration in γ, gives a better indication of the changes in γ' and γ phase chemistry as a function of tantalum content. As shown in Figures 14a and 14b, the molybdenum, cobalt, and chromium partitioning ratios do not vary much as the bulk tantalum level in the alloy increases; these elements are predominantly located in the γ phase (partitioning ratio less than 1). Aluminum partitions strongly to the γ' (as expected) and so does tungsten to a lesser extent. Somewhat surprisingly for aluminum and as expected for tungsten, as the bulk tantalum content in the alloy increases, the partitioning ratios decrease indicating that both of these elements have a stronger preference to partition to the γ phase with increasing tantalum content. Both Figures 14a and b indicate that partitioning of aluminum to γ depends only on whether or not tantalum is present in the alloy (since the partitioning ratio of aluminum in any alloy containing tantalum is approximately the same). Tantalum shows the opposite behavior; its concentration increases in the γ' as the tantalum content in the alloy increases. All the titanium in the alloy

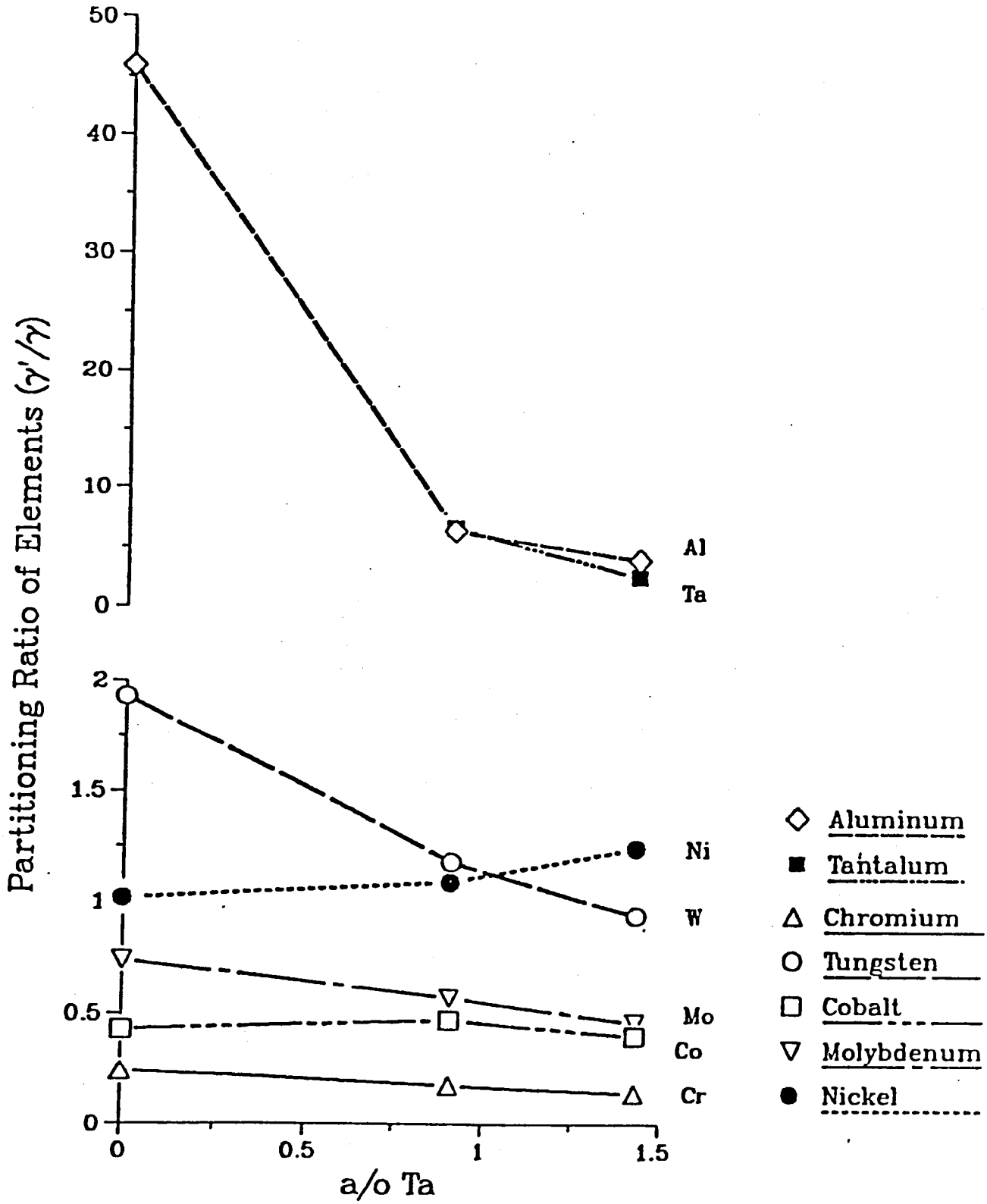

Figure 14a. Partitioning ratio of elements between γ and γ' in normal carbon Mar-M247 type alloys as a function of Ta level in the alloys.

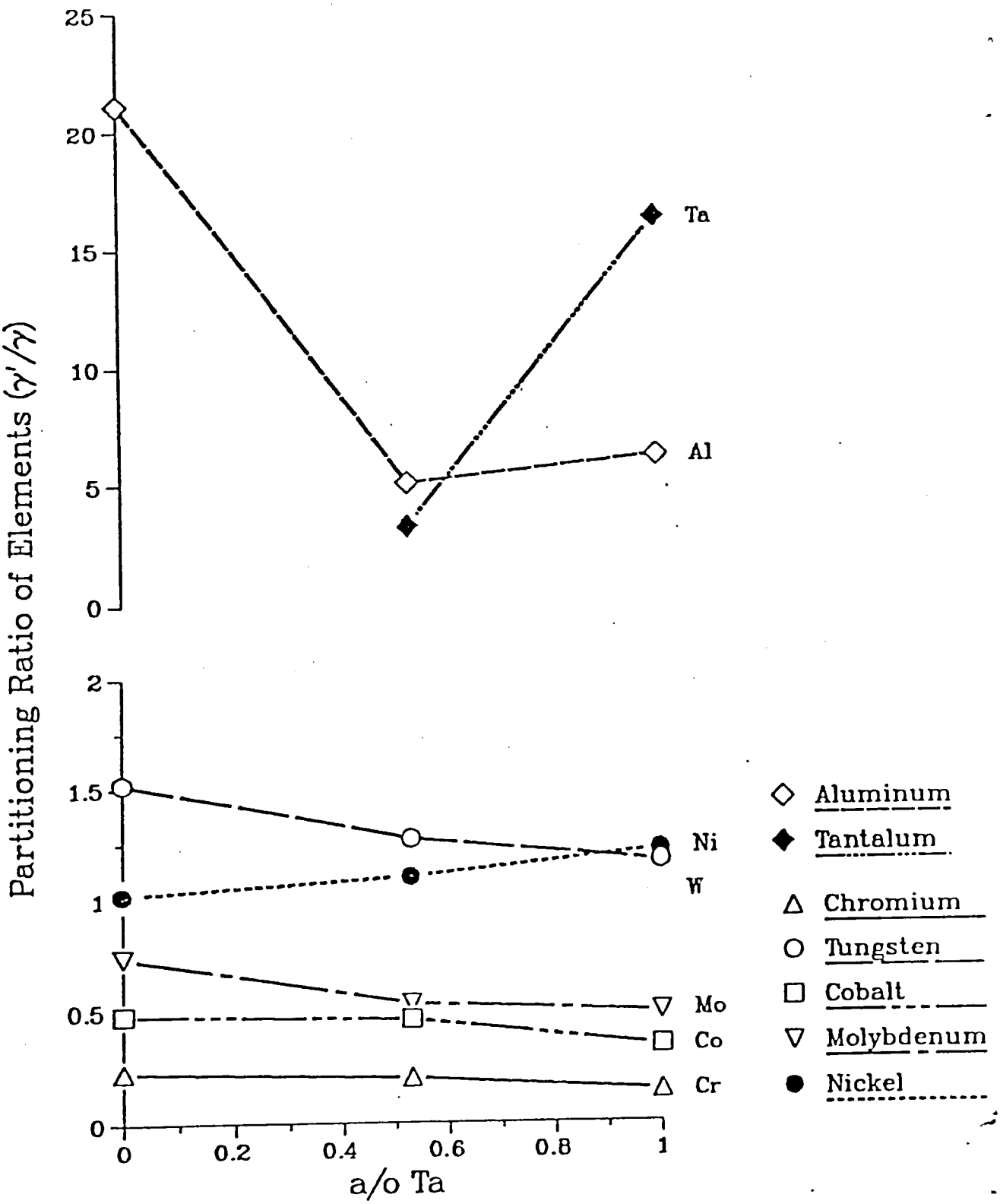

Figure 14b. Partitioning ratio of elements between γ and γ' in LC Mar-M247 type alloys as a function of Ta level in the alloys.

(with the exception of the fraction which goes into the MC carbides) is believed to partition to γ'.

C. Mechanical Properties

Tensile Properties

A single tensile test was performed at 540°C (1000°F) and 760°C (1400°F) and two tensile tests at 982°C (1800°F) for each alloy. The results are presented in Table 5. The critical resolved shear stress (CRSS) was calculated based on the maximum Schmid factor determined for each specimen from Laue back-reflection x-ray patterns and using the $\{111\}\langle 1\bar{1}0\rangle$ slip system.

As shown in Figure 15, the CRSS is independent of temperature up to about 760°C (1400°F), consistent with the general behavior of nickel-base superalloys. Between 760°C and 982°C (1800°F), there is a rapid decrease in strength of about 200 MPa for each alloy. The effect of tantalum on the CRSS is also seen in Figure 15; at lower temperatures, there is a strong increase in the CRSS with increasing tantalum while in either alloy series at the highest temperature (982°C), the effect of tantalum on increasing the CRSS is less pronounced. A plot of the tensile strength versus tantalum content in Figure 16 also demonstrates the beneficial effect of tantalum on tensile strength. The tensile strengths show a similar dependence on temperature as the CRSS in Figure 15, in that the tantalum effect on tensile strength is less pronounced at 982°C.

The tensile ductilities, both elongation and reduction in area, of all six alloys are plotted as a function of the tantalum content in the alloy in Figures 17a and b. In general, the ductility in each alloy series decreases as the tantalum content increases. However, at the

Table 5. Tensile Properties of the Mar-M247 Type Alloys

Alloy	Temperature (°C)	0.2% Yield Strength (MPa)	UTS (MPa)	Ductility % Elong.	Ductility % RA	CRSS (MPa)
E	540	877	980	8.2	11.5	383
	760	853	1028	5.9	10.2	392
	982	424	468	19.0	22.8	179
	982	470	496	23.7	35.3	213
F	540	974	1005	6.2	7.8	412
	760	1007	1247	3.4	4.7	411
	982	488	630	20.9	26.1	222
	982	462	618	14.8	20.1	189
G	540	1007	1046	4.2	4.8	458
	760	929	994	5.4	5.0	437
	982	--	643	19.1	24.5	--
	982	531	632	19.2	20.3	248
H	540	810	892	23.0	21.6	348
	760	929	994	16.1	20.3	437
	982	--	500	36.6	57.3	--
I	540	898	952	17.1	20.4	395
	760	934	1100	9.1	10.7	408
	982	494	572	35.4	51.4	221
	982	487	571	25.5	41.9	219
J	540	976	982	9.8	10.1	434
	760	922	1025	10.3	15.1	410
	982	513	617	29.5	43.1	232
	982	561	629	29.3	40.9	261

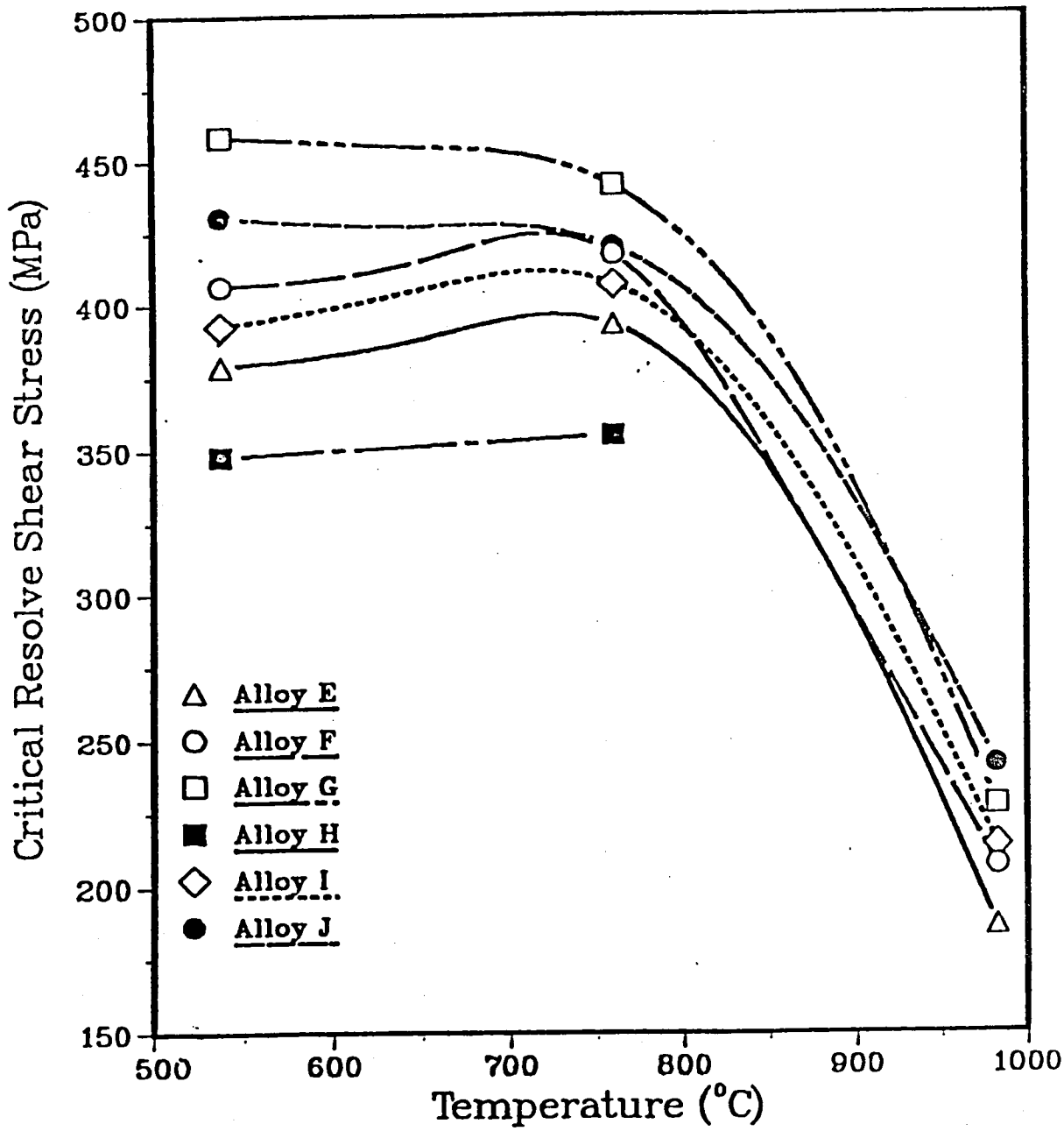

Figure 15. Temperature dependence of CRSS for the Mar-M247 type alloys. Note the strong effect of the Ta level in the alloys on the CRSS at lower temperatures.

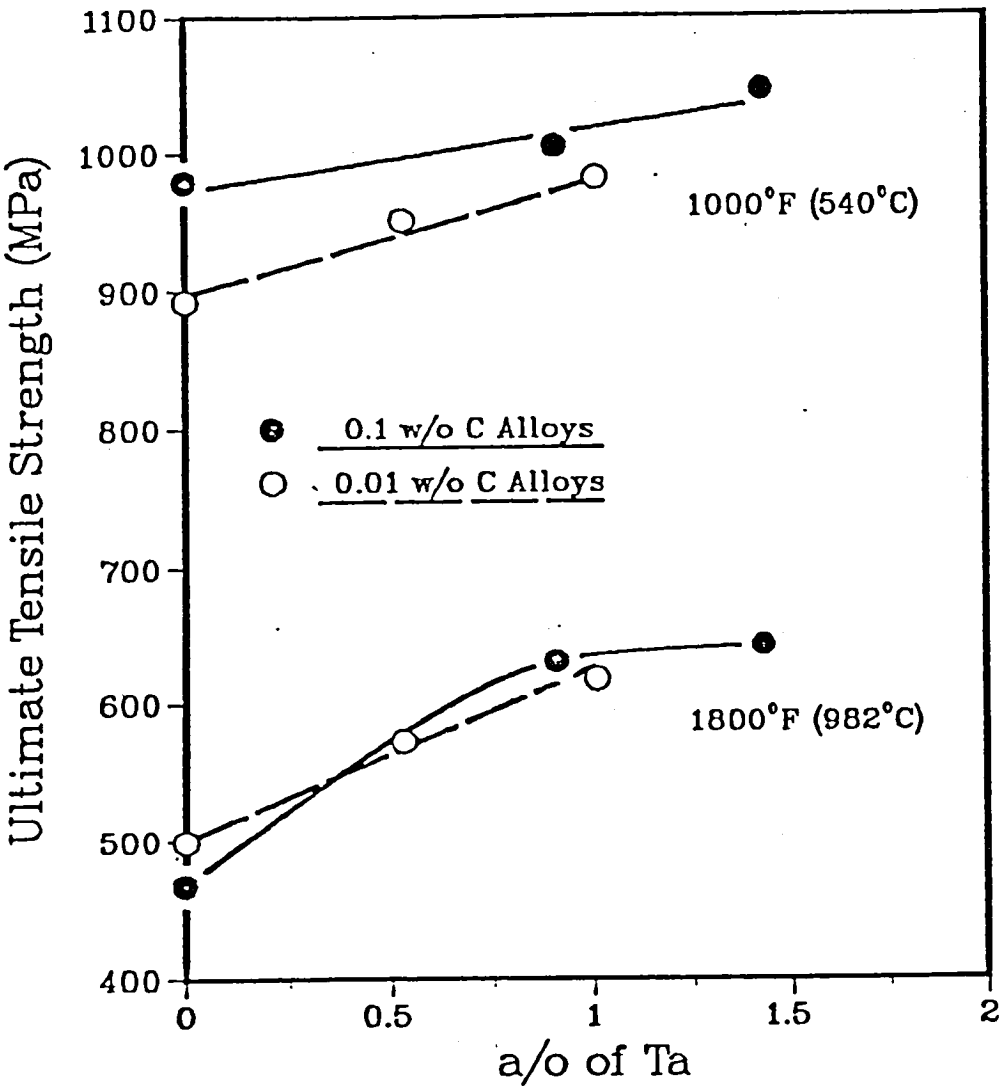

Figure 16. The effect of the bulk Ta level on the ultimate tensile strength of the Mar-M247 type alloys. Note the temperature dependence of the UTS.

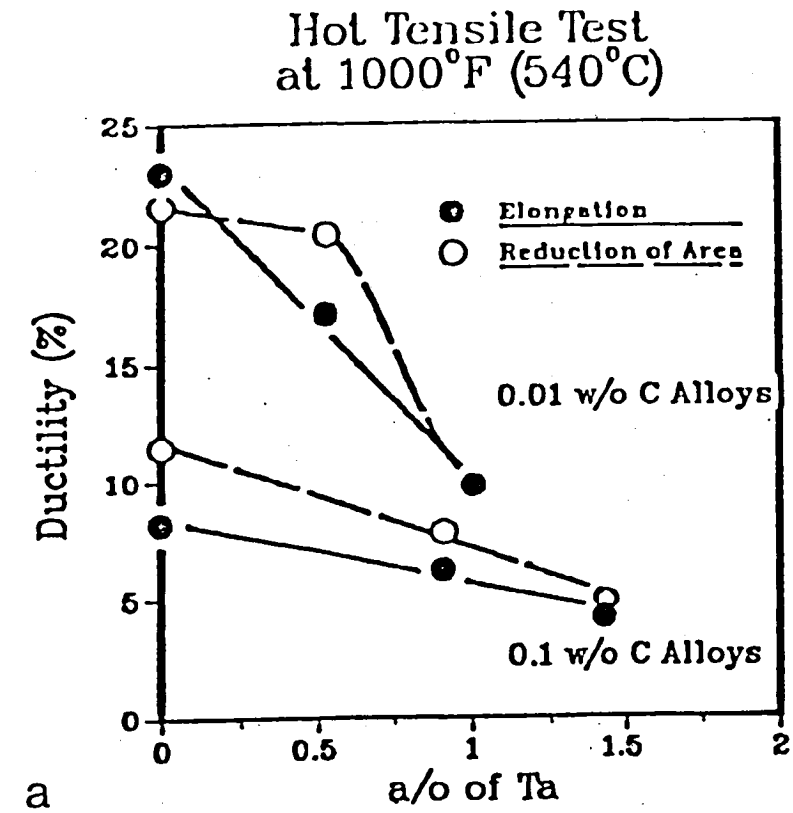

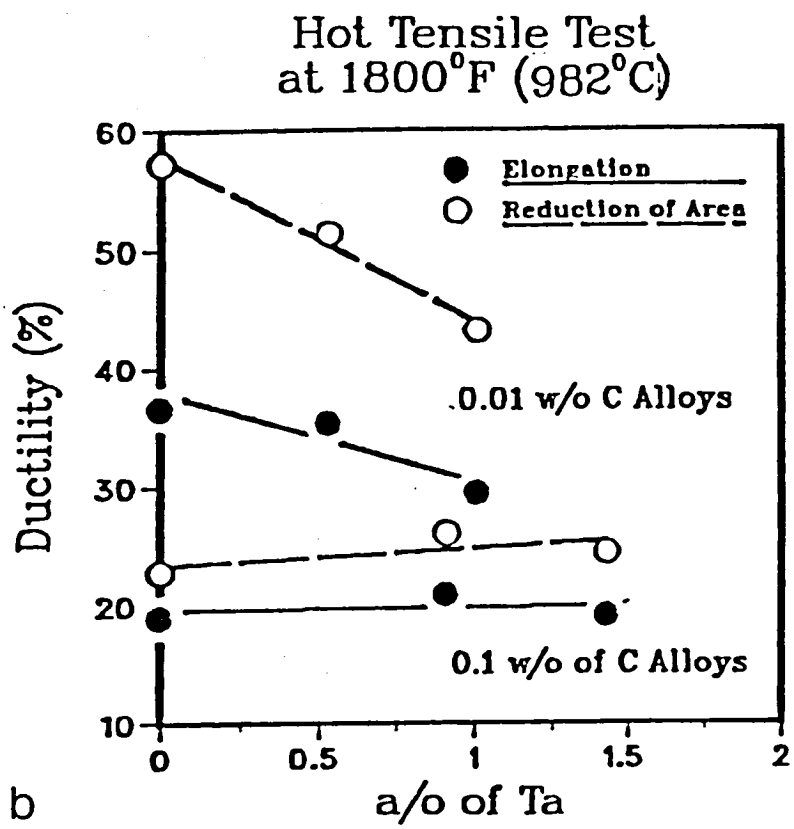

Figure 17. Tensile ductility properties of the alloys at 540°C (a) and 982°C (b) as a function of the Ta level in the alloys.

highest temperature (982°C), ductilities of the normal carbon alloys (E, F and G) seem to be independent of the tantalum content. In addition, there is a difference in ductility between the normal carbon and LC series of alloys with the latter exhibiting more ductility than the former.

Creep Rupture Properties

Creep tests were performed at 760°C (1400°F), 871°C (1600°F), and 982°C (1800°F) using various stress levels. Some of the tests were discontinued before rupture occurred and the creep rupture data of all six alloys are summarized in Table 6. Representative creep curves of all alloys at 760°C (1400°F) in Figures 18a and 18b display the expected primary and secondary creep regions; with the exception of alloys E and H, these tests were discontinued before rupture so the tertiary region was not observed. At higher temperature and high stress (982°C and 276 MPa), the primary creep region does not occur but the secondary and tertiary regions are clearly visible as shown in Figures 19a and 19b.

The creep curves for either set of alloys in Figures 18 and 19 indicate the strong influence of tantalum on creep behavior; the secondary creep rate decreases and the rupture time increases as the bulk tantalum level in the alloy increases. These trends can also be examined in Larson-Miller plots. A Larson-Miller plot is a parametric method used to extrapolate creep rupture data in which the applied stress is plotted versus the Larson-Miller parameter defined as $T(20+\log t_f)$ where T is the temperature in degrees Rankine and t_f is the rupture time. The Larson-Miller plots for both series of alloys are shown in Figures 20a and b. For our purposes, it is sufficient to examine the applied stress required to attain a certain Larson-Miller

Table 6. Creep Rupture Properties of the Mar-M247 Type Alloys

Alloy	Temperature (°C)	Stress (MPa)	Rupture Time (Hr)	$\dot{\varepsilon}_s$ (10^{-7}) (sec^{-1})	Ductility	
					% Elong.	% RA
E	760	690	57.4	4.80	21.7	23.4
	871	414	25.7	2.05	25.7	36.8
	871	345	124.6	8.60	28.3	36.8
	982	276	3.3	20.00	31.4	40.6
	982	138	--	0.26	--	--
F	760	690	--	0.80	--	--
	871	483	36.7	5.45	20.2	28.0
	871	414	--	1.50	--	--
	982	276	17.2	9.50	25.9	34.6
	982	207	81.8	0.88	22.6	40.0
G	760	690	--	0.12	--	--
	871	483	51.3	4.07	22.3	26.2
	871	414	--	0.90	--	--
	982	276	21.7	5.00	18.3	28.2
	982	207	111.0	0.73	23.7	33.8
H	760	690	49.2	5.50	26.7	34.6
	871	414	37.8	6.81	38.6	45.8
	871	379	82.5	2.50	31.0	43.8
	982	276	5.7	43.00	38.9	58.8
	982	172	102.5	0.83	37.4	50.4
I	760	690	--	2.00	--	--
	871	414	107.2	3.05	30.4	45.6
	871	414	--	1.30	--	--
	982	276	13.1	13.00	30.6	51.1
	982	207	70.4	0.18	35.4	49.3
J	760	690	--	0.55	--	--
	871	483	63.3	3.32	33.1	41.7
	871	414	--	0.80	--	--
	982	276	23.7	5.55	35.4	44.5
	982	207	122.3	0.76	34.0	43.2

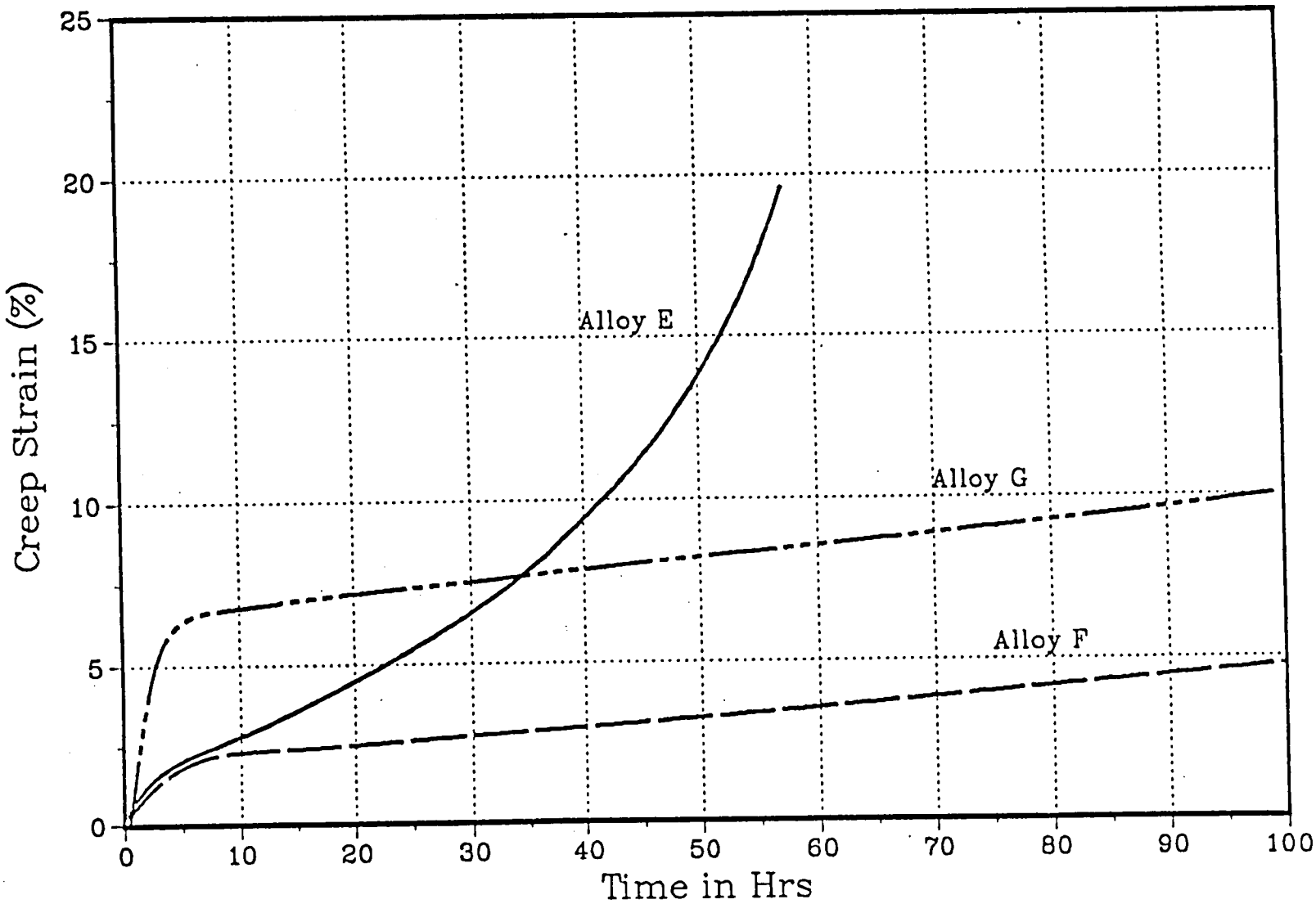

Figure 18a. Representative creep curves of the normal carbon Mar-M247 type alloys tested at 760°C and 690 MPa.

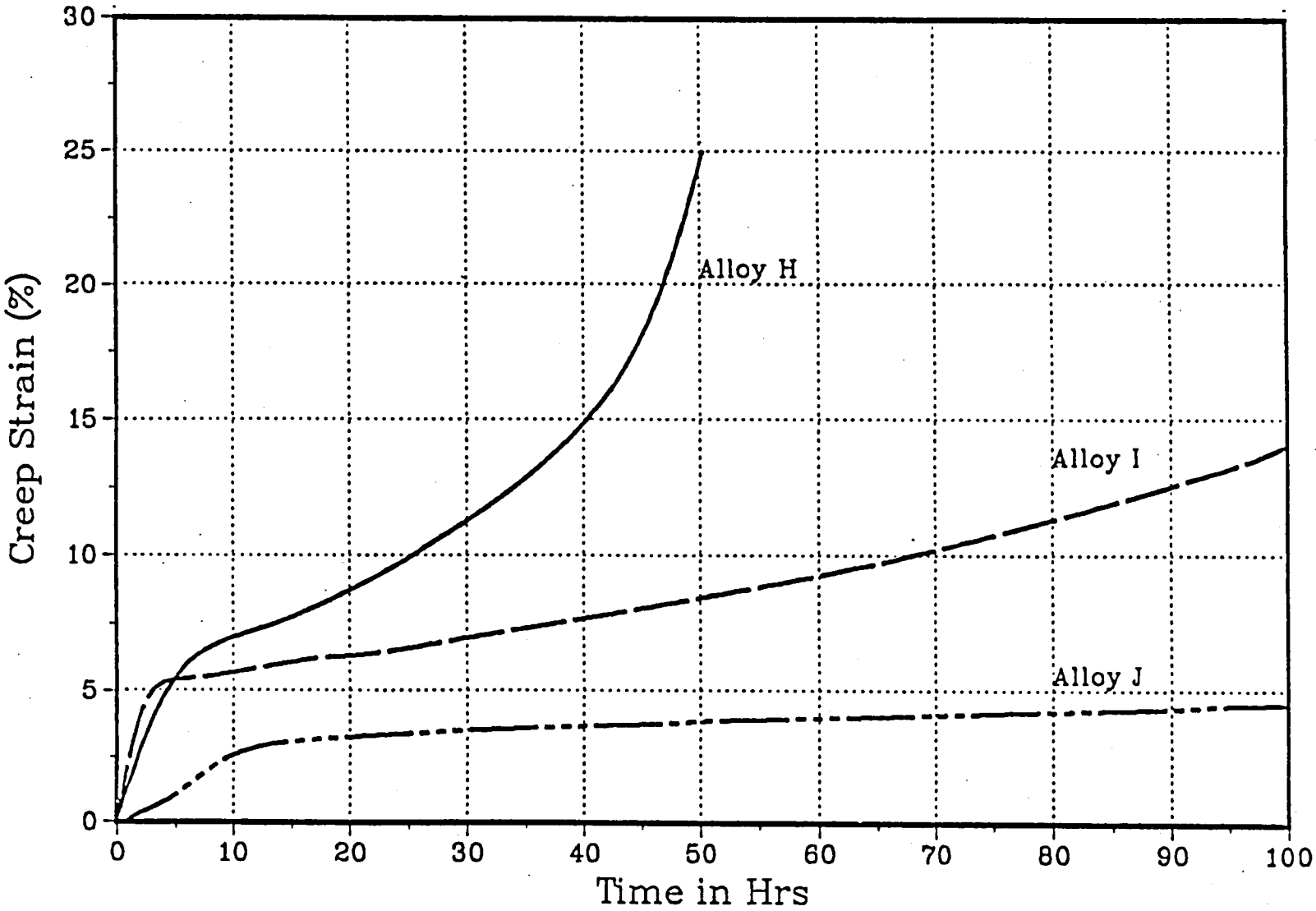

Figure 18b. Representative creep curves of the LC Mar-M247 type alloys tested at 760°C and 690 MPa.

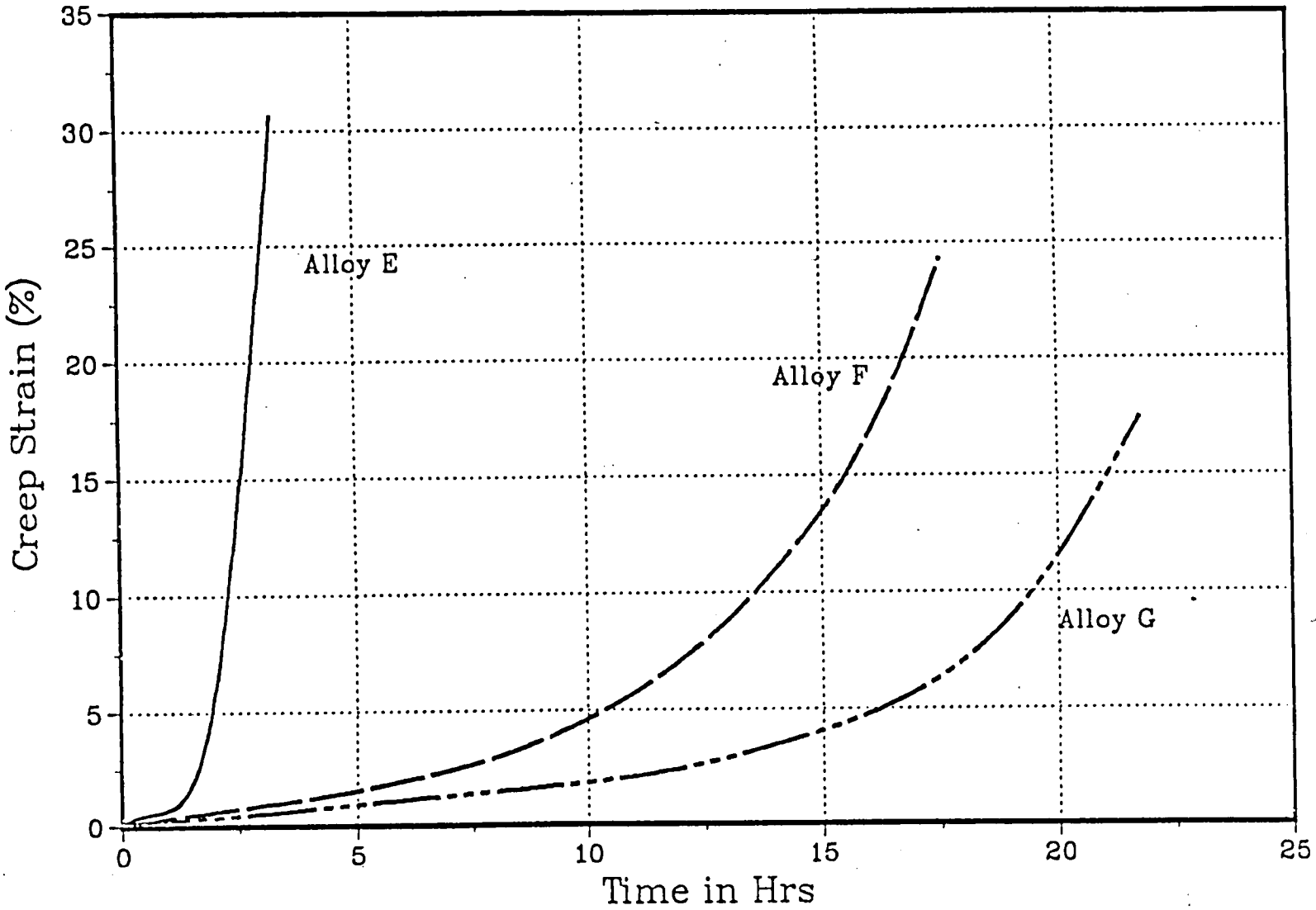

Figure 19a. Representative creep curves of normal carbon Mar-M247 type alloys tested at 982°C and 276 MPa.

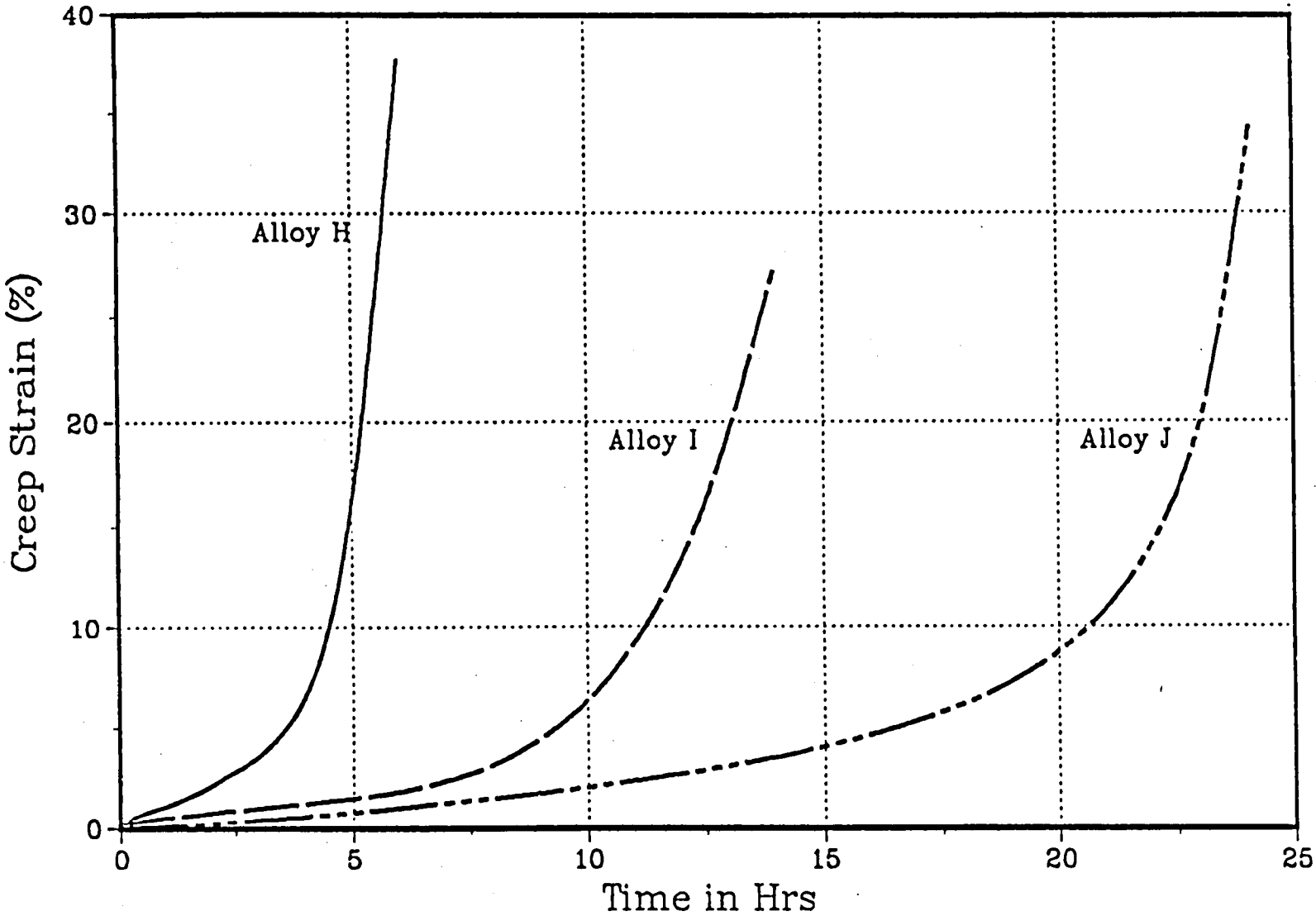

Figure 19b. Representative creep curves of LC Mar-M247 type alloys tested at 982°C and 276 MPa.

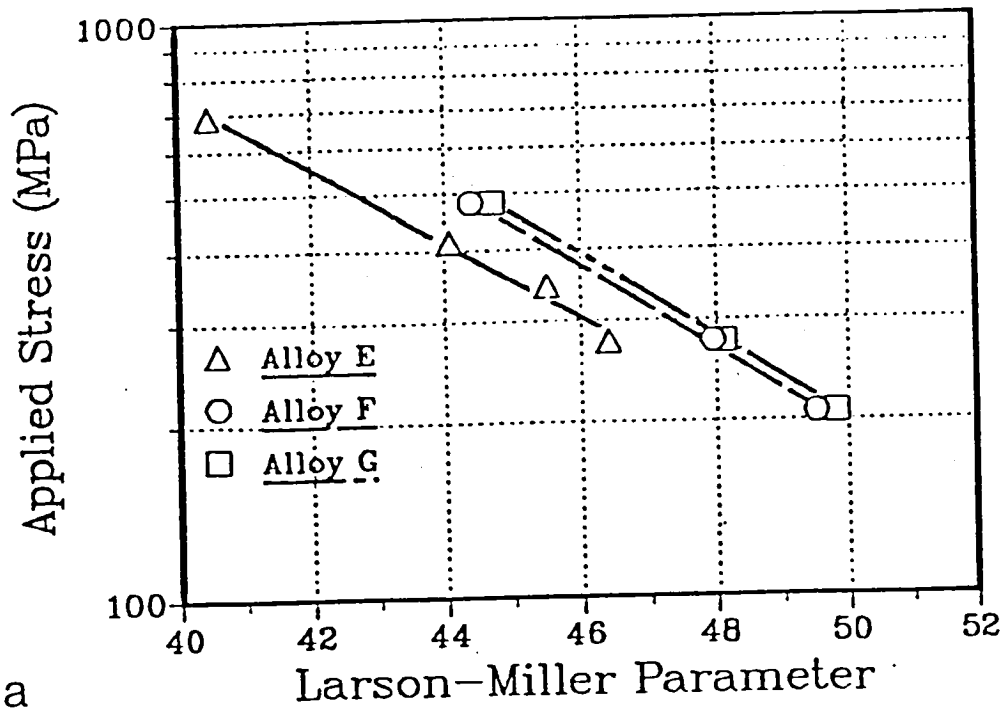

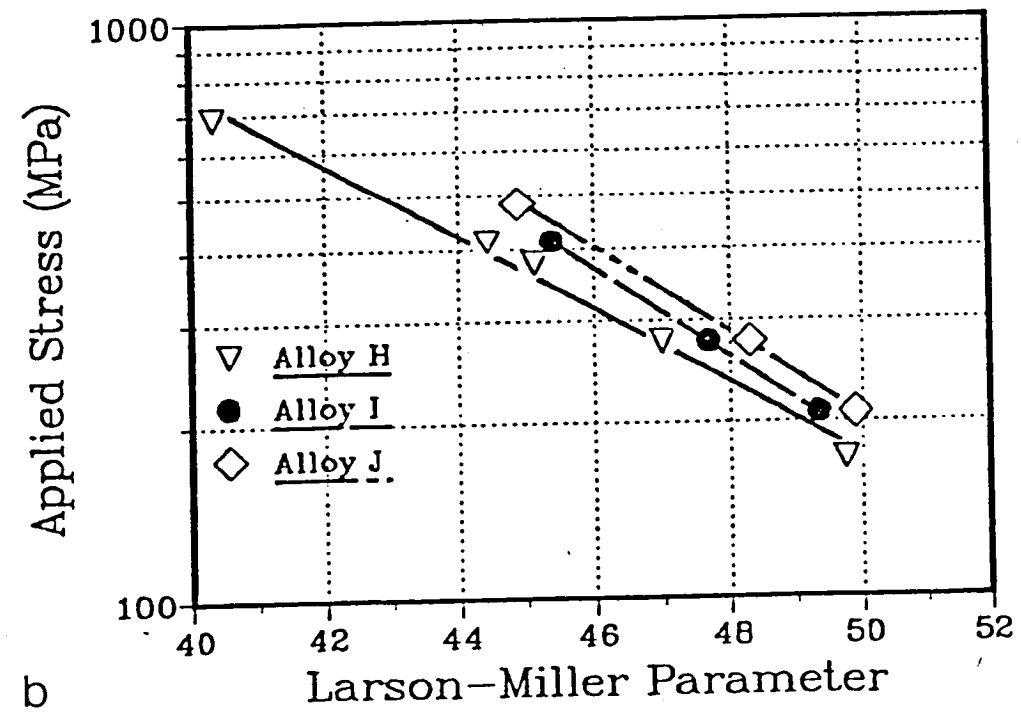

Figure 20. Larson-Miller plots of (a) normal carbon Mar-M247 and (b) LC Mar-M247 type alloys showing the effect of Ta level in the alloys on the rupture time of the alloys.
LMP = $(T+460)(20+\log t_f)(10^{-3})$

parameter value. From the definition of the Larson-Miller parameter, this would correspond to the stress required to obtain the same rupture time at the same temperature. It can be seen from either figure that the applied stress at a constant Larson-Miller parameter increases as the bulk tantalum level increases. Alternatively, at a constant applied stress, the Larson-Miller parameter increases as the bulk tantalum level in either series of alloys increases; if constant temperature is assumed, this corresponds to an increase in the rupture time with increasing tantalum content. Similar Larson-Miller plots can be generated using the secondary creep rates since the secondary creep rate is inversely proportional to the rupture time [58]. In these plots (Figure 21), a larger stress is required to attain the same Larson- Miller parameter (i.e., the same secondary creep rate) as the bulk tantalum level in the alloy increases. Alternatively, at constant applied stress, the Larson-Miller parameter increases as the bulk tantalum level in the alloy increases and assuming constant temperature, this corresponds to a decreasing secondary creep rate with increasing tantalum content.

The influence of carbon on the creep rupture properties can also be assessed from these data. Representative creep curves of several alloys from each alloy series are plotted together in Figure 22. At each tantalum level, the secondary creep rate is lower and the rupture time is greater for the LC alloy compared to the normal carbon alloy. The influence of carbon on the rupture time is more readily illustrated in Figure 23 where the rupture time of alloys with the same tantalum content and the two carbon levels are compared at the same stress and temperature; the LC alloys always exhibit longer rupture times.

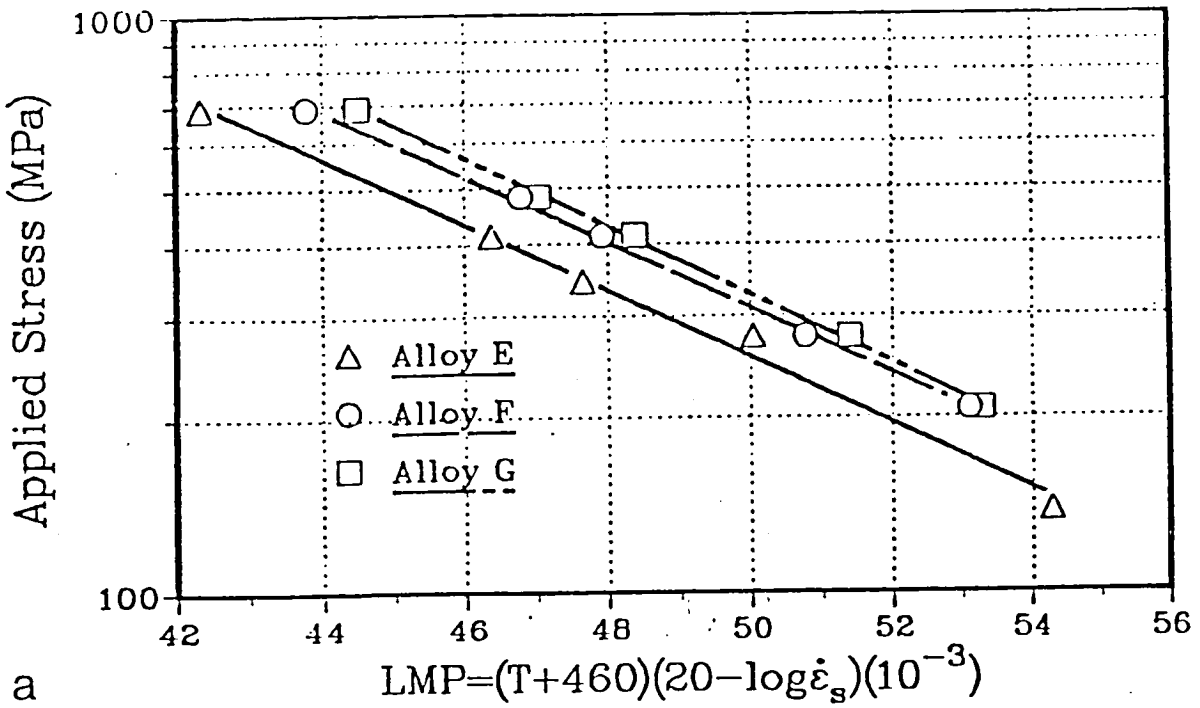

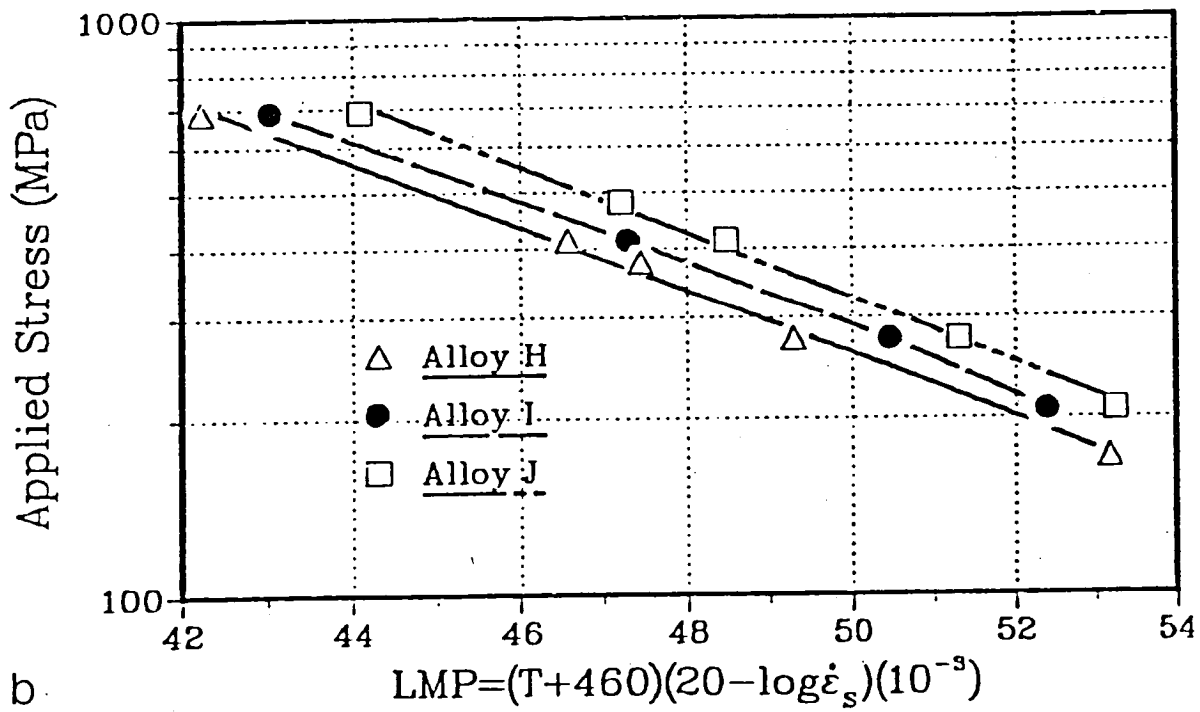

Figure 21. Larson-Miller plots of (a) normal carbon Mar-M247 and (b) LC Mar-M247 type alloys showing the influence of Ta level in the alloys on the secondary creep rates.

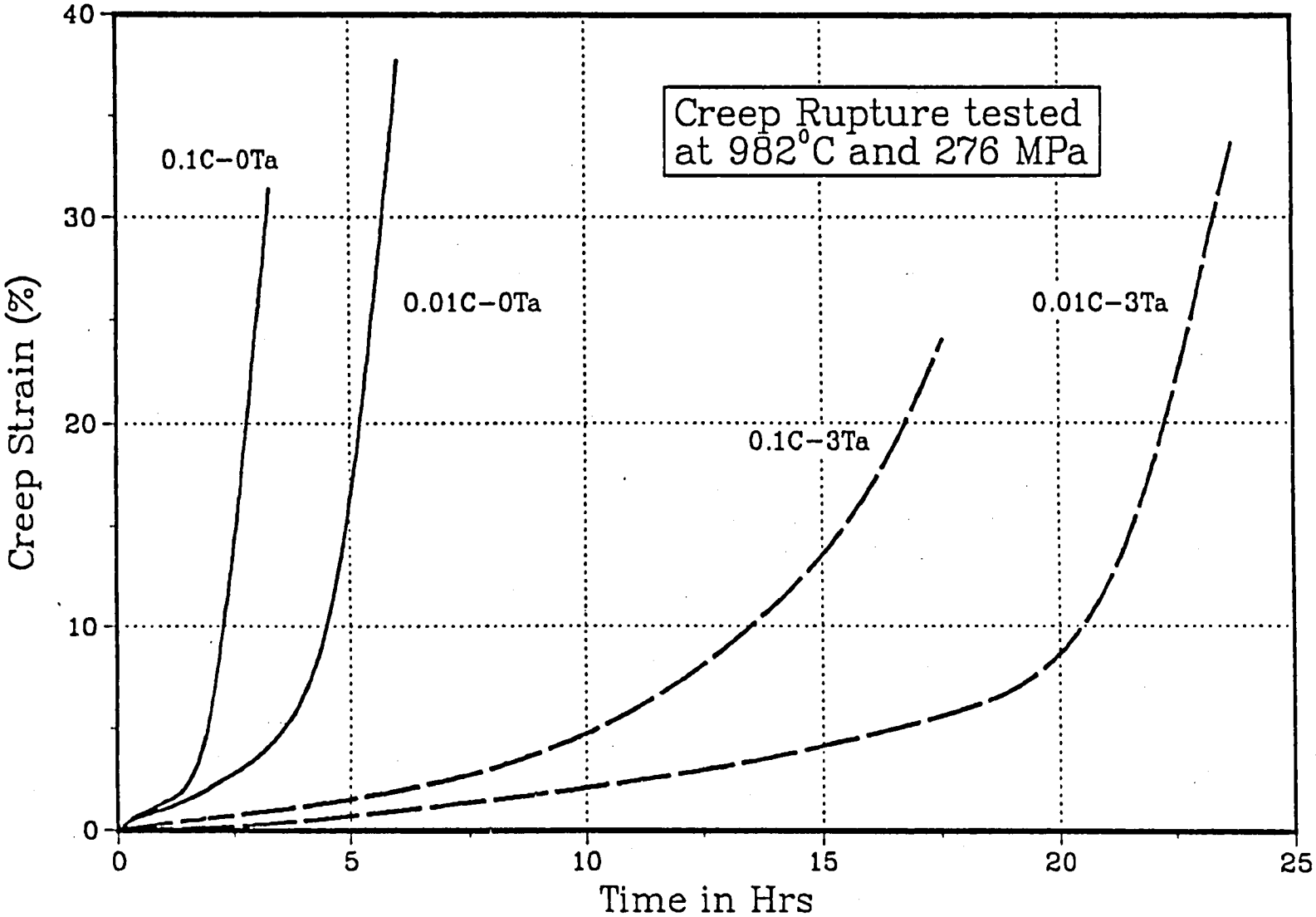

Figure 22. Representative creep curves of several alloys tested at 982°C and 276 MPa with various Ta and C levels in the alloys.

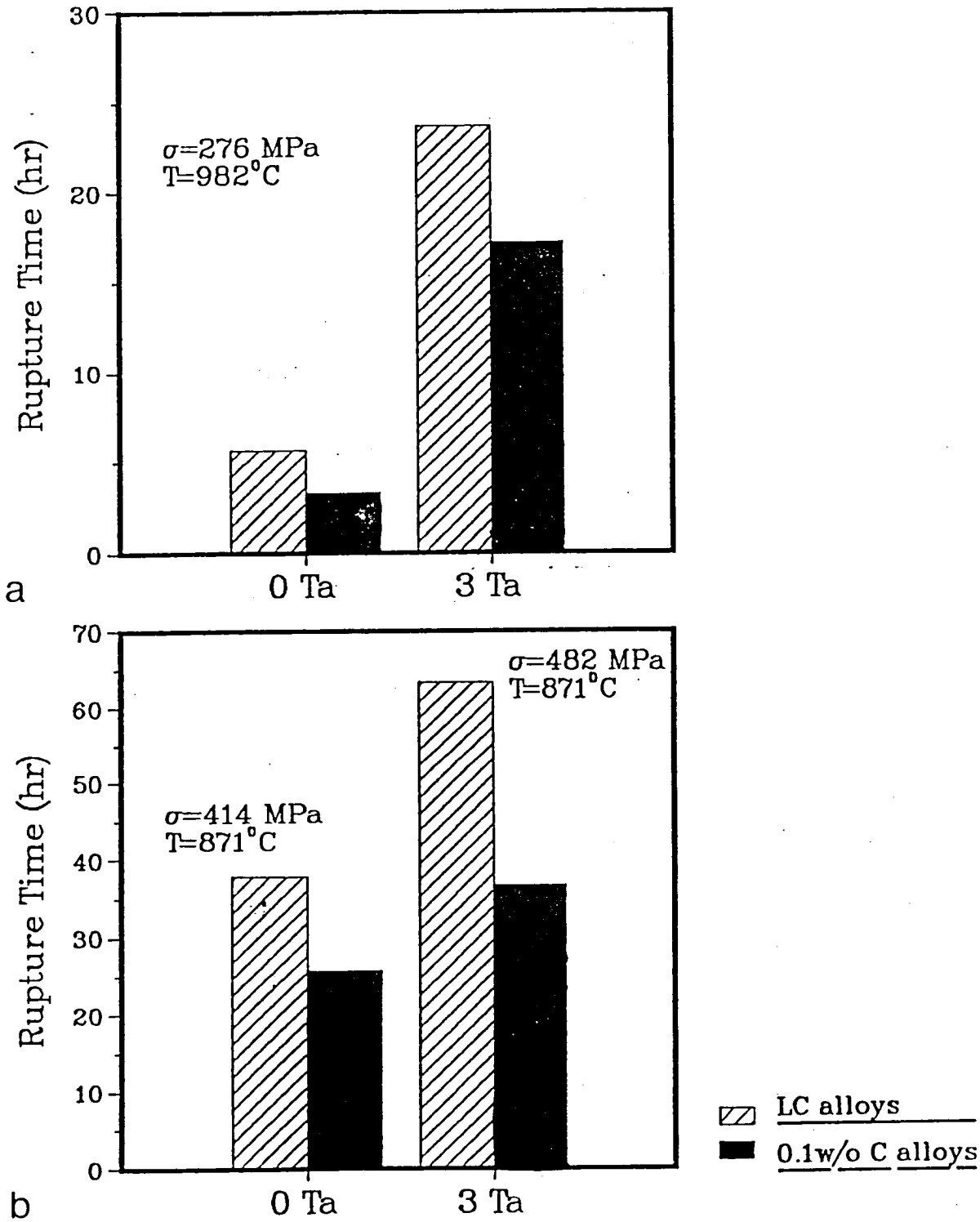

Figure 23. Rupture time at the same stress and temperature for the normal carbon and LC alloys containing 0 and 3 wt.% Ta.

The secondary creep rate as a function of stress is described usually by a power law expression such as equation (1) as discussed in the introduction. Insufficient secondary creep rate data were obtained in the present study to construct the necessary log secondary creep rate versus log applied stress plots at constant temperature to calculate the stress exponent in the power law relation. An estimate of this stress exponent was obtained by using the Larson-Miller plots to calculate the secondary creep rate for selected stresses within the limits of the creep rates measured experimentally and for the test temperatures employed in these tests. The resulting log secondary creep rate versus log applied stress plots are shown in Figures 24 and 25 for two temperatures. The stress exponents calculated from these plots are shown in Figures 26a and b. At each temperature, the stress exponent decreases slightly with increasing bulk tantalum content. In addition, the values are greater than the values of 3 - 5 found for pure metals or simple solid solutions but are typical values for nickel-base superalloys. In particular, the values are in good agreement with those obtained in a study on LC Mar-M247 single crystals [59].

D. Post-Creep Tested Microstructure

The microstructures present after creep rupture testing were examined using SEM and TEM. Coarsening of γ' was observed at all testing temperatures. The microstructure in Figure 27 illustrates the coarsening of γ' from a more spheroidal morphology observed in the heat treated condition (Figure 27a) to a more cuboidal morphology with rounded corners after testing at 760°C (1400°F) (Figure 27b and 28a). Although the micrograph in Figure 27b was taken from a specimen in the

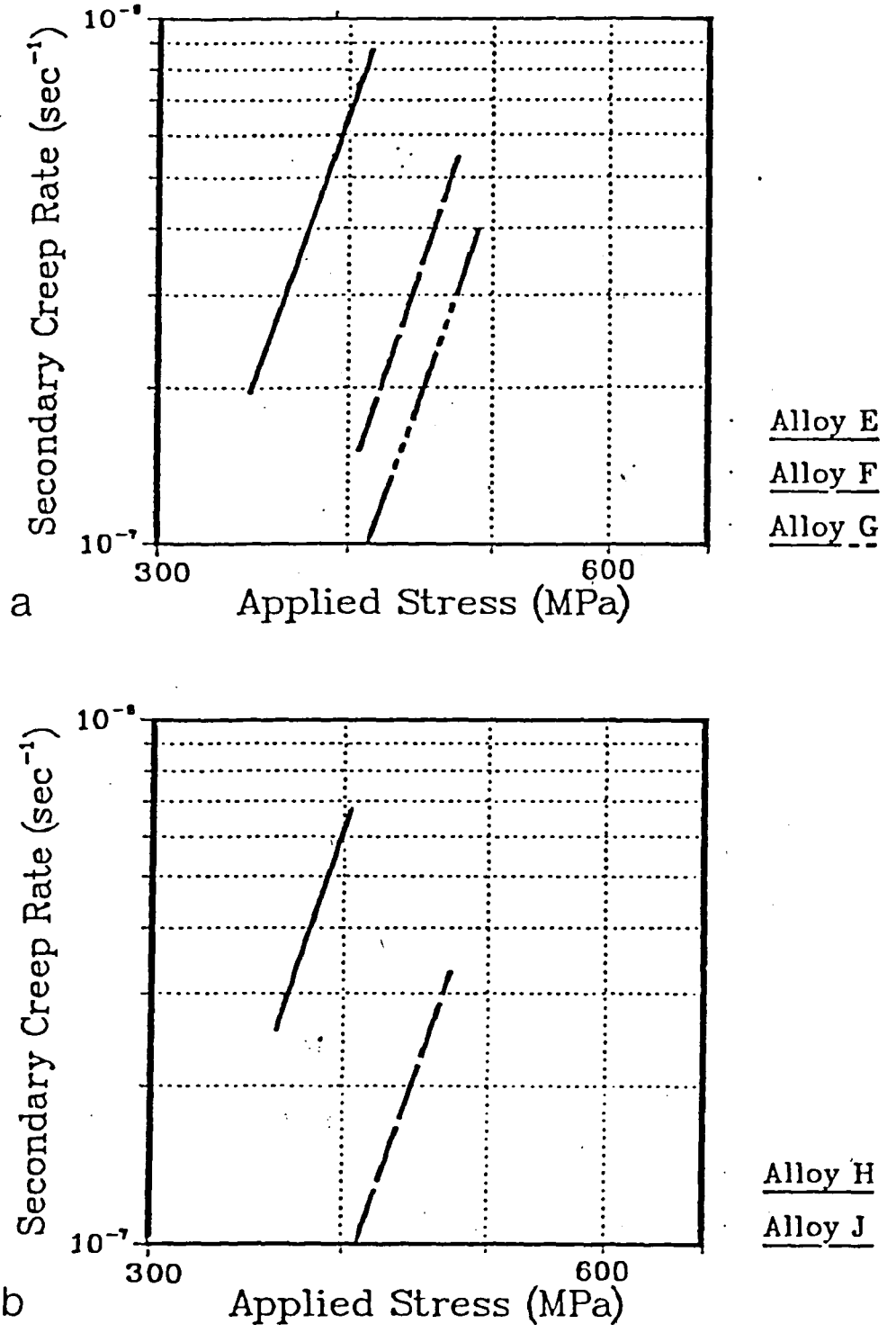

Figure 24. log-log plots of $\dot{\varepsilon}_s$ as a function of applied stress in (a) normal carbon Mar-M247 and (b) LC Mar-M247 type alloys at 871°C.

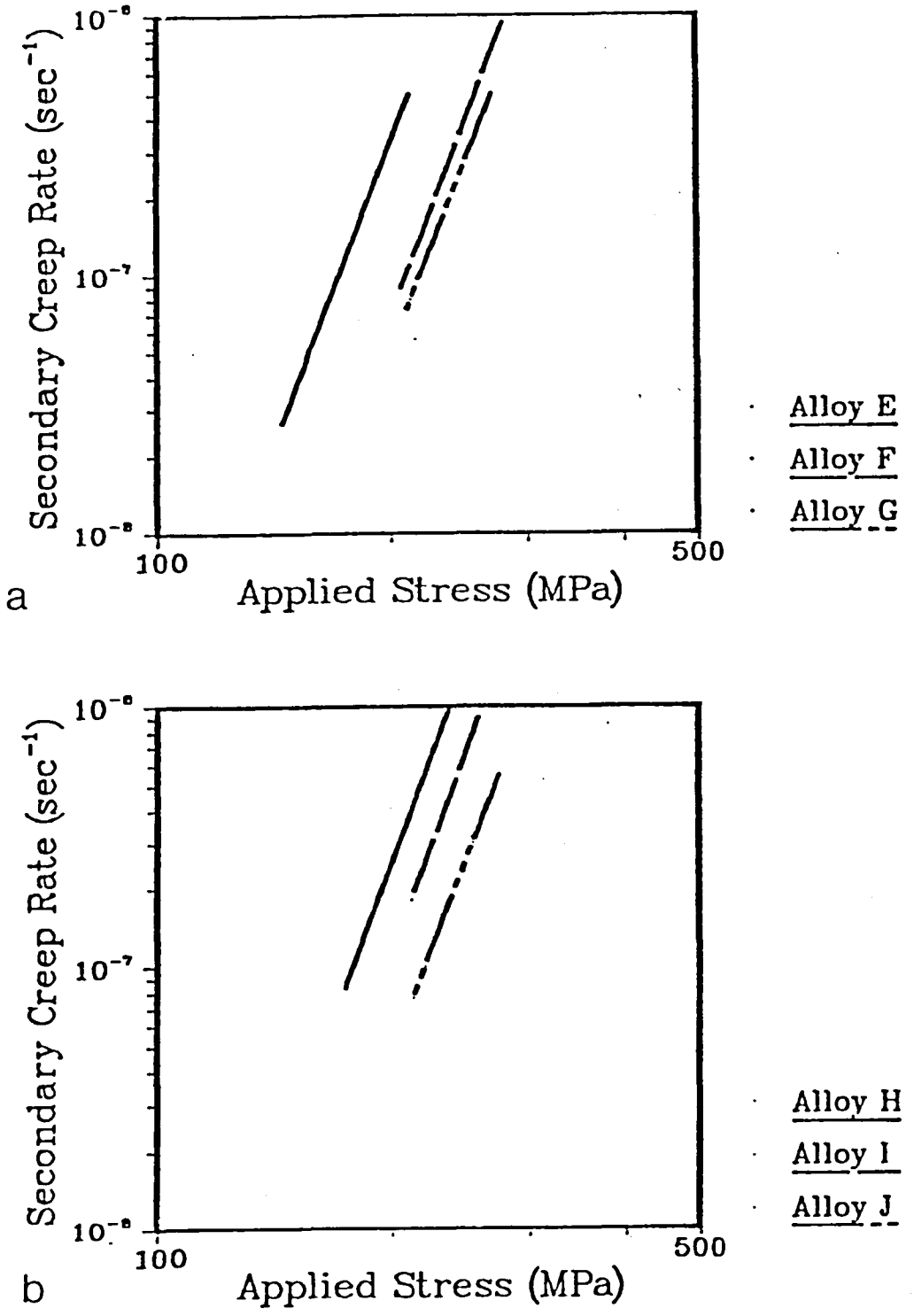

Figure 25. log-log plot of $\dot{\varepsilon}_s$ as a function of applied stress in (a) normal carbon Mar-M247 and (b) LC Mar-M247 type alloys at 982°C.

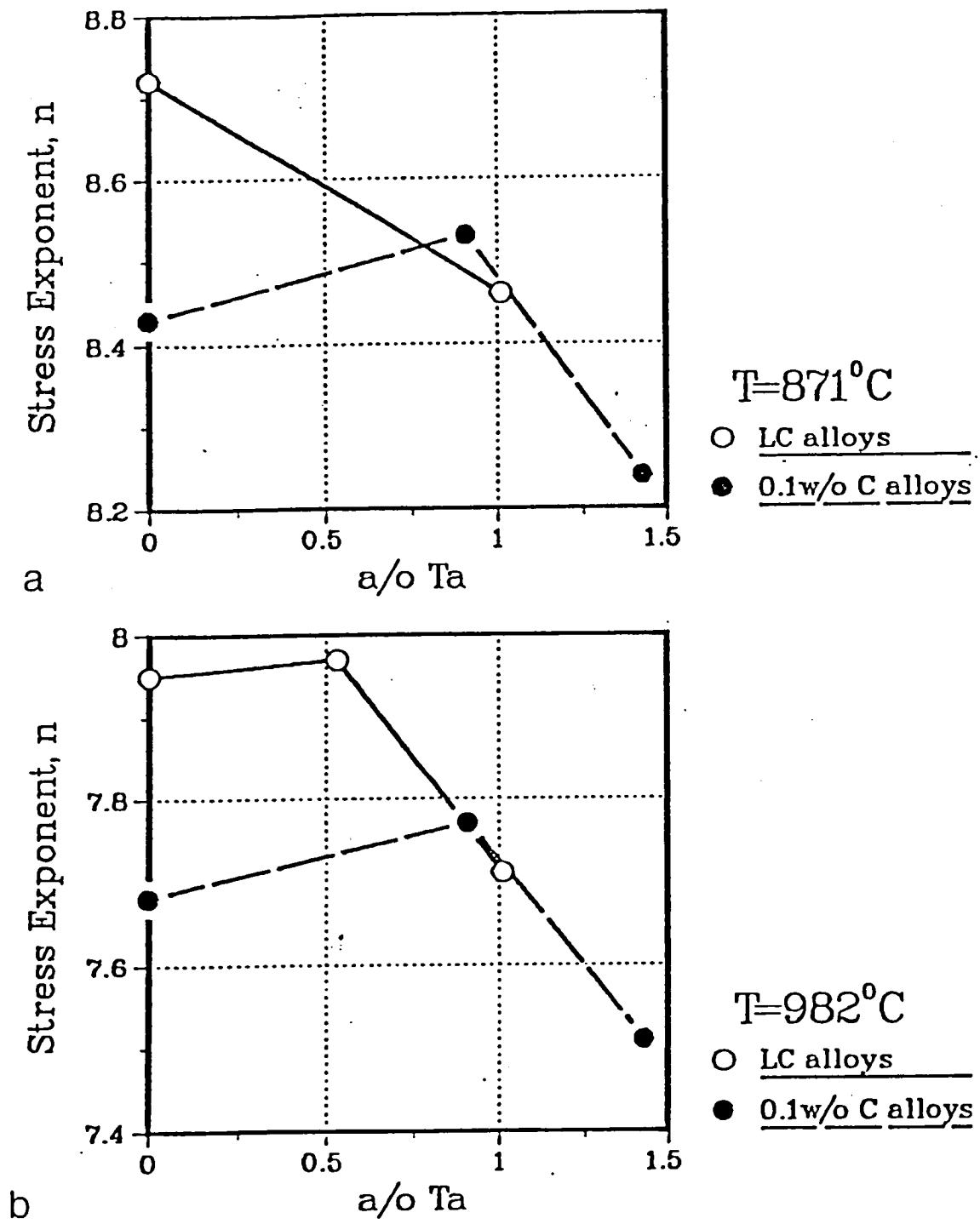

Figure 26. The stress exponent, n, as a function of Ta level in the alloys at (a) 871°C and (b) 982°C.

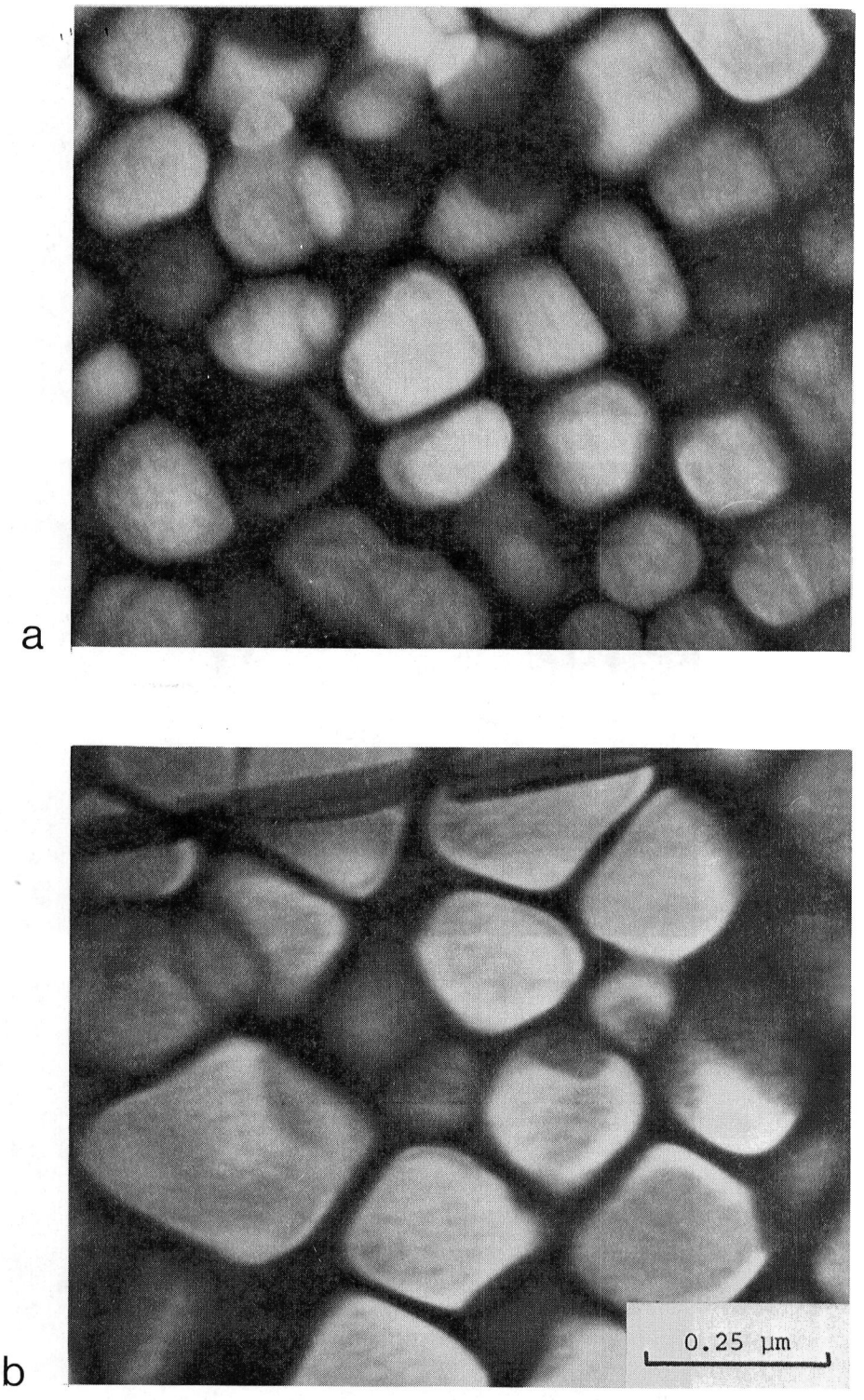

Figure 27: TEM dark field image of alloy F illustrating the coarsening of γ' during creep deformation: (a) before creep deformation and (b) after creep deformation. The micrograph after creep testing was taken from a foil cut from thread region of the test specimen.

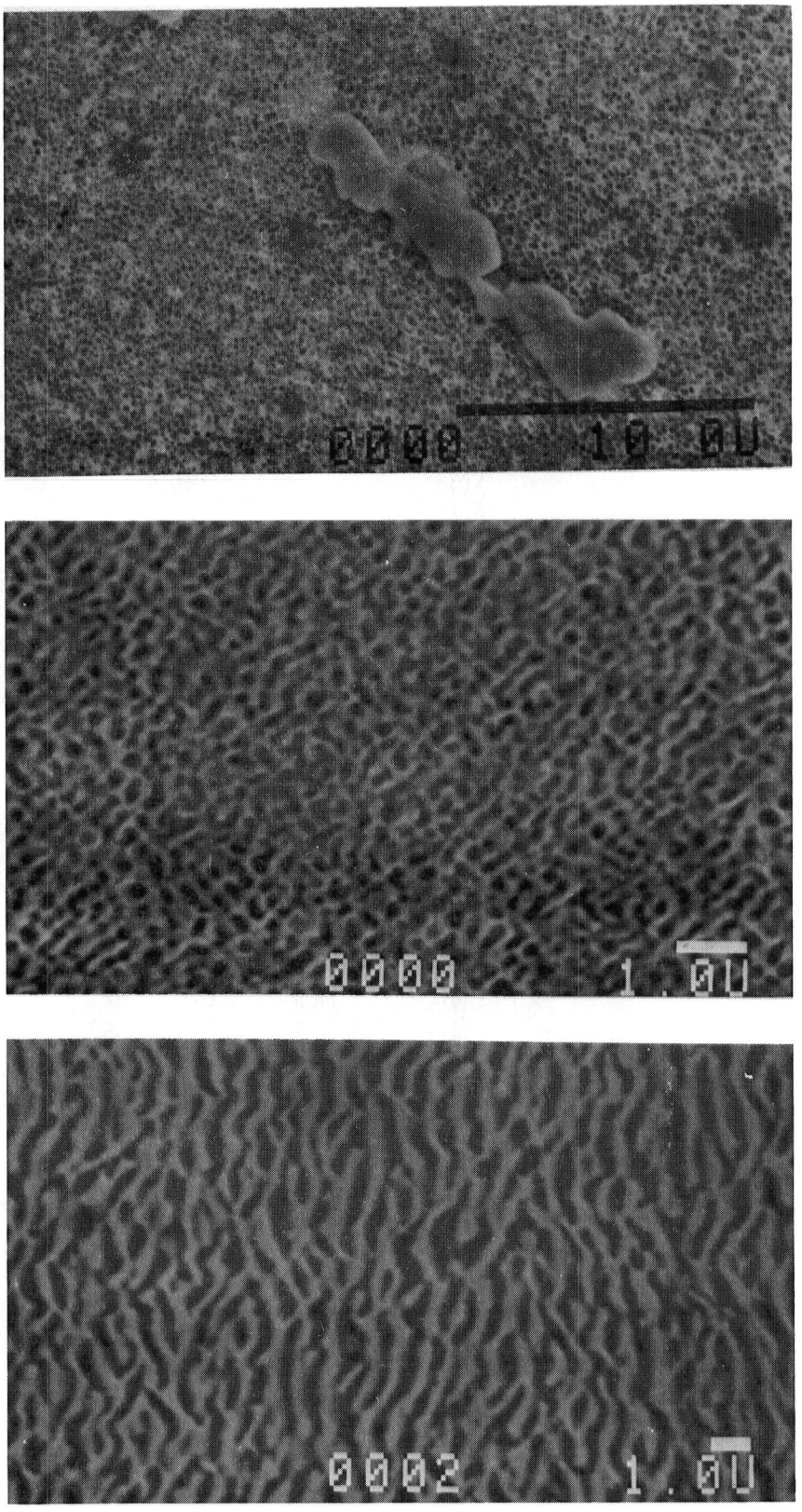

Figure 28: SEM micrographs of the Mar-M247 type alloys after creep deformation at (a) 760°C, (b) 871°C and (C) 982°C. These micrographs were taken on longitudinal sections in which the stress axis is horizontal.

thread region of the test specimen, it is representative of the γ' morphology observed throughout the entire gage section. The cuboidal structure was also observed in all alloys tested at 871°C (1600°F). However, γ' began to form a raft structure at this testing temperature as shown in Figure 28b. The propensity to form a γ' raft structure at 871°C seems to increase with increasing tantalum content for the structure in Figure 28b was observed only in some of the regions very near to the fracture surface in alloys G and J. However, further work is necessary to verify this observation. The γ' coarsened into a distinct platelet morphology which was perpendicular to the stress axis (Figure 28c) in all samples tested at 982°C (1800°F). The rafted γ' structure was observed throughout the gage section of each sample.

Examination of the creep ruptured specimens also revealed that many of the MC carbides near to the fracture surface in the normal carbon alloys fractured during tertiary creep (Figure 29a) or decohesion took place along the carbide/γ-γ' matrix interface (Figure 29b). No cracks in the MC carbides were observed in specimens deformed into the secondary creep stage. As shown in Figure 29a, the cracks were orientated perpendicular to the stress axis. In the LC alloys void formation was observed in the necked region (Figure 30).

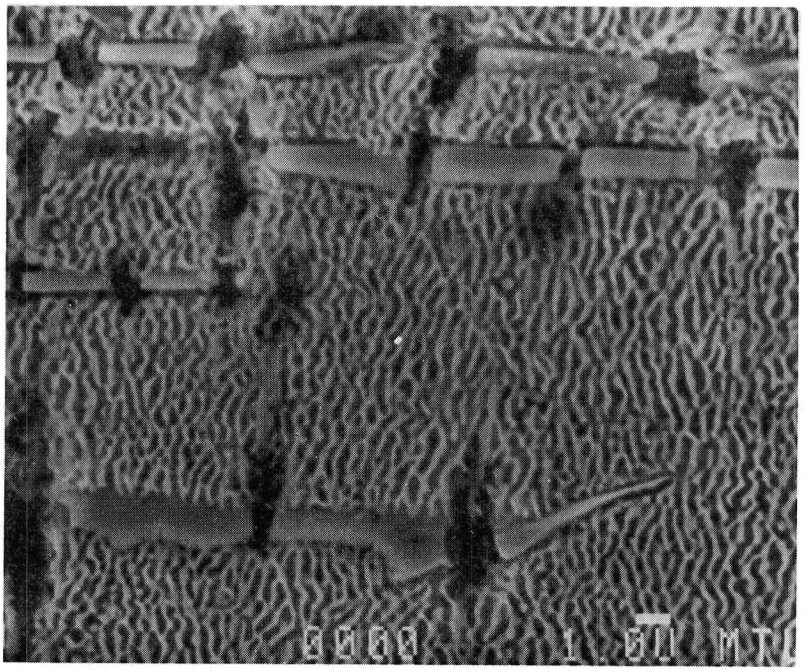

a

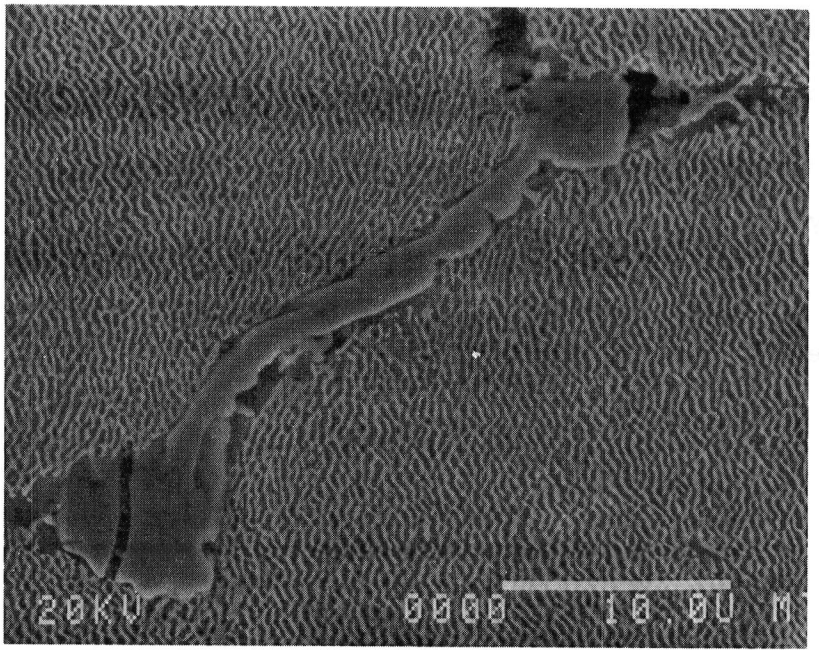

b

Figure 29. Longitudinal section of a normal carbon Mar-M247 type alloy (alloy F) deformed into the tertiary creep stage; (a) fracture of the MC carbides occurred in regions adjacent to the fracture surface or (b) decohesion took place at the carbide/ γ-γ' interface. The stress axis is horizontal in both micrographs.

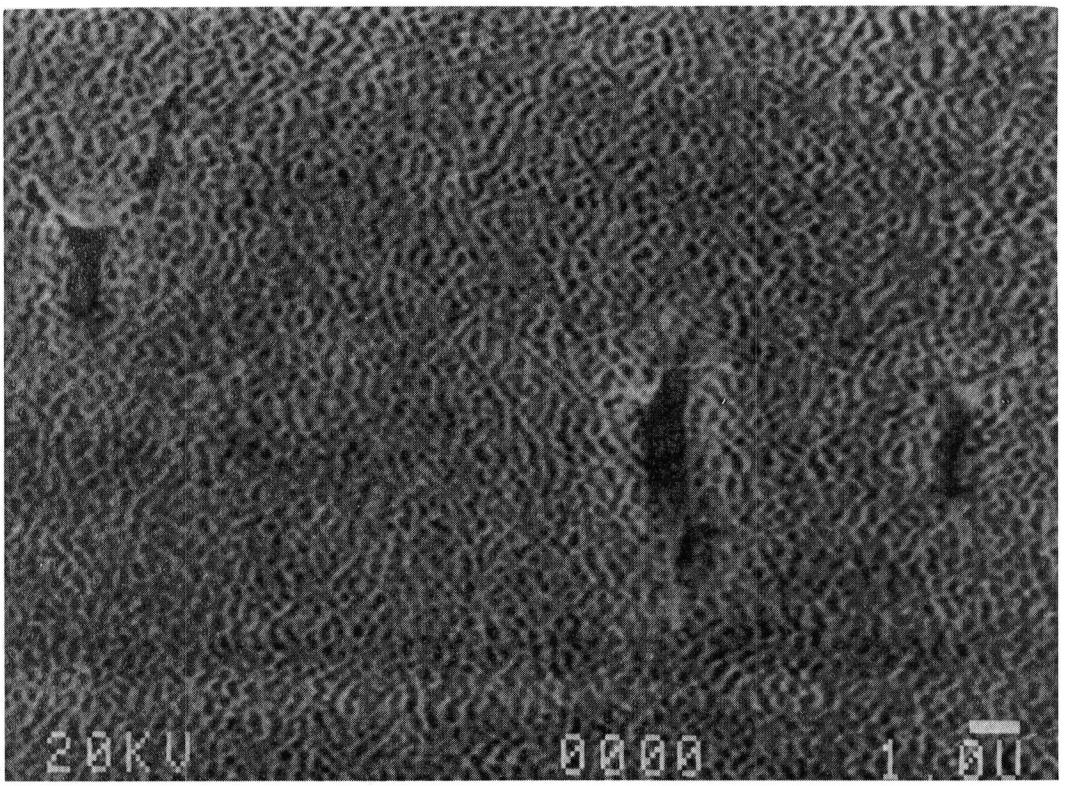

Figure 30: Void formation was found in the LC Mar-M247 type alloys near the necked region.

DISCUSSION

Microstructure and Phase Chemistries

The addition of tantalum has been shown to affect the carbide chemistry and stability in the normal carbon alloys and the γ and γ' phase chemistries in both alloy series. The effect of tantalum on the carbides will be discussed first before examining the influence of tantalum additions and carbon removal on the γ and γ' phase chemistries. In particular, we would like to draw attention to the "cascade effect" which results when carbon is reduced from 0.10 wt.% to 0.01 wt.%; since no carbides form in the LC alloys, those metallic elements which would otherwise partition to the carbides are released into the γ and γ' phases.

The replacement of titanium-rich MC carbides in the heat treated structure with tantalum-rich MC carbides, as tantalum is added to the alloys, is consistent with the empirical observed order of carbide formation [52]. In addition, the tantalum-rich MC carbides are more stable than the titanium-rich MC carbides with regard to MC carbide decomposition and formation of $M_{23}C_6$ or M_6C carbides. When the titanium -rich MC carbides are present, decomposition of some of these carbides must occur during heat treatment. The carbide decomposition releases carbon back into solution which would then diffuse to the carbon-poor dendrite cores with the subsequent formation of the tungsten-rich M_6C carbides. However, the addition of tantalum to the MC carbide only slows down the kinetics of the MC carbide decomposition. Although the tungsten-rich M_6C carbides were not observed in the heat treated microstructures of alloys F and G (which contain tantalum), M_6C carbides have been observed in these alloys aged at 982°C for 1000 hours [60].

The principle effect of adding tantalum to the alloy on the γ and γ' phase chemistries, from the partitioning ratios in Figure 14, is that tantalum partitions strongly to the γ' phase and aluminum and tungsten partition more to the γ phase. However, both Figures 12 and 13 indicate, that in general, the concentration of the other alloying elements either remain constant or decrease slightly in the γ' phase as tantalum is added and either remain constant or increase in the γ phase as tantalum is added. As pointed out earlier, some of the changes in γ and γ' chemistries may reflect variation in the overall bulk chemistry. Nevertheless, there seems to be a trend in that, as the overall tantalum content of the alloy increases, γ becomes more heavily alloyed (since the nickel concentration in the γ is decreasing). In addition, although titanium is released from the MC carbides as tantalum is added to the normal carbon alloys, the fraction of titanium tied up in the carbides that is released is sufficiently small so that a significant influence on the γ' phase chemistry is not observed.

The "cascade" effect referred to earlier can be examined by comparing the phase chemistry of the γ' phase in the two alloys series; the most dramatic impact on removing carbon from the alloy should involve releasing tantalum and titanium from the carbides which then partition strongly to γ'. Examining Figures 12a and 13a, at the lowest tantalum level in each alloy series, γ' is seen to contain about equivalent tantalum levels (slightly less than one atomic percent) but the bulk tantalum level is greater by a factor of two in the normal carbon alloy. Although not as dramatic, roughly equivalent tantalum levels in γ' are found in both of the higher tantalum alloys but the normal carbon alloy

contains about 50% more bulk tantalum than the LC alloy. The release of tantalum from the carbides primarily into the γ' phase of the LC alloys has a significant effect on mechanical properties as will be discussed in the next section. In addition, the titanium concentrations in the γ' phase are greater in the LC alloys compared to the normal carbon alloys and this result is consistent with the "cascade effect".

The effect of tantalum on the γ and γ' microstructure arises mainly from the increase in γ' wt. fraction as tantalum was added and the tendency for the γ' to become more spheroidal after heat treatment as the tantalum level in the alloy was reduced. The former result was anticipated since tantalum is thought to be a strong γ' forming element and our data is consistent with this. In addition, a similar increase in γ' volume fraction as 3 wt.% Ta was added to LC Mar-M247 type single crystals has been observed by Nathal [59]. Nathal also pointed out that elements which promoted higher volume fractions of γ' and increased the stability of γ' should also increase the γ' solvus temperature; Nathal's γ' solvus data and our data (see Figure 1) support this contention. An additional benefit of the increase in γ' solvus with increasing tantalum level is that higher solutionizing temperatures are possible. The higher solutionizing temperatures can lead to greater homogenization of the dendritic segregation present in the as-cast structure.

The dependence of γ' morphology on heat treatment and tantalum level is more puzzling. Changes in γ' morphology are usually linked to changes in mismatch in the lattice parameters between γ and γ' but no mismatch could be determined between γ and γ' at room temperature in our alloys. High temperature x-ray diffraction experiments are necessary to resolve the question of whether a mismatch exists at the

temperatures where γ' nucleates and grows. In addition, why there is a change in morphology from cuboidal γ' in the as-cast state to a more spheroidal γ' in the heat treated condition back to a cuboidal γ' during creep testing is unknown. The change in morphology of γ' from spherical to cubic has also been observed in these alloys aged unstressed for 1000 hours at 982°C [60] and in the work of Nathal [59] on similar Mar-M247 type alloys.

Mechanical Properties

Creep Rupture Properties

The results show that both carbon and tantalum affect the creep behavior of single crystal Mar-M247. Before discussing the more complex question of what is the tantalum effect in enhancing the creep rupture properties, the first question we wish to address is: do the carbides directly influence the creep properties of the Mar-M247 type alloys ? Although an effect of removing carbon on enhancing the creep rupture properties has been demonstrated, it has also been shown that removing carbon from the alloy releases those metallic elements into the γ and γ' phases which would otherwise partition to carbides. This may have a significant affect in the tantalum containing alloys since it has been shown that the addition of tantalum to the alloys strongly enhances the creep rupture properties.

One way to address the influence of the carbides is to assume that the creep rupture properties are controlled by the γ and γ' microstructure. Therefore, if the MC carbides do not directly influence the creep properties in the tantalum containing alloys, the secondary creep rate or rupture time should depend only on the Ta present in γ and γ'. The

total weight fraction of carbides in each of the alloys was obtained from the phase extraction analyses and the total tantalum contained in the carbides was determined from the EDX analysis. From these data, the amount of tantalum in γ and γ', designated as the "effective Ta", was calculated. From the Larson-Miller plots, Figures 21 and 22, the stress required for rupture in 100 hours at 982°C and the stress required to obtain a secondary creep rate of 1×10^{-6} sec^{-1} at 982°C were calculated and are shown in Figures 31a and b as a function of the effective Ta content in the alloy; the data for alloy E was not included since no tantalum was present in this alloy. The data for either plot fall onto a single nearly linear curve indicating the creep rupture properties are only a function of tantalum in the γ and γ'. Confirmation of this is obtained by examining the creep curves of alloys J and G; both contain ~1 at.% effective Ta but G contains the normal carbon level. Figure 32 shows that both the secondary creep rate and time to rupture are virtually identical for both alloys. These data strongly suggest that the MC carbides in alloys F and G (and apparently also the $M_{23}C_6$ carbides) do not directly influence the time to rupture or secondary creep rates.

A secondary effect of carbon is that the carbides decrease the total elongations in creep rupture. This is seen in Figure 32 in that the rupture ductility of the LC alloy (J) is greater than the normal carbon alloy (G). This may be readily understood given that carbides are a source of void nucleation. Examination of the microstructure after creep testing (Figure 29) revealed that the MC carbides had fractured. Apparently, once the alloys enter tertiary creep, the increase in strain is sufficient to cause fracture of the carbides or decohesion at the carbide/γ-γ' interface, which in turn leads to rapid

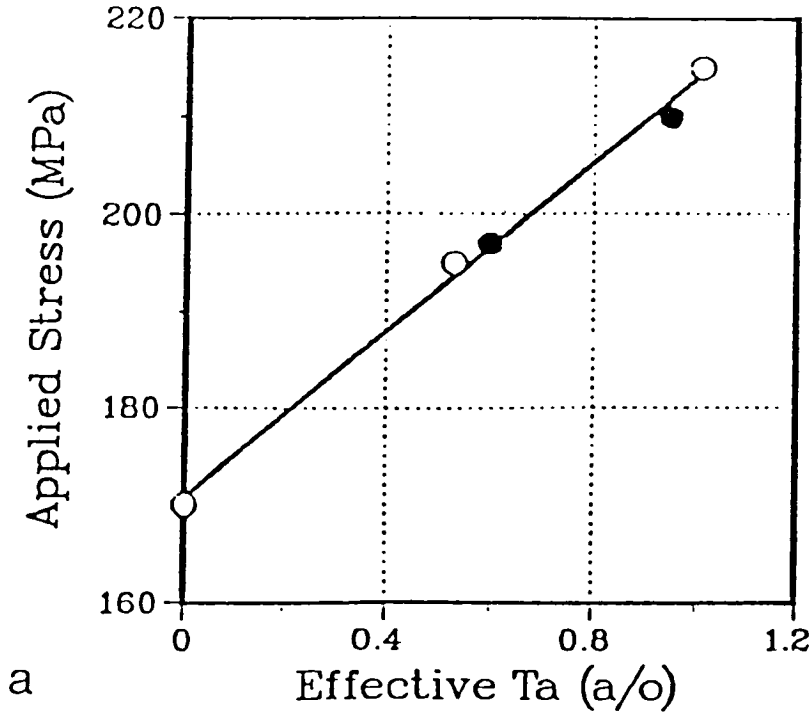

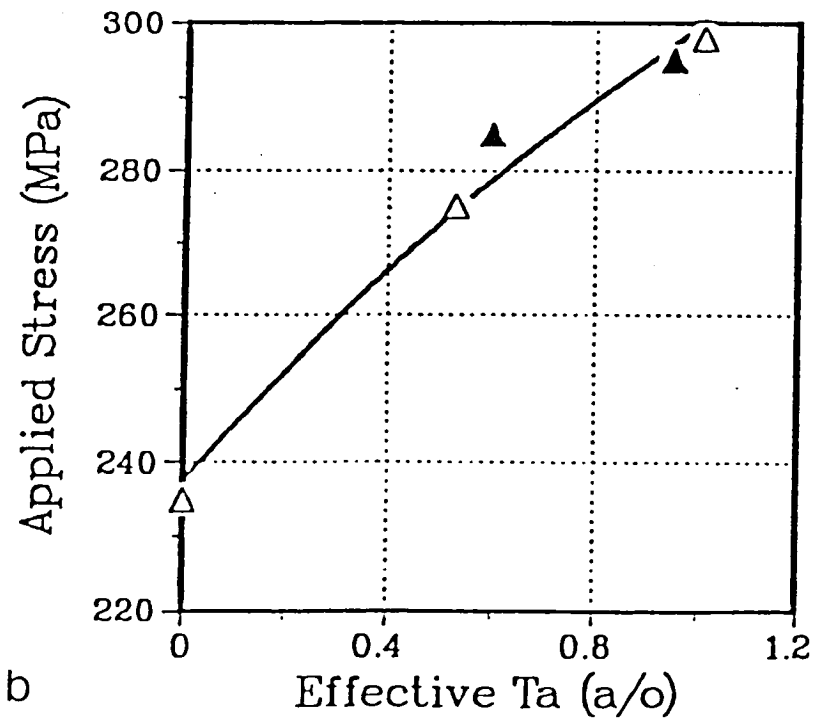

Figure 31. (a) Stress required for rupture in 100 hours at 982°C and (b) the stress required to obtain a secondary creep rate of $1x10^{-6}$ sec^{-1} at 982°C as a function of effective Ta content. The open and filled symbols in both figures refer to the LC and normal carbon alloys, respectively.

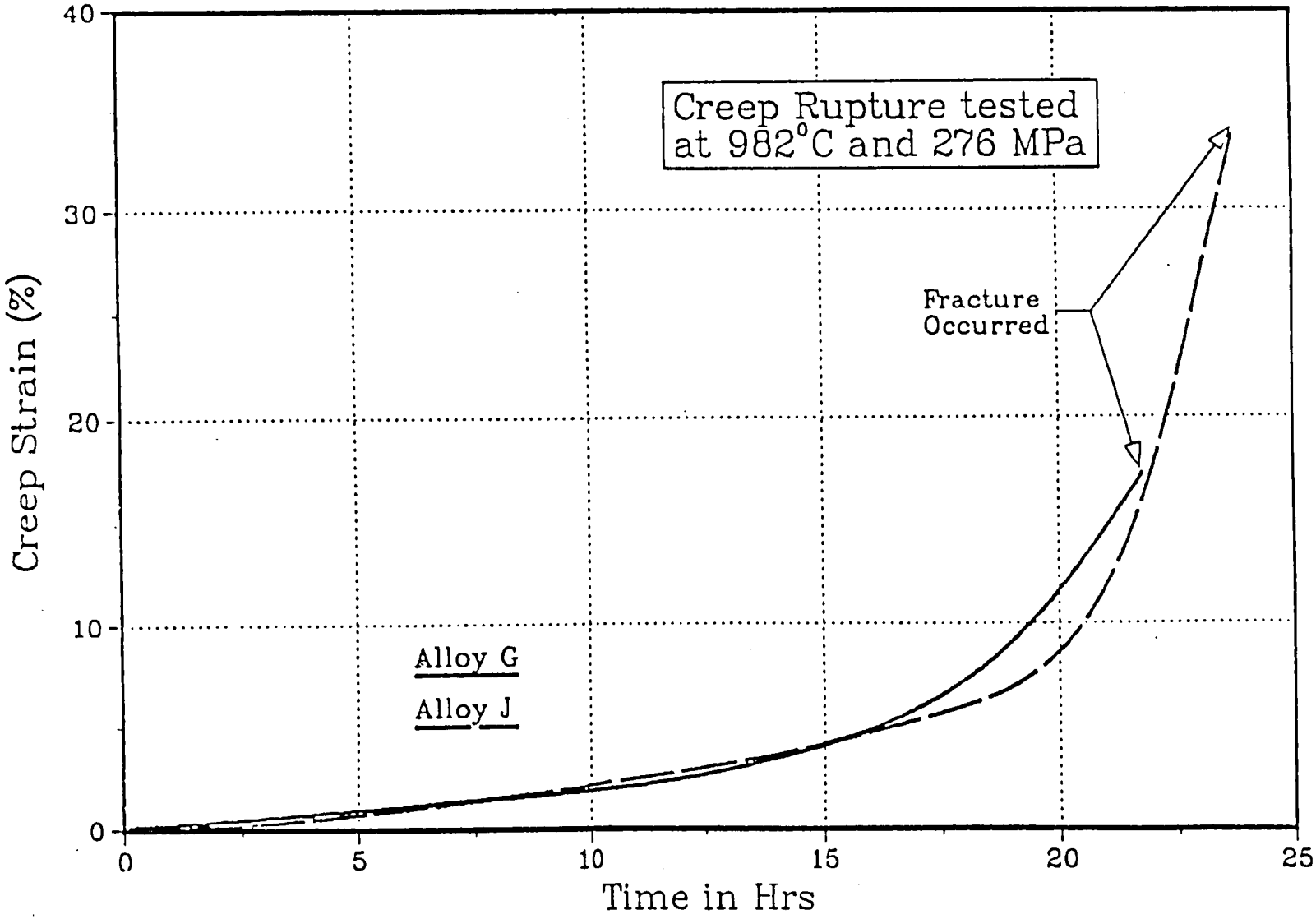

Figure 32. Creep curves for alloys G and J with the same effective Ta content exhibit virtually identical secondary creep rates and rupture times.

failure. Void nucleation in the LC alloys is more difficult and this results in larger ductilities. These data are consistent with ductilities observed in the hot tensile tests (Figure 17) which show the elongation and reduction in area at 540°C and 982°C are lower for the alloys containing the carbides compared to the LC alloys.

A final comment regarding the "carbon effect" and tantalum substitution is appropriate here. The previous analysis indicates that if LC single crystals of Mar-M247 are utilized, a tantalum level of 1.5 wt.% will still yield creep rupture properties commensurate with a normal carbon single crystal alloy containing 3 wt.% tantalum, a reduction of half the tantalum level.

Having demonstrated the tantalum-rich MC carbides do not directly influence the creep rupture properties, we now wish to examine what is the nature of the beneficial effect of tantalum on creep rupture properties in Mar-M247 type alloys. We suggest the beneficial effect as tantalum is added arises from four sources: increases in γ' wt. fraction, solid solution hardening of γ and γ', and possibly changes in the antiphase boundary energy of γ' and an influence of the γ' raft structure. Each of these sources will be examined in turn.

An increase in the volume fraction of fine γ' particles leads to an increase in the creep resistance of nickel-base alloys. This has been demonstrated in several systems but the work of Jackson et al. [61] on a sister alloy to Mar-M247, Mar-M200, is pertinent. Jackson et al. reported a 4 fold increase in rupture time as the γ' volume fraction increased from 30 to 45 percent. A similar increase in rupture time is observed in the present study at the highest tantalum level in each alloy series. However, the increase in γ' volume fraction is much

smaller than in the work on Mar-M200. Figure 33a shows a replot of the wt. fraction of γ' as a function of total tantalum content in the alloy. If the γ' wt. fraction data are replotted against the effective tantalum content as shown in Figure 33b, consistent with our previous "effective Ta" analysis, all data now plot onto a single curve. Based upon the comparison with the Mar-M200 study, the increase of about 5% in γ' weight fraction, shown in Figure 33, is not believed to be the sole mechanism responsible for enhancing the creep rupture properties.

Solid solution hardening of γ' and γ as tantalum is added to the alloy is also a possible strengthening mechanism. Solution hardening of γ' by tantalum has been reported [53] and an increase in the tantalum concentration in γ' was found from the phase chemistry analysis. Changes in the partitioning ratios and γ phase chemistry as tantalum is added also indicated that γ is becoming more heavily alloyed. This is important because tungsten, aluminum and chromium can act as strong solid solution hardeners of γ. In addition, tantalum and tungsten are effective in slowing down diffusion in γ and γ' at temperatures greater than 0.6 T_m. The presence of tantalum in γ' may also enhance the mechanical properties from an increase in the antiphase boundary energy of γ'. However, while this effect has been suggested elsewhere [4], no studies have directly shown a correlation between the addition of tantalum to γ' and any change in the antiphase boundary energy.

The final mechanism, which would be more important at higher temperatures, is the promotion of a rafted γ' structure by tantalum. Coarsening of γ' at high temperatures can cause a change in deformation mechanism from dislocations shearing the γ' particles to Orowan bypass. The development of a rafted γ' structure precludes the latter mechanism

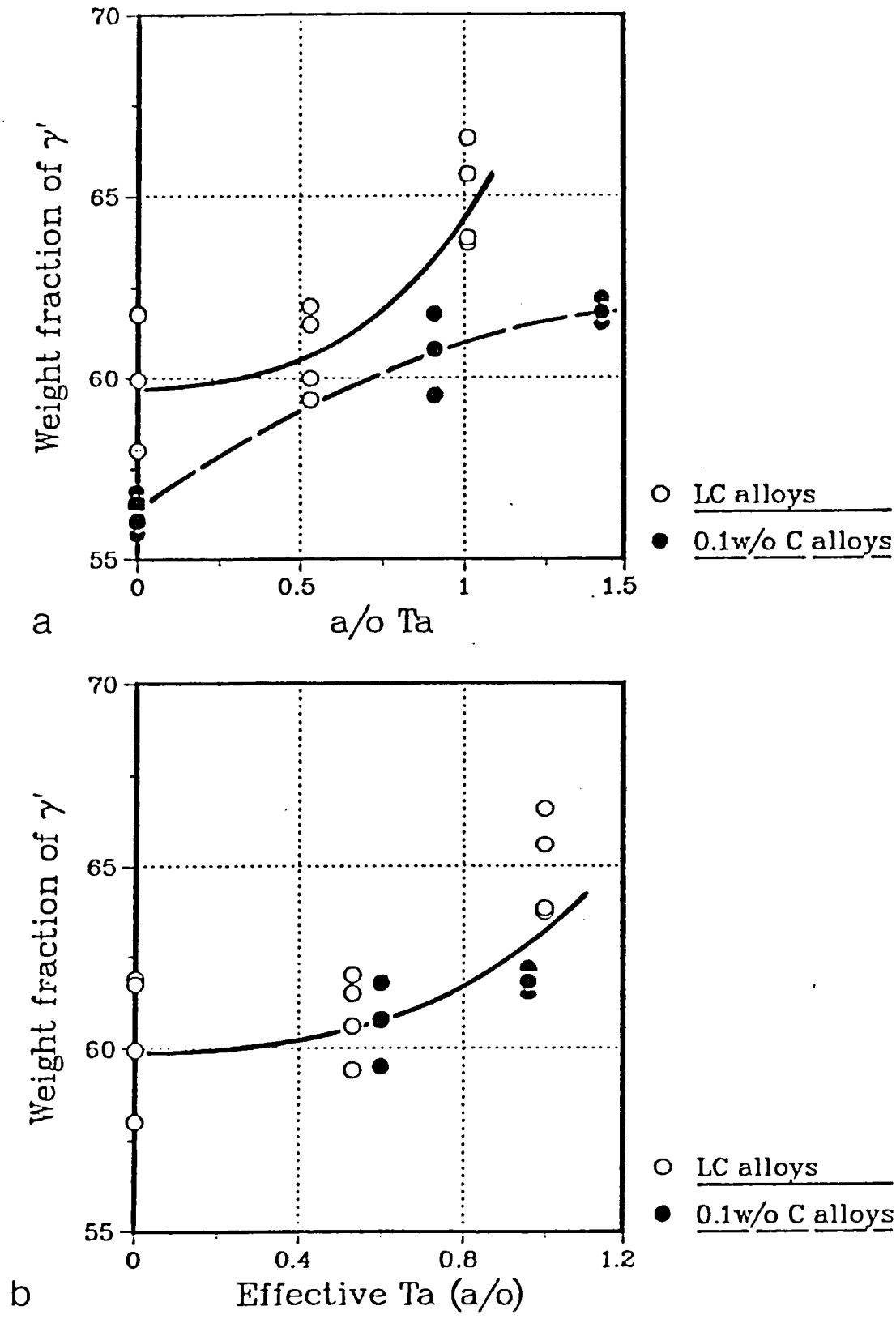

Figure 33. γ' weight fraction as a function of (a) Ta level in the alloys and (b) Ta level in the γ-γ' phases (effective Ta).

from occurring and insures particle cutting or dislocation climb around the particles.

The relative contributions of these four mechanisms in enhancing the creep rupture properties as tantalum is added to Mar-M247 alloys cannot be ascertained at the present time. However, an alloy matrix has been designed to examine potential substitutes for tantalum (see Table 7), and which should also be useful in separating out the contribution of several mechanisms. Strong γ' forming elements such as aluminum and/or titanium are proposed to be substituted for tantalum in order to maintain the same γ' volume fractions found in the Mar-M247 type alloys containing tantalum. Comparison of the creep rupture properties of the new alloy matrix to the present study, if the γ' volume fraction levels can be maintained, should indicate if the volume fraction effect is dominant or whether factors such as solution hardening of γ' with tantalum and changes in antiphase boundary energy with tantalum are important. The effect of the γ' raft structure can be eliminated if the creep tests are performed at 760°C or included if the creep tests are performed at 871°C or 982°C.

Tensile Properties

Increases in both the yield strength and tensile strength as tantalum is added to Mar-M247 type alloys was demonstrated. The mechanisms responsible for the increase in CRSS with tantalum would be the same as discussed previously in regard to the creep rupture properties with the exception of γ' rafting. No evidence of γ' rafting was found after tensile testing at any temperature. Any analysis of the CRSS would require separating out the relative contributions of the three

Table 7. Proposed Compositions for Ta Substitution Alloy Series Based on Modified Mar-M247 Composition*

Alloy Designation	
K	1.5 wt.% Ta + 0.3 wt.% Al (5.8 wt.% Al total)
L	0 wt.% Ta + 0.6 wt.% Al (6.1 wt.% Al total)
M	1.5 wt.% Ta + 0.4 wt.% Ti (1.4 wt.% Ti total)
N	1.5 wt.% Ta + 0.3 wt.% Al + 0.4 wt.% Ti (5.8 wt.% Al + 1.4 wt.% Ti total)

* All alloys will be cast in single crystal form from the same composition of master metal without C, Ta, Zr, Hf, and B; alloying elements will be added via master alloy additions at time of casting.

proposed mechanisms. Such an analysis may be possible if hot tensile tests are also performed on the proposed alloy matrix.

CONCLUSIONS

In this study, tantalum was systematically replaced by nickel in a normal carbon (0.10 wt.%) series of Mar-M247 type alloys and in a low carbon (0.01 wt.%) series of Mar-M247 type alloys.

1). The γ' solvus temperature increased from 1200 to 1250°C as 4.5 wt.% tantalum was added to the normal carbon alloys and from 1230 to 1250°C as 3 wt.% tantalum was added to the LC alloys.

2). The addition of tantalum to normal carbon Mar-M247 type alloys causes tantalum-rich MC carbides to replace titanium-rich MC carbides, consistent with the empirical order of carbide formation. The presence of M_6C carbides in the 0 wt.% Ta alloy after heat treatment and the absence of these carbides in the heat-treated tantalum containing alloys indicates the addition of tantalum slows down the kinetics of MC carbide decomposition at high temperatures.

3). Small (~0.2 μm) $M_{23}C_6$ carbides are observed in all normal carbon alloys and are identified as $Cr_{23}C_6$ carbides. The distribution of these carbides is nonuniform and their volume fraction was estimated to be very small in comparison to the other carbides.

4). The microstructure is found to be heat treatment sensitive. As-cast cuboidal γ' became more spheroidal after heat treatment and this tendency increased as the Ta level in the alloy decreased. However, upon aging under stress at 760°C or under no stress at 982°C (1000 hours), the spheroidal γ' reverts back to a cuboidal morphology; the

reason why these transitions occur is not understood. At higher temperatures, particularly 982°C, aging under stress (in creep tests) causes the γ' to form a rafted structure.

5). Based on the phase extraction results, the weight fraction of γ' increased from 60 to 65 pct. as the "effective Ta" level in the alloy increased from 0 to 3 wt.%. The lattice parameter of γ' also increased as tantalum was increased in the alloy.

6). Tantalum was observed to partition strongly to the γ' phase. In addition, as tantalum was added to either alloy series, the aluminum and tungsten partitioning ratios decreased while the partitioning ratios of the other alloying elements remained essentially constant.

7). When carbon is reduced from 0.10 wt.% to 0.01 wt.%, those metallic elements which otherwise partition to carbides, namely Ti and Ta, are released primarily into the γ' phase.

8). A reduction in secondary creep rate and an increase in rupture time result from increasing the tantalum content and decreasing the carbon level. The latter result can be interpreted in terms of a "cascade" effect; that is, the primary benefit of removing carbon is to increase the amount of "effective" Ta (i.e., the amount of Ta in γ and γ') in the alloy which enhances the creep rupture properties. By examining the creep rupture properties as a function of the effective Ta content, the results strongly suggest the MC carbides do not directly affect the secondary creep rate or rupture life. The carbides do affect

rupture ductility; carbide fracture and carbide-matrix decohesion causes void nucleation and a subsequent reduction in the rupture ductility.

9). The beneficial effects of tantalum in enhancing the creep rupture properties result, in part, from the increase in γ' wt. fraction with Ta and solid solution hardening as Ta is added due to the changes in phase chemistries of γ and γ'. Additional mechanisms which may also be factors include an increase in the antiphase boundary energy of γ' as tantalum is added to the alloy and enhancement of the γ' raft structure at higher temperatures with tantalum.

10). An increase in the yield strength and tensile strength result from increasing the tantalum content. The same mechanisms with the exception of γ' rafting act to enhance the strength as Ta increases. The propensity for the carbides to fracture as strain increases leads to rapid failure and causes the normal carbon alloys to exhibit lower ductilities than the LC alloys.

REFERENCES

1). J.R. Stephens: NASA TM-81617, NASA-Lewis Research Center, Cleveland, OH, 1980.

2). J.R. Stephens: NASA TM-82852, NASA-Lewis Research Center, Cleveland, OH, May 1982.

3). O.H. Kreige and J.M. Baris: Trans. of the ASM, 1969, vol. 62, p. 195.

4). R.F. Decker and C.T. Sims: The Superalloys, (Edited by C.T. Sims and W.C. Hagel), John Wiley and Sons Inc., New York,NY, 1972, p. 33.

5). W.C. Hagel and H.T. Beattie: Iron and Steel Inst., Spec. Rep. 64, p. 98-107.

6). F.H. Harf: NASA TM-83006, NASA-Lewis Research Center, Cleveland,OH, Oct. 1982.

7). C.T. Sims: The Superalloys, (Edited by C.T. Sims and W.C. Hagel), John Wiley and Sons Inc., New York,NY, 1972, p. 259.

8). R.L. Fleischer: Acta Met., 1963, vol. 11, p. 203.

9). R. Labusch: Physica Status Solidi, 1970, vol. 41, p. 659.

10). R. Labusch: Acta Met., 1971, vol. 20, p. 917.

11). W.B. Pearson: Handbook of Lattice Spacing and Structure of Metals and Alloys, Pergamon Press Ltd., London, 1958.

12). R.M.N. Pelloux and N.J. Grant: Trans. Met. Soc. AIME, 1960, vol. 218, p. 232.

13). B.E.P. Beeston, I.L. Dillamore and R.E. Smallman: Metal Sci. J., 1968, vol. 2, p. 12.

14). N.S. Stoloff: The Superalloys, (Edited by C.T. Sims and W.C. Hagel) John Wiley and Sons Inc., New York,NY, 1972, p. 79

15). B. Reppich: Acta Met., 1982, vol. 30, p. 87 and 95.

16). R. Labusch and R.B.Schwartz: J. Appl. Phys., 1978, vol. 49, p. 5174

17). C. Hammond and J. Nutting: Metal Sci., Oct. 1977, vol.11, p. 474.

18). E. Orowan: Symposium on Internal Stresses in Metals, Inst. of Met., London (1948), p. 451-453.

19). V. Gerold and H. Haberkorn: Phys. Status solidi, 1966, vol. 16, p. 675

20). H. Gleiter: Acta Met., 1968, vol. 16, p. 829.

21). S.M. Copley and B.H. Kear: Trans. TMS-AIME, 1969, vol. 239, p. 984.

22). H. Gayter and J. Nutting: Creep Strength in Steel and High Temperature Alloys, The Metal Society, London, 1974, p. 189

23). M.F. Ashby: Acta Met., 1972, vol. 20, p. 887.

24). R.W. Lund and W.D. Nix: Acta Met, 1976, vol. 24, p. 469.

25). W.J. Evans and G.F. Harrison: Met. Sci. J., 1976, vol. 10, p.307.

26). R.A. Stevens and P.E.J. Flewitt: Acta Met., 1981, vol. 29, p. 867.

27). S. Purushothaman and J.K. Tien: Acta Met., 1978, vol. 26, p. 519.

28). O. Ajaja, T.E. Howson, S. Purushothaman and J.K. Tien: Mat. Sci. and Eng., 1980, vol. 44, p. 165.

29). P.W. Davies, G. Nelmes, K.R. Williams and B. Wilshire: Met. Sci. J. 1973, vol. 7, p. 187.

30). K.R Williams and B. Wilshire: Met. Sci. J., 1973, vol. 7, p. 176.

31). J.D. Parker and B. Wilshire: Met. Sci. J., 1975, vol. 9, p. 248.

32). Brown, L.M. and Ham, R.K., Strengthening Mechanisms in Crystals (Edited by A. Kelly and R.B. Nicholson), Elsevier, Amsterdam, 1971, p. 9-135

33). D. Raynor and J.M. Silcock: Met. Sci. J., 1970, vol. 4, p. 121.

34). P.L. Threadgill and B. Wilshire: Proc. Creep Strength in Steel and High Temperature Alloys, The Metal Society, London, 1974, p. 8-14.

35). T. Gibbon: Scipta Met., 1978, vol. 12, p.749-751.

36). M. McLean: Proc. Roy. Soc. A, 1980, vol. 373, p.93-109.

37). C.R. Barrett and O.D. Sherby: Trans. of Met. Soc. of AIME, 1965, vol. 233, p. 1116.

38). R.A. Stevens and P.E.J. Flewitt: Mat. Sci. and Eng., 1979, vol. 37, p. 237.

39). J.K. Tien and S.M. Copley: Met. Trans., 1971, vol. 2, p. 543.

40). C. Carry and J.L. Strudel: Acta Met., 1978, vol. 26, p. 859.

41). A. Pineau: Acta Met., 1976, vol. 24, p. 559.

42). D.D. Pearson, F.D. Lemkey and B.H. Kear: Proc. 4th Int. Symp. on Superalloys, ed. by J.K. Tien et. al., ASM, Metal Park, 1980, p. 513,

43). R.B Mackay and L.J Ebert: Scripta Met., 1983, vol. 17, p.1217.

44). M.V. Nathal and L.J. Ebert: Scripta Met., 1983, vol. 17, p.1151.

45). B.H Kear and B.J. Piearcey: Trans. TMS-AIME, 1967, vol. 239, p. 1209-1215.

46). G.R. Leverant and B.H. Kear: Met. Trans., 1970, vol. 7, p. 491-498.

47). B.H. Kear, G.H. Leverant and J.M. Oblak: Trans ASM, 1969, vol. 62, p. 639.

48). G.R. Leverant, B.H. Kear and J.M. Oblak: Met. Trans, 1973, vol. 4A, p. 355.

49). R.A. Mackay, R.L. Dreshfield and R.D. Maier: Proc. Int'l Symp. on Superalloys, ASM, Metal Park, OH, Sept. 1980, p. 385.

50). R.A. Mackay and R.D. Maier: Met. Trans., 1982, vol. 13A, p. 1747.

51). R.V. Miner, Jr.:Met. Trans., 1977, vol. 8A, p. 259

52). Ford, J.A. and Herchenroeder, R.B., Tantalum in High-Temperature Alloys, Workshop on Conservation and Substitution Technology for Critical Materials, Cabot Corporation, June 15-17, 1980.

53). S. Chakravorty and D.R.F. West: Metals Technology, 1980, vol. 7, p.414

54). G.C. Fryburg, C.A. Stearns and F.J. Kohl: J. of the Electrochemical Society, 1977, vol.124, p. 1147.

55). S.M. Copley, A.F. Giamei, S.M. Johnson and M.F. Hornbecker: Met. Trans., 1970, vol. 1A, p. 2193.

56). M.J. Donachie and O.H. Kriege: J. of Materials, 1972, vol. 7, p. 269.

57). B.D Cullity: Elements of X-Ray Diffraction, 2nd ed., Addison-Wesley Publishing Company, Inc., Massachusetts, 1978, p. 363.

58). F.C. Monkman and N.J Grant: Proc. ASTM, 1956, vol. 56, p. 834.

59). M.V. Nathal: NASA TM 83479, NASA-Lewis Research Center, Cleveland, OH, 1984.

60). B. Wines: Coarsening Kinetics of γ' Phase in Superalloy, BS Thesis, Michigan Technological University, 1984.

61). J.J. Jackson, M.J. Donachie, R.J. Henrick and M. Gell: Met. Trans., 1977, vol. 8A, p. 1615.

1. Report No.	2. Government Accession No.	3. Recipient's Catalog No.
NASA CR-174779		

4. Title and Subtitle	5. Report Date
The Effect of Tantalum and Carbon on the Structure/ Properties of a Single Crystal Nickel-Base Superalloy	October 1984
	6. Performing Organization Code

7. Author(s)	8. Performing Organization Report No.
Hung C. Nguyen	None
	10. Work Unit No.

9. Performing Organization Name and Address	11. Contract or Grant No.
Michigan Technological University Houghton, Michigan	NAG 3-216
	13. Type of Report and Period Covered
12. Sponsoring Agency Name and Address	Contractor Report
National Aeronautics and Space Administration Washington, D.C. 20546	14. Sponsoring Agency Code 505-33-62

15. Supplementary Notes

Final report. Project Manager, Robert Dreshfield, Materials Division, NASA Lewis Research Center, Cleveland, Ohio 44135. This report was a thesis submitted in partial fulfillment of the requirements for the degree of Master of Science in Metallurgical Engineering to Michigan Technological University, Hougton, Michigan in August 1984.

16. Abstract

The microstructure, phase chemistry, and creep and hot tensile properties were studied as a function of tantalum and carbon levels in Mar-M247 type single crystal alloys. Microstructural studies showed that several types of carbides (MC, $M_{23}C_6$ and M_6C) are present in the normal carbon (0.10 wt % C) alloys after heat treatment. In general, the composition of the MC carbides changes from titanium-rich to tantalum-rich as the tantalum level in the alloy increases. Small ($\sim$0.2 μm) $M_{23}C_6$ carbides are present in all alloys. Tungsten-rich M_6C carbides are also observed in the alloy containing no tantalum. No carbides are present in the low carbon (0.01 wt % C) alloy series. The morphology of γ' is observed to be sensitive to heat treatment and tantalum level in the alloy. Cuboidal γ' is present in all the as-cast structures. After heat treatment, the γ' precipitates tend to have a more spheroidal-like morphology, and this tendency increases as the tantalum level decreases. On prolonged aging, the γ' reverts back to a cuboidal morphology or under stress at high temperatures, forms a rafted structure. The weight fraction and lattice parameter of the spheroidal γ' increases with increasing tantalum content. Changes in the phase chemistry of the γ matrix and γ' have also been analyzed using phase extraction techniques. The partitioning ratio (percent element in γ'/percent element in γ) decreases for tungsten and aluminum and increases for tantalum as the tantalum content increases for both alloy series; no significant changes occur in the partitioning ratios of the other alloying elements. A reduction in secondary creep rate and an increase in rupture time result from increasing the tantalum content and decreasing the carbon level. The latter result can be interpreted in terms of a "cascade effect"; that is, the primary benefit of removing carbon is to release those metallic elements, most notably tantalum, which otherwise partition to carbides, into the γ and γ' phases. The results strongly suggest the MC carbides do not directly influence the secondary creep rate or rupture life but do cause a reduction in rupture ductility. The data also suggest the principal sources of strengthening from tantalum arise from an increase in the amount of γ' with tantalum and an increase in solid solution strengthening of γ and γ' as a result of the phase chemistry changes. However, changes in the antiphase boundary energy of γ' with tantalum and a greater propensity of the γ' raft structure to form in creep tests at higher temperatures with increasing tantalum may also be factors.

17. Key Words (Suggested by Author(s))	18. Distribution Statement
Superalloys Nickel alloys Tantalum Carbon	Unclassified - unlimited STAR Category 26

19. Security Classif. (of this report)	20. Security Classif. (of this page)	21. No. of pages	22. Price*
Unclassified	Unclassified	99	A05

*For sale by the National Technical Information Service, Springfield, Virginia 22161

NASA Langley Rsch Center
Attn Library
Langley Field, VA 23365